

POLITECNICO DI TORINO  
ENERGY AND NUCLEAR ENGINEERING

MASTER'S DEGREE THESIS

---

**Experimental analysis of CO<sub>2</sub> splitting  
by perovskites-based chemical looping:  
isothermal redox cycling of SFNM-04  
in a microreactor setup**

---



*Supervisors:*

Prof. Massimo SANTARELLI  
Dr. Domenico FERRERO

*Author:*

Francesca Romana VALLI

March 2022

# Summary

Global electricity demand is increasing faster than renewables, driving strong requirements in generation from fossil fuels. As a result, carbon emissions from the electricity sector, which fell in both 2019 and 2020, are projected to increase in 2021 and in 2022. In a path towards meeting the international goals on climate change, the energy sector is going through epochal changes that involve in a transversal way the methods of supplying, transporting, storing and using energy. In this context, mitigation actions against CO<sub>2</sub> emissions are becoming increasingly fundamental. A recent analysis published by IEA highlighted that one of the key technology areas for putting energy systems on a sustainable trajectory is represented by carbon capture, utilisation and storage (CCUS). One possible solution in the direction of renewable fuel-based economy is represented by the chemical looping (CL) technology that is an innovative carbon capture process. Exploiting the capability of an oxygen carrier to assume different oxidation states, the chemical looping process is divided into two half cycles: firstly, the oxygen carrier is reduced by using high temperature heat as energy driver either in an inert ambient or with the contribution of a reducing agent to lower the reduction temperature, then is regenerated by an oxidizer (e.g CO<sub>2</sub> if the cycle is applied for CCU). In this study, the chemical looping technology is studied to be coupled with renewable high temperature heat input, supported by hydrogen as reducing agent. The process necessitates of a bi-functional looping material able to split CO<sub>2</sub> that combines both catalytic function for high fuel production and oxygen storage function for redox cycling. The key issue for the system performance is therefore represented by the oxygen carrier, that must accomplish several requirements. Although at present metal oxides dominate the research spectrum, in literature it is possible to find different materials such as cerium oxides. Perovskites have

recently emerged as promising materials for this application as they feature high non-stoichiometric oxygen exchange capacities while offering the benefit of significantly reduced operating temperatures. This thesis arises from an international project involving PoliTo, UNIUD and MIT. The aim of this work is to propose a new double-perovskite structured material with composition  $Sr_2FeNi_{0.4}Mo_{0.6}O_{6-\delta}$  for the thermochemical CO<sub>2</sub> splitting cycle to produce CO. The material has been tested in a microreactor setup to assess the influence of the sample mass and gas flow rates on the fuel yields. Isothermal redox cycles at 850°C have been performed with a crucible and with a tube-in-tube configuration. The results obtained in both configurations show that, at constant sample mass, the CO yields decreases when increasing the flow rates. While a decrease in the sample mass corresponds to an increase of the fuel yield at constant flow rate. The testing conditions in which the measured yield is independent from the gas flow rate have been identified. Finally, results obtained with SFNM-04 have been compared to data available in literature for LSM perovskites.

# Contents

<b>List of Tables</b>	v
<b>List of Figures</b>	vi
<b>1 Introduction</b>	1
1.1 The issue of Carbon Dioxide . . . . .	1
1.2 Carbon Capture, Storage and Sequestration . . . . .	3
1.2.1 CO <sub>2</sub> Capture . . . . .	4
1.2.2 CO <sub>2</sub> Transport . . . . .	7
1.2.3 CO <sub>2</sub> Storage . . . . .	7
1.2.4 CO <sub>2</sub> Utilization . . . . .	8
<b>2 Literature Review</b>	9
2.1 The Chemical Looping Technology . . . . .	9
2.2 Solar two-step H <sub>2</sub> O/CO <sub>2</sub> splitting cycles with metal-oxides . . . . .	13
2.3 Materials for Chemical Looping . . . . .	16
2.3.1 Volatile Oxygen Carriers . . . . .	16
2.3.2 Non-Volatile Oxygen Carriers . . . . .	18
2.3.3 Perovskites . . . . .	19
<b>3 Materials and Experimental Methods</b>	31
3.1 Materials: SFNM-04 . . . . .	31
3.1.1 Chemical-Physical Characterization . . . . .	33
3.1.2 Functional Characterization . . . . .	33
3.1.3 Stability of SFNM-04 to CO <sub>2</sub> . . . . .	35
3.1.4 Oxy-dry Reforming Catalytic Tests . . . . .	37

3.1.5	Influence of H <sub>2</sub> , CO <sub>2</sub> and temperature . . . . .	38
3.1.6	Exsolution . . . . .	41
3.2	Test Bench Description . . . . .	42
3.2.1	Microreactor and Furnace Section . . . . .	45
3.2.2	Gas Analyser . . . . .	46
3.3	Preliminary Experimental Procedures . . . . .	49
<b>4</b>	<b>Results</b>	<b>51</b>
4.1	Data Processing . . . . .	53
4.2	Test (I) . . . . .	57
4.3	Test (II) . . . . .	59
4.4	Test (III) . . . . .	60
4.5	Test (IV) . . . . .	62
4.6	Test (V) . . . . .	63
4.7	Test (VI) . . . . .	65
4.8	Test (VII) . . . . .	66
<b>5</b>	<b>Summary and Discussion</b>	<b>68</b>
5.1	Influence of Sample Mass . . . . .	68
5.2	Influence of the Oxidation Flow Rates . . . . .	70
5.3	Influence of the Reactor Setup . . . . .	72
5.4	Comparison of SFNM-04 with LSM-based perovskites . . . . .	75
<b>6</b>	<b>Conclusion</b>	<b>77</b>
	<b>Bibliography</b>	<b>80</b>

# List of Tables

2.1	LM A-substituted perovskites: $\mu\text{mol/g}$ of $\text{O}_2$ and $\text{CO}$ evolved during thermochemical redox cycling. . . . .	24
2.2	Summary of the fuel yields of LSM Al and Cr-doped perovskites in solar-to-fuel thermochemical cycles found in literature. . . . .	29
3.1	$\text{CO}$ e $\text{H}_2$ production by SFNM04 powders. . . . .	37
3.2	Results of the isothermal tests performed at $T=750^\circ\text{C}$ and $T=850^\circ\text{C}$ varying $\text{CO}_2$ and $\text{H}_2$ content. . . . .	40
4.1	Brief summary of the set of experimental tests performed . . . . .	51
4.2	Parameters kept constant in all the tests performed. . . . .	52
4.3	Test (I): results in terms of $\text{CO}$ peak rates and total $\text{CO}$ yield. . . .	58
4.4	Test (II): results in terms of $\text{CO}$ peak rates and total $\text{CO}$ yield. . . .	60
4.5	Test (III): results in terms of $\text{CO}$ peak rates and total $\text{CO}$ yield. . . .	61
4.6	Test (IV): results in terms of $\text{CO}$ peak rates and total $\text{CO}$ yield. . . .	63
4.7	Test (V): results in terms of $\text{CO}$ peak rates and total $\text{CO}$ yield. . . .	64
4.8	Test (VI): results in terms of $\text{CO}$ peak rates and total $\text{CO}$ yield. . . .	66
4.9	Test (VII): results in terms of $\text{CO}$ peak rates and total $\text{CO}$ yield. . . .	67

# List of Figures

1.1	Global average land-sea temperature anomaly. [1]. . . . .	1
1.2	Annual CO <sub>2</sub> Emissions from Coal. [8]. . . . .	2
1.3	Schematic of CCUS. [9]. . . . .	3
1.4	Carbon Capture Processes. [10]. . . . .	4
1.5	Schematic of a Pre-Combustion capture process [16]. . . . .	5
1.6	Existing CO <sub>2</sub> pipeline infrastructure and CCUS projects in the United States [23]. . . . .	7
1.7	Theoretical CO <sub>2</sub> storage capacity by region [25]. . . . .	8
2.1	Syngas Conversion Pathways [26]. . . . .	10
2.2	Schematic description of Chemical Looping Combustion [32]. . . . .	11
2.3	Schematic description of Chemical Looping Reforming [32]. . . . .	12
2.4	Schematic description of the CSP-aided, two-step, redox-pair-base, water splitting CL process [34]. . . . .	14
2.5	Zn/ZnO two-step solar thermochemical cycle . . . . .	17
2.6	Ideal cubic structure of an ABX <sub>3</sub> perovskite . . . . .	20
2.7	O <sub>2</sub> production rates in LSM perovskites with different content of Sr. [66]. . . . .	22
2.8	Re-oxidation yields of the perovskites under CO <sub>2</sub> exposure. [66]. . . . .	23
2.9	LSM perovskites O <sub>2</sub> and CO yields from cycle 2 to cycle 10 . . . . .	23
2.10	SLMA perovskites and Ceria: Comparison of CO production . . . . .	25
2.11	Short-term durability test: total amount of CO produced per cycle for SLMA2 . . . . .	26
2.12	LSM Cr-doped perovskites: results of the isothermal cycles at 1400°C in terms of CO production and O <sub>2</sub> release . . . . .	27
3.1	Ruddlesden-Popper phases structure . . . . .	32

3.2	XRD spectra of SFNM-04 and SFNM-05 samples. . . . .	33
3.3	SFNM-04 H <sub>2</sub> consumption in TPR analysis of 4 subsequent reduction and re-oxidation cycles. . . . .	34
3.4	Functional Characterization of SFNM-04: XRD spectra after 2 and 4 reduction cycles . . . . .	35
3.5	XRD analysis of SFNM-04 after the treatment in 30% C <sub>3</sub> H <sub>8</sub> at 800 °C for two hours. . . . .	36
3.6	XRD analysis of SFNM-04 after the thermal treatments . . . . .	36
3.7	Catalytic results of Oxy-dry Reforming Test for SFNM-04. . . . .	37
3.8	CO production expressed in [ $\mu\text{mol/g/s}$ ] and in [%] terms: 9 Isothermal Cycles at T=850°C by varying the CO <sub>2</sub> content in the range 6-100 % during reduction. . . . .	38
3.9	CO production expressed in [ $\mu\text{mol/g/s}$ ] and in [%] terms: 10 Isothermal Cycles at T=850°C by varying the H <sub>2</sub> content in the range 5-100 % during reduction. . . . .	39
3.10	Illustration models for (a) structure transformation and (b) surface morphology evolution of Sr <sub>2</sub> FeMo <sub>0.65</sub> Ni <sub>0.35</sub> O <sub>6-<math>\delta</math></sub> under reducing atmosphere [87]. . . . .	41
3.11	Test bench setup . . . . .	43
3.12	Software home screen . . . . .	44
3.13	Carbolite Gero furnace . . . . .	45
3.14	Microreactor setup: a) Alumina Crucible; b) tube-in tube. . . . .	46
3.15	A simplified circuit diagram of a Thermal Conductivity Detector [90] . . . . .	47
3.16	Typical structure of a NDIR [93] . . . . .	49
4.1	CO concentrations expressed [ppm] during Test (I). . . . .	53
4.2	CO production rate in [ $\mu\text{moles/s/g}$ ] during the oxidation step. . . . .	55
4.3	Correction method: break point identification in the original curve by means of the straight line. . . . .	56
4.4	Correction method: corrected CO production curve. . . . .	56
4.5	Test (I) results in terms of CO production rates [ $\mu\text{moles/s/g}$ ]. . . . .	57
4.6	Repeatability test performed by testing the material two times with the same oxidation flow rate equal to 200 [Nml/min]. . . . .	58
4.7	Test (II) results in terms of CO production rates [ $\mu\text{moles/s/g}$ ]. . . . .	59
4.8	Test (III) results in terms of CO production rates [ $\mu\text{moles/s/g}$ ]. . . . .	61

4.9	Test (IV) results in terms of CO production rates [ $\mu\text{moles/s/g}$ ]. . .	62
4.10	Test (V) results in terms of CO production rates [ $\mu\text{moles/s/g}$ ]. . . .	64
4.11	Test (VI) results in terms of CO production rates [ $\mu\text{moles/s/g}$ ]. . .	65
4.12	Test (VII) results in terms of CO production rates [ $\mu\text{moles/s/g}$ ]. . .	67
5.1	CO production rates curves: comparison at fixed setup configura- tion and oxidation flow rates. . . . .	68
5.2	CO specific yields: upward trend resulting from a gradual decrease of SFNM-04 mass. . . . .	70
5.3	Influence of the oxidation mass flow rates on the results of Test (II) and Test (V) considered as reference. . . . .	71
5.4	Specific CO yields as function of oxidation flow rates. . . . .	72
5.5	Reactor setup influence: CO production rate curves comparison of Test (V) and Test (VI). . . . .	73
5.6	Reactor setup influence: CO specific yields comparison of Test (V) and Test (VI) at fixed flow rates. . . . .	73
5.7	Reactor setup influence: CO specific yields comparison of Test (V), Test (VI) and Test (VII) at fixed gas velocities. . . . .	75

# Acronyms

## **CCUS**

Carbon Capture, Utilisation and Storage. 3

## **CDS**

Carbon Dioxide Splitting. 14

## **CL**

Chemical Looping. 10

## **CLC**

Chemical Looping Combustion. 10

## **CLG**

Chemical Looping Gasification. 10

## **CLR**

Chemical Looping Reforming. 10

## **CSP**

Concentrated Solar Power. 14

## **EDX**

Energy Dispersive X-ray. 33

## **EGA**

Emerson Gas Analyzer. 52

**IEA**

International Energy Agency. 3

**IRD**

Infrared Detector. 46

**LCM**

Lanthanum-doped Calcium-Manganite perovskites. 23

**LMA**

Lanthanum-Manganite-doped Aluminium perovskites. 25

**LSM**

Lanthanum-doped Strontium-Manganite perovskites. 21

**MFC**

Mass Flow Controller. 44

**MIT**

Massachusetts Institute of Technology. 31

**NDIR**

Non-Dispersive Infrared Detector. 49

**PCU**

Power Conditioning Unit. 45

**PSI**

Paul Scherrer Institute. 17

**RP**

Ruddlesden-Popper. 31

**SOFC**

Solid Oxide Fuel Cell. 31

**TCD**

Thermal Conductivity Detector. 46

**TPR**

Temperature Programmed Reduction. 33, 34

**TR**

Thermal Reduction. 14

**UNIUD**

Università degli Studi di Udine. 31

**WS**

Water Splitting. 14

**XPS**

X-ray Photoemission Spectroscopy. 33

**XRD**

X-ray Diffraction. 33

# Chapter 1

## Introduction

### 1.1 The issue of Carbon Dioxide

Warmed by sunlight, Earth's surfaces continuously radiate thermal infrared energy.

The so called greenhouse gases absorb that heat and release it gradually over time. Without this natural effect, Earth's average annual temperature would drop below freezing. But increases in greenhouse gases concentrations in the atmosphere have tipped the Earth's energy budget out of balance, trapping additional heat and raising Earth's average temperature. The average global temperature increase is shown in the Figure 1.1.

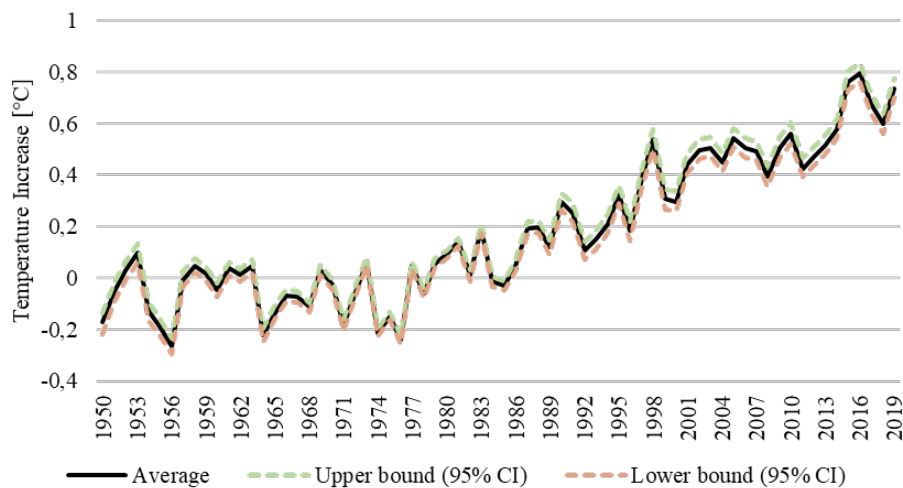


Figure 1.1: Global average land-sea temperature anomaly. [1].

In this context, CO<sub>2</sub> is of particular significance because, despite it absorbs less heat per molecule with respect to the others greenhouse gases, it is more abundant, and it stays in the atmosphere much longer. CO<sub>2</sub> is responsible for about two-thirds of the total energy imbalance that is causing Earth’s temperature to rise [2]. While global CO<sub>2</sub> emissions declined by 5.8% in 2020, due to the COVID-19 forced confinement [3, 4], in 2021 global energy-related CO<sub>2</sub> emissions are projected to rebound and grow by 4.8% corresponding to the largest single increase since the carbon-intensive economic recovery from the global financial crisis occurred more than a decade ago [3]. If, on the one hand the continuing renewable energy cost declines will help meet rising renewable targets [5], on the other hand power, in terms of fossil fuels combustion, is still the largest carbon emitter in the energy sector, accounting for almost 40% of global energy-related emissions [6]. Among the fossil fuel types, coal is responsible for 44% of the world total CO<sub>2</sub> emissions [7] and yet it remains by far the largest fuel source for power generation, at 38%, followed by gas at about 20%. Moreover, in the emerging economies, such as China and India, the coal-fired share of total generation is higher than 60% [6].

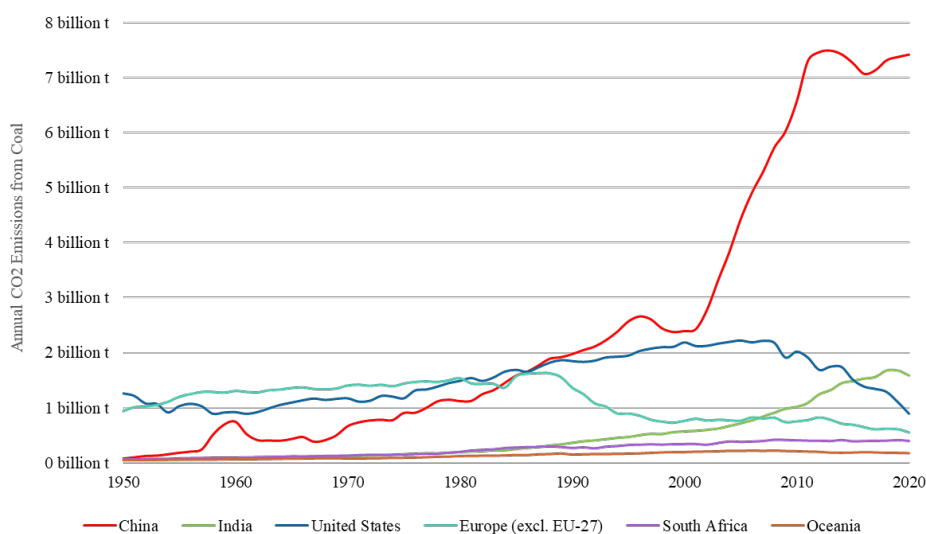


Figure 1.2: Annual CO<sub>2</sub> Emissions from Coal. [8].

Being the Paris Agreement’s goal to keep the increase in global average temperature below 2°C above pre-industrial levels, the global power sector is expected to dramatically reduce its carbon intensity.

## 1.2 Carbon Capture, Storage and Sequestration

The International Energy Agency (IEA) has long highlighted that there are no single or simple solutions to reach international energy and climate goals but their analysis clearly shows that one of the key technology areas for putting energy systems on a sustainable trajectory will be Carbon Capture, Utilisation and Storage (CCUS) [9].

CCUS represents the only technology that contributes at the same time to the reduction of emissions in key sectors directly, and to removing  $\text{CO}_2$  to balance emissions that cannot be avoided. A simple schematic diagram to explain the operating principles of CCUS systems is reported in Figure 1.3.

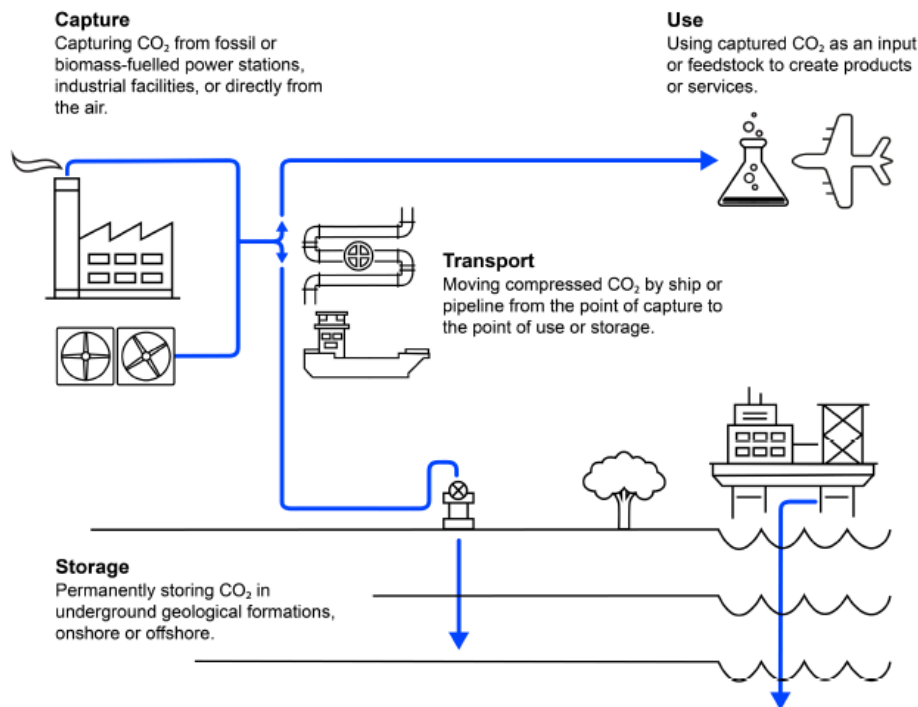


Figure 1.3: Schematic of CCUS. [9].

### 1.2.1 CO<sub>2</sub> Capture

The choice of the capture technology for different applications depends on a number of considerations. The factors influencing the choice include the desired CO<sub>2</sub> concentration in the inlet and outlet gas stream, the operating conditions in terms of pressure and temperature, the composition and flow rate of the gas stream, the integration of the system into the original facility, and also business considerations.

In Figure 1.4 the three basic systems for capturing CO<sub>2</sub> from use of fossil fuels and/or biomass are shown.

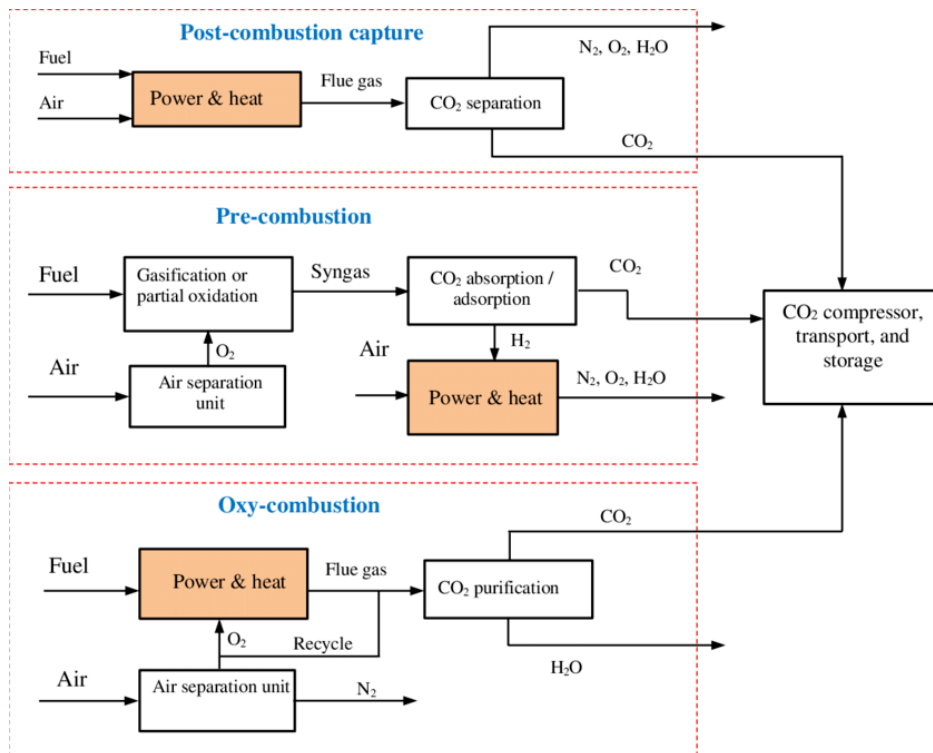


Figure 1.4: Carbon Capture Processes. [10].

More in details, in the *Post-Combustion Capture* the CO<sub>2</sub> is captured from flue gases produced by combustion of fossil fuels and biomass in air. The flue gas is treated with a chemical solvent to extract selectively CO<sub>2</sub> from nitrogen and water vapour and the separation can be performed through chemical and/or physical absorption.

The main advantage of this technology is that it can be adopted to retrofit existing power plants without requiring excessive modification and resulting in a substantial cost reduction [11, 12]. However, the major challenge for post-combustion capture is its large parasitic load. It has to be pointed out that the CO<sub>2</sub> capture requires a minimum separation work, which increases by decreasing the CO<sub>2</sub> concentration within the flue gas [13]. Since the CO<sub>2</sub> level in flue gas is usually quite low (i.e. 7 to 14% for coal-fired and 4% for gas-fired), the energy penalty and also the costs for the capture unit to reach the concentration of CO<sub>2</sub> (above 95.5%) needed both for transport and storage are elevated [14, 15].

*Pre-combustion capture* refers to removing CO<sub>2</sub> from fossil fuels before the end of the combustion exploiting the benefit of a pre-treatment of the fuel, which can be coal or natural gas. A typical block-scheme is shown in Figure 1.5.

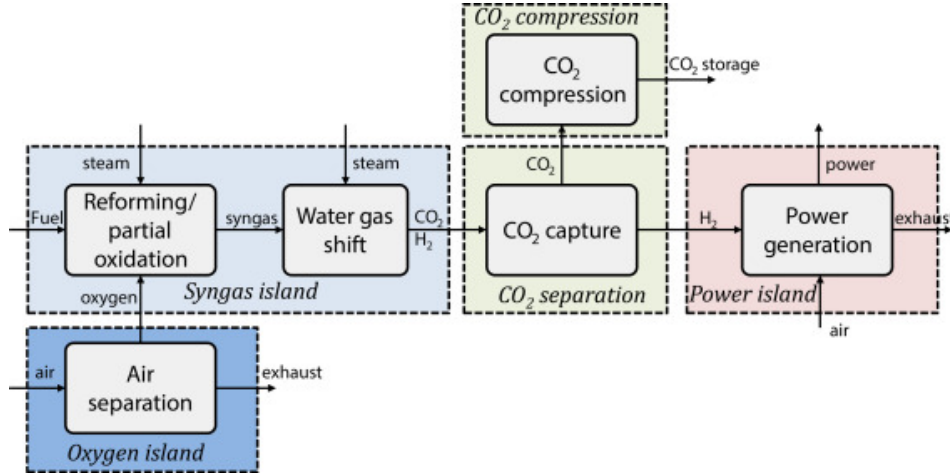
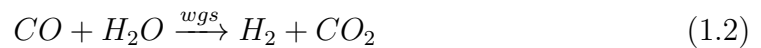


Figure 1.5: Schematic of a Pre-Combustion capture process [16].

When the fuel considered is coal, for instance, the pre-treatment consists in a gasification process in a gasifier under low oxygen level to produce syngas (Eq. 1.1). The syngas, which is a mixture consisting primarily of hydrogen and carbon monoxide, will then undergo water gas shift reaction with steam forming more H<sub>2</sub> while the CO gas will be converted to CO<sub>2</sub> (Eq. 1.2).



The high CO<sub>2</sub> concentration (>20%) in the H<sub>2</sub>/CO<sub>2</sub> fuel gas mixture facilitates the CO<sub>2</sub> separation [15].

Three main issues arise with pre-combustion CCS in connection with an integrated coal gasifier plant (IGCC):

1. *High Energy Intensity:* in the WGS reactor medium pressure is mandatory in order to convert all the CO into CO<sub>2</sub>. Moreover a H<sub>2</sub>O/CO molar ratio of 2 is required at the inlet of the reactor. Since the reactor design is generally adiabatic and the reaction is exothermic, more than one reactor is required to shift all the CO to CO<sub>2</sub>. Inter-cooling in between two subsequent reactors is also needed to re-establish a favourable thermodynamic equilibrium condition before each reactor stage. All these requisites make the process energy intensive [14, 17, 18];
2. *Requirement of a new design for the turbine:* the combined cycle must accommodate a H<sub>2</sub>-rich syngas that will develop very high firing temperature at the inlet of the turbine. Being H<sub>2</sub> a very calorific fuel, to have an almost pure-H<sub>2</sub> combustion is quite challenging. New challenges are involved in terms of materials for the blades of the turbine [18]. Alternatively, conventional alloys as those used for NG-fired turbines could be employed but better cooling strategies for the metal blades should be implemented [19];
3. *High investment costs of IGCC:* high investment costs are associated with IGCC plants and CCS systems make the economics even worse as no carbon credit is given to plants capturing CO<sub>2</sub> instead of venting it to the atmosphere [17].

The last route for CO<sub>2</sub> capture is the *Oxy-fuel combustion capture*, in which pure oxygen is used for combustion instead of air, resulting in a flue gas that is mainly CO<sub>2</sub>, H<sub>2</sub>O, particulates and SO<sub>2</sub>. Particulates and SO<sub>2</sub> can be easily removed by conventional electrostatic precipitator and flue gas desulphurization methods respectively [11], resulting in a gas stream characterized by high concentration of CO<sub>2</sub>. The latter can be then compressed, transported and stored. The main issue is represented by the huge amount of oxygen needed for the combustion. This comes from an energy intensive air separation unit [20] leading to an energy penalty which can be even 7% higher compared with a plant without CCS [21, 22].

### 1.2.2 CO<sub>2</sub> Transport

At present the two possibilities for the large-scale CO<sub>2</sub> transport are by pipeline and ship. The cheapest way for transporting large quantities of CO<sub>2</sub> is represented by pipelines. There is already an extensive onshore CO<sub>2</sub> pipeline network in North America, with a combined length of more than 8.000 [km] [9].

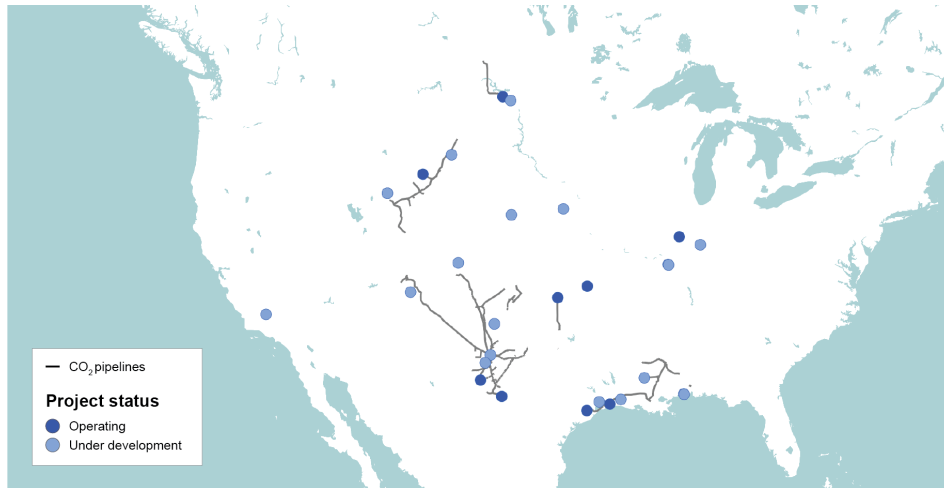


Figure 1.6: Existing CO<sub>2</sub> pipeline infrastructure and CCUS projects in the United States [23].

While transport by pipelines is already deployed, large-scale transportation of CO<sub>2</sub> by ship has not yet been demonstrated (TRL 4-7) [9]. Liquefaction is required when considering the ship transportation systems. Liquefaction is an established technology for gas transport by ship as LPG and LNG. This existing experience can be transferred to liquid CO<sub>2</sub> transport [19].

### 1.2.3 CO<sub>2</sub> Storage

CO<sub>2</sub> storage mainly consists in injecting the captured CO<sub>2</sub> into a deep underground geological reservoir. Firstly, the gas is compressed, to increase the density, and consequently turned it into a liquid. Then it is stored permanently into the reservoir, which must be at depths greater than 800 meters to keep the CO<sub>2</sub> in the liquid state. The overall storage capacity for storing CO<sub>2</sub> underground is yet not defined, but potentially very large, as shown in Figure 1.7. The main issues correlated to CCS are the resultant loss of plant efficiency, which is estimated at

between 7 and 15% , depending on the type of storage that is considered [11], but also earthquakes, engineering feasibility and costs [24].

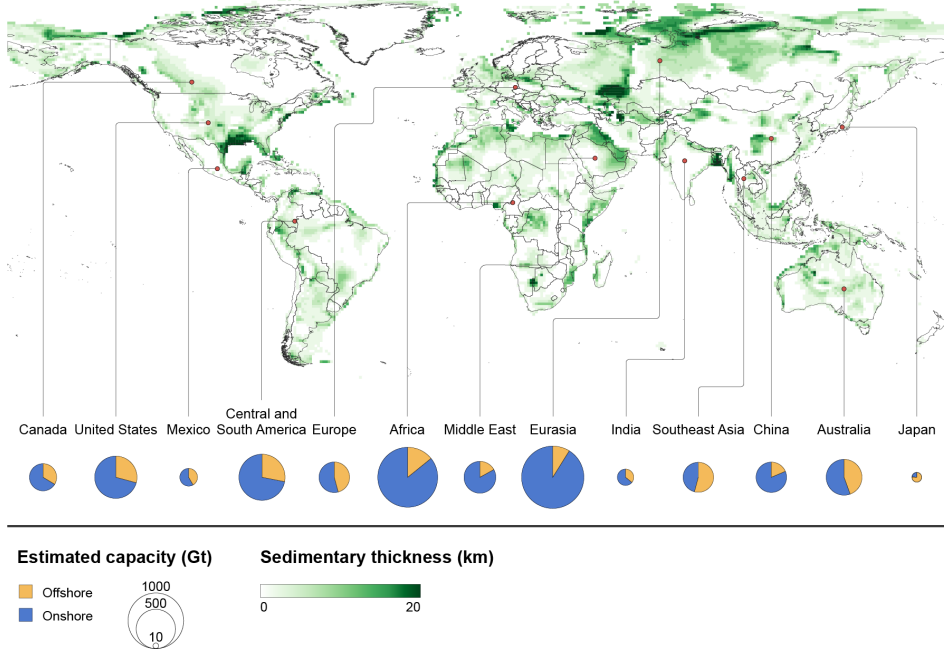


Figure 1.7: Theoretical CO<sub>2</sub> storage capacity by region [25].

## 1.2.4 CO<sub>2</sub> Utilization

For all the reasons described in the previous paragraph, CO<sub>2</sub> could have a more promising future as a carbon raw material than being considered a waste gas to be stored. The potential applications for CO<sub>2</sub> use include direct use, where the CO<sub>2</sub> is not chemically altered (non-conversion), and the transformation of CO<sub>2</sub> to a useful product (conversion). Among the many processes used for the conversion of CO<sub>2</sub>, the focus of this work is chemical looping, a process that in the past years has gained great attention in research. In Chapter 2 a detailed description of the possible applications of chemical looping processes is provided.

# Chapter 2

## Literature Review

### 2.1 The Chemical Looping Technology

A promising non-fossil alternative is represented by the so-called Synthetic Fuels; this term refers to any liquid fuel obtained from low energy content carbonaceous sources like coal, natural gas or biomass. In this context, the most used syngas is the Syngas, which is mainly a mixture of CO and H<sub>2</sub>. Syngas is a crucial intermediate resource for the production of hydrogen, ammonia, methanol, but also synthetic liquid fuels via the well known Fischer–Tropsch process. The main syngas conversion pathways are shown in Figure 2.1.

Steam Methane Reforming is the main industrial route to produce hydrogen and syngas. Although SMR is a mature technology, it suffers from significant disadvantages such as the high energy intensity and the low efficiency which lead to a strong use of fossil fuels as raw materials [27]. Thermochemical conversion of CO<sub>2</sub> can be an interesting and economical options both for syngas production and CO<sub>2</sub> reuse. Moreover it can be coupled with renewable energy sources, which can be used as high temperature energy input [28]. The conceptually simplest way to produce syngas from CO<sub>2</sub> and H<sub>2</sub>O is the direct thermal splitting but it requires extremely high temperatures (in the order of 2400°C) [29, 30]. Traynor and Reed [31] investigated a prototype system in which a solar focusing mirror and secondary concentrator were used to provide high solar intensity around a ceramic rod. This high-temperature provided strong heating of CO<sub>2</sub> with the resultant dissociation to CO and oxygen. They were able to achieve a conversion efficiency

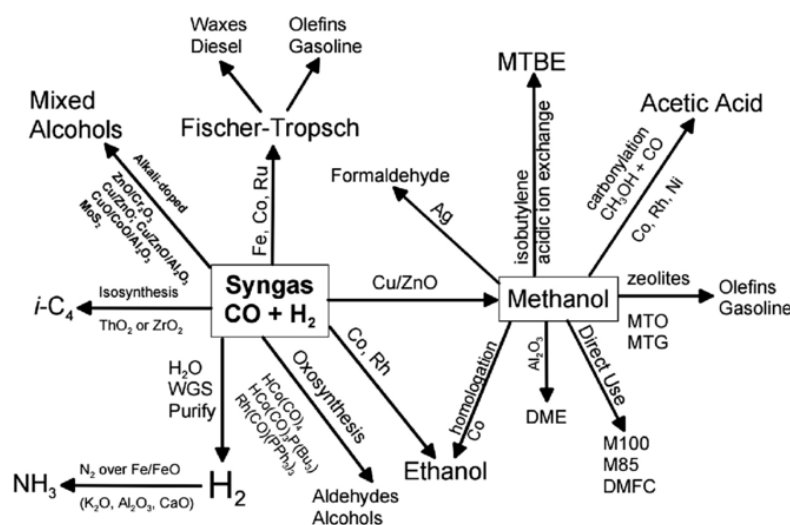


Figure 2.1: Syngas Conversion Pathways [26].

of 6% from  $\text{CO}_2$  to  $\text{CO}$  and a solar-to-chemical energy-conversion of 5%.

Chemical Looping represents an alternative solution; by predicting the thermochemical process it is possible to drastically reduce the temperatures in play. The loop mainly exploits the capability of oxygen carriers to assume different oxidation states obtaining, in this way, a closed loop of redox reactions which can be repeated, ideally, in a perpetual way by re-circularizing one of the reagents and alternating it in different oxidative states. Chemical Looping is characterized by a high efficiency, can be performed using two or three reactors and with a wide range of intermediates that can be used for the process. It is, therefore, a versatile technology which can be widely used for several practical purposes. According to the carbonaceous feed-stock reaction conditions in the reducer, chemical looping reactions can be classified into two categories: complete/full oxidation, which represents the Chemical Looping Combustion (CLC) applications, and partial/selective oxidation, representing Chemical Looping Reforming (CLR) and Chemical Looping Gasification (CLG). CL can also be applied to systems without fossil feed-stock. In this case the CL relies on sources like solar or nuclear energy as high temperature heat sources for the reducer reactor. CLC is an innovative combustion technology that can be used for  $\text{CO}_2$  capture in power generating processes.

A schematic description of the process is shown in Figure 2.2.

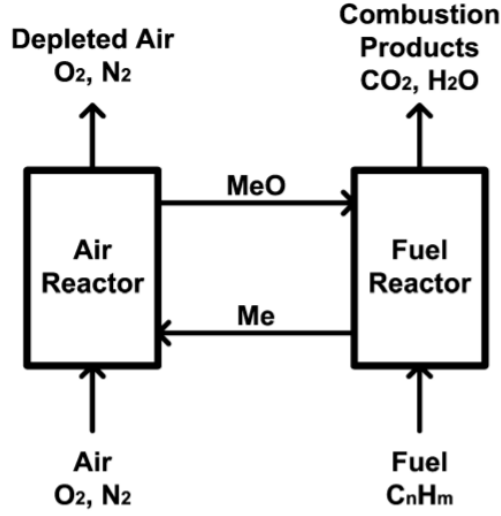
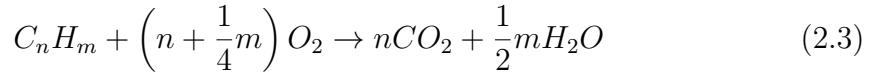
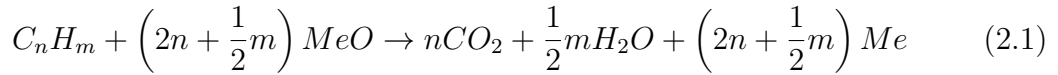


Figure 2.2: Schematic description of Chemical Looping Combustion [32].

In the configuration reported in Figure 2.2 two separate reactors are used, one for fuel and the other one for air. The abbreviation MeO is used to indicate the oxidized form of the oxygen carrier, while Me is used for the reduced form. This is because the oxygen-carrier materials are often metal oxides (NiO, Fe<sub>2</sub>O<sub>3</sub>, Mn<sub>3</sub>O<sub>4</sub>, CuO). The MeO transports oxygen between the two reactors. In the fuel reactor it is reduced by the fuel, which in turn is oxidized to CO<sub>2</sub> and H<sub>2</sub>O according to Reaction 2.1. In the air reactor, the oxygen carrier is oxidized to its initial state with O<sub>2</sub> coming from the combustion air according to Reaction 2.2.



By combining Reaction 2.1 with Reaction 2.2, the net chemical reaction (Reaction 2.3) over the two steps is obtained. The latter is equal to the conventional combustion reaction, in which the fuel is burned in direct contact with oxygen from air. Therefore, the total amount of heat evolved in the CLC process is the

same as in conventional combustion, but CLC has several potential benefits when compared to it. The gas produced in the fuel reactor consists of  $\text{CO}_2$  and  $\text{H}_2\text{O}$ . By means of cooling in a condenser it is possible to obtain almost pure  $\text{CO}_2$ , avoiding in this way the need of  $\text{CO}_2$  separation units and without any penalty in energy. Another feature of this technology is that the direct contact between fuel and air is avoided and the combustion products are not diluted with  $\text{N}_2$ . CLR is based on the same basic principles as CLC; the difference lies precisely on the useful product which, for CLR is not heat but syngas. In the CLR process the air to fuel ratio is kept low to avoid the complete oxidation of the fuel to  $\text{CO}_2$  and  $\text{H}_2\text{O}$ . It consists basically in a partial oxidation of hydrocarbon fuels where an oxygen carrier is again used as a source of oxygen, avoiding the need for expensive and power demanding air separation units. The basic principles of CLR are illustrated in Figure 2.3.

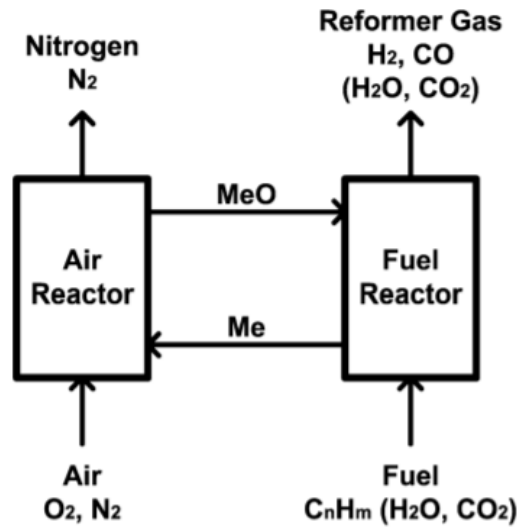
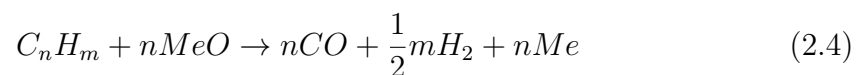


Figure 2.3: Schematic description of Chemical Looping Reforming [32].

In the air reactor Reaction 2.2 will occur, as in the CLC process. In the fuel reactor, part of the fuel may become completely oxidized to  $\text{CO}_2$  and  $\text{H}_2\text{O}$ , but a large share should react according to Reaction 2.4.

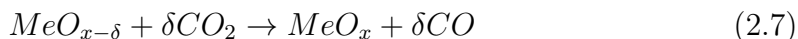
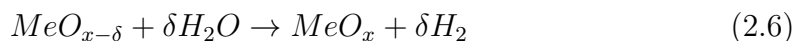
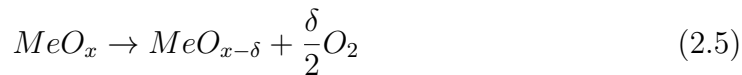


An important aspect to be considered in the CLR system is the heat balance of

the process; the oxidation reaction of the MeO is strongly exothermic, while the reduction reaction is endothermic. The heat generated in the air reactor must be high enough to fulfil the heat balance in the system, without requirement of any external energy source. These aspects have been investigated by [33]; they carried out a detailed mass and heat balance study of a Chemical Looping Methane Reforming process to determine the auto-thermal operating conditions that maximize the H<sub>2</sub> production working with a Ni-based oxygen carrier. The result of their analysis shows that the oxygen-to-methane molar ratio should be higher than 1.25 to reach auto-thermal conditions, which corresponds to a H<sub>2</sub> yield of 2.7 mol H<sub>2</sub>/mol CH<sub>4</sub>.

## 2.2 Solar two-step H<sub>2</sub>O/CO<sub>2</sub> splitting cycles with metal-oxides

As previously said, the single-step thermal dissociation of water and carbon dioxide is conceptually the simplest reaction to produce syngas, but the requirement of extremely high temperatures as well as the problem of effectively separating H<sub>2</sub> and O<sub>2</sub> to avoid explosive mixtures make it impractical. Conversely, thermochemical cycles are a series of consecutive chemical reactions ( $\geq 2$ ) in which the maximum-temperature step takes place at a temperature lower than that of the single-step H<sub>2</sub>O and CO<sub>2</sub> dissociation. For this reason, CL processes are used for syngas production and may include CO<sub>2</sub> or H<sub>2</sub>O energy-upgrading through solar thermochemical cycles. The preferred setup for this type of process consists of a circulating closed loop between two interconnected reactors. In these reactors the metal oxide is subjected alternatively to reduction and oxidation step, according to the following reactions:



The process is driven by the capability of the oxygen carrier to assume different oxidation states; it spontaneously releases oxygen molecules during the thermal reduction (Reaction 2.5) at high temperature level (above 1300°C), with the corresponding generation of oxygen vacancies. The deviation from stoichiometry,  $\delta$ , otherwise known as the oxygen storage capacity, is directly related to the maximum amount of fuel capable of being produced. Thus, process efficiencies are directly related to the oxygen storage capacities. After the reduction step, the reduced oxygen carrier is re-oxidized in the low temperature oxidation reactor at around 1000°C, splitting in this way H<sub>2</sub>O and CO<sub>2</sub> (Reaction 2.6 and 2.7 respectively). The high temperature energy input required in the reduction step can be provided by the integration with a CSP system. The schematic description of the CSP-aided, two-step, redox-pair-base, water splitting CL process is shown in Figure 2.4.

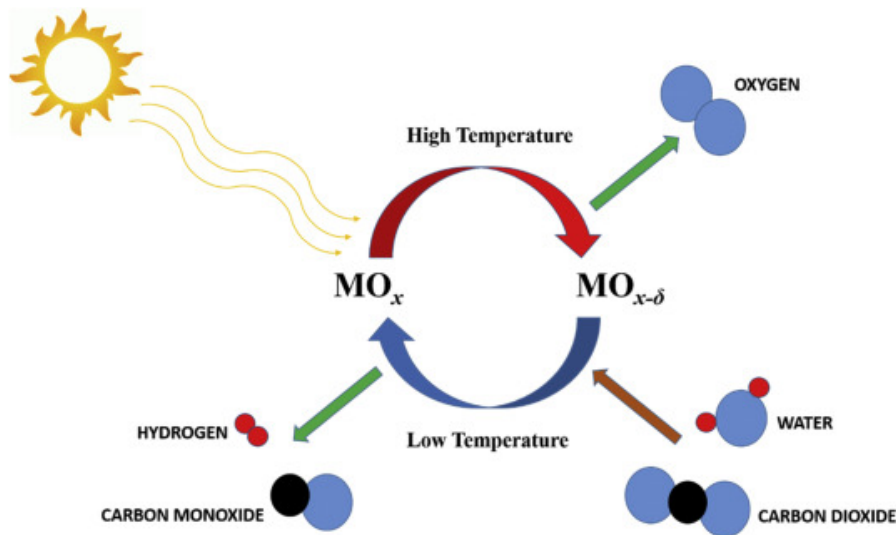
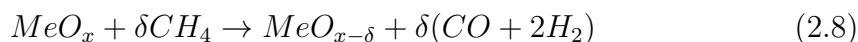


Figure 2.4: Schematic description of the CSP-aided, two-step, redox-pair-base, water splitting CL process [34].

As stated earlier, the TR reaction requires and it is favoured at high temperatures and with a very low partial pressure of oxygen in the mixture. On the contrary, the WS and CDS reactions require low temperature levels and high oxygen partial pressure. This leads to swings of temperatures and pressures between the two reactors. One option to reduce the temperature in the reduction step is

to introduce a reducing agent, such as  $H_2$ , which not only allow to reach the conditions for which the temperatures of the two steps can coincide, but it also make it possible to operate at almost atmospheric pressure. This leads to a substantial simplification of the requirements of the process; for this reason it has been chosen as a solution to be implemented in this work. Another option to decrease the temperature of the reduction reaction is by considering the convergence of two approaches: solar fuels via the redox cycles and the CLR of methane. Krenzke et al. [35] found out that coupling the reduction of ceria to the partial oxidation of methane enables isothermal cycling at temperatures as low as  $950^\circ\text{C}$  with the additional production of high-quality syngas during the reduction and with an estimated solar-to-fuel efficiency reaching 40% without any heat recovery. The main difference with respect to the CL process is the conversion of  $CH_4$  into syngas, according to Reaction 2.8.



Reaction 2.8 is then followed by Reaction 2.6 and Reaction 2.7.

As mentioned in the paragraph 2.1, CLR is a valid alternative to the SMR high energy intensity process for the syngas production. Moreover, Reaction 2.8 is favoured at lower pressure levels, allowing to reduce the pressure swing between the two reactors. The main drawback of this hybrid technology is the carbon deposition, which is the deposition of solid carbon particles, by means of the methane decomposition (Reaction 2.9) or by Boudouard equilibrium (Reaction 2.10).



Carbon deposition phenomenon causes a decrease in the redox performance of the oxygen carrier and must be avoided. Ishida et al. found out that carbon deposition behavior depends significantly on the combination of the solid reactant. NiO/YSZ was proved to be a good candidate for chemical-looping combustion, obtaining the total absence of carbon deposition under the condition of  $H_2O/CO$  ratio equal to 0,5 at  $600^\circ\text{C}$  [36].

## 2.3 Materials for Chemical Looping

The key issue of the system performance is for sure the oxygen-carrier material. It must accomplish the following characteristics:

- Sufficient oxygen transport capacity;
- High reactivity for reduction and oxidation reactions;
- Physical and chemical properties stability during many successive redox cycles;
- Limited cost;
- Environmental friendly characteristics.

Although other carriers continue to generate significant scientific research interest [37, 38, 39], metal oxide-based materials dominate the research spectrum, especially because they are suitable for applications involving carbon capture. The pure metal oxides show decreasing reaction rates in few cycles [40, 41], not fulfilling the above mentioned characteristic. A porous support is used to provide a higher surface area for reaction, a binder for increasing the mechanical strength and attrition resistance, and also increases the ionic conductivity of solids [42]. In literature it is possible to find multiple studies of oxygen carriers materials. Over 350 thermochemical redox cycles are known to be thermodynamically capable of dissociating  $\text{H}_2\text{O}$  to produce  $\text{H}_2$  [43]. Of these potential cycles, only a minority operate in two steps while the remainders occur in 3 or more steps. In general, two step cycles can be divided into two distinct classes of metal-oxide redox pairs namely volatile and non-volatile.

### 2.3.1 Volatile Oxygen Carriers

Volatile oxygen carriers are also called phase-changing metal oxide because they are characterized by a phase change from solid to vapor when moving from oxidized to reduced state. The key feature of these materials is the possibility to have a stoichiometric reduction, resulting in a greater oxygen exchange capability than non-volatile reactions. However, to do so a reduction temperature higher than

the vaporization temperature is required. The high endothermicity in reduction of these materials is not only an issue from the feasibility point of view, but it implies also the requirements of a fast cooling immediately after the reduction to avoid the recombination of the oxygen released with the oxygen vacancies on the metal oxide, which is favoured at high temperatures [44]. The most common materials with volatile characteristics include zinc oxides, germanium oxides, cadmium oxides, and tin oxides.

## Zinc Oxides

ZnO/Zn is a potential candidate for a working redox pair in two-step thermochemical water splitting. This system has been extensively examined and developed, mainly by the Paul Scherrer Institute (PSI) in Switzerland [45, 46]. In Figure 2.5 the two-step solar thermochemical cycle based on Zn/ZnO redox reactions for H<sub>2</sub> and CO production is shown.

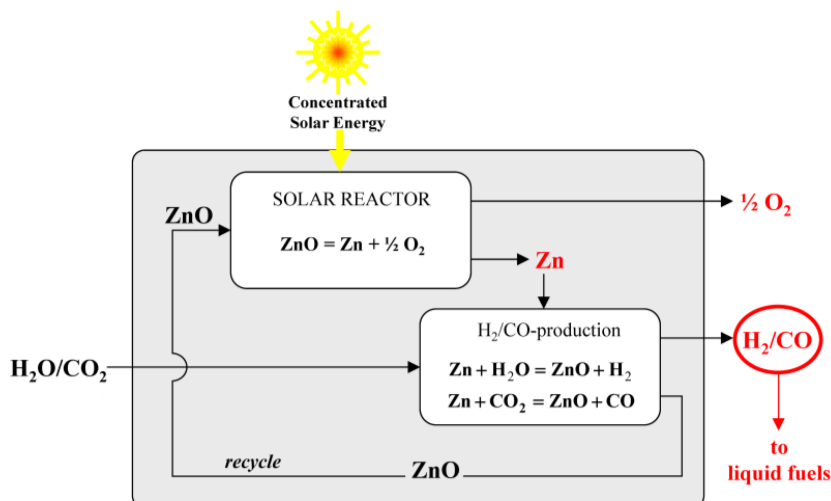


Figure 2.5: Schematic of the two-step solar thermochemical cycle based on Zn/ZnO redox reactions to produce H<sub>2</sub> and/or CO from H<sub>2</sub>O and/or CO<sub>2</sub> [46].

When using ZnO, the solar reactor operating temperature has to be in the range 2000–2300 K, as the thermal dissociation of ZnO proceeds at reasonable rates above 2000 K, limiting in this way the conversion efficiency [47]. Moreover, Villasmil et al. [48] demonstrated that the achievement of pure Zn via TR of ZnO is very difficult. The solid products of the solar-driven thermochemical decomposition of

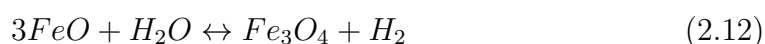
ZnO consisted of a mixture containing ZnO and Zn, with a percentage of Zn in the range 12–49% due to partial re-oxidation of Zn in the presence of O<sub>2</sub> in the quenching step. Bhosale [49] examined the influence of partial reduction of ZnO on the thermodynamic parameters. He found out that the solar-to-fuel efficiency increases by 42.4% due to the rise in the the percentage of ZnO reduction from 0.4% to 57.2%.

### 2.3.2 Non-Volatile Oxygen Carriers

In non-volatile cycles, the redox intermediate remains in the solid phase throughout the reduction step. The reduction temperature required is therefore lower than the one of the volatile materials. Non-volatile metal oxides cycles can be further divided into stoichiometric and non-stoichiometric cycles. Stoichiometric reactions involve a change in crystal structure, forming a solid solutions upon reduction. They are characterized by a greater oxygen exchange with respect to that of non-stoichiometric reactions but they typically exhibit slower reaction kinetics and poor stability [50]. The most used non-volatile stoichiometric pairs include iron oxides and ferrite. Non-stoichiometric reactions, with metal oxides such as perovskites or CeO<sub>2</sub>, are characterized by the partial reduction of the bulk metal-oxide, while maintaining the crystallographic structure.

#### Iron Oxides

As previously said, Iron Oxides belong to non-volatile stoichiometric oxygen carriers. The solar thermochemical cycle for WS using iron oxide was firstly proposed by Nakamura [51] and it can be represented by reactions 2.11 and 2.12.



Kodama report on the thermodynamic analysis of the cycle [52]. In the study it is indicated that the first high-temperature step of the thermal decomposition of magnetite (Fe<sub>3</sub>O<sub>4</sub>) to wustite (FeO), proceeds at temperatures above 2500 K

under 1 bar, while the hydrolysis reaction thermodynamically proceeds at temperatures below 1000 K. Since the very-high reduction temperature creates engineering challenges [53, 54], any possibility of lowering the reduction temperature is desirable. The first option consists in varying the partial pressure of oxygen in the atmosphere; the iron-oxygen phase diagram [55] shows, in fact, that the FeO single phase can be formed at temperature equal to 1400°C or higher if the oxygen partial pressure ranges from  $10^{-6}$  to  $10^{-8}$  bar [56]. Another possible option is the implementation of mixed oxides, based on solid solutions between the redox system  $\text{Fe}_3\text{O}_4/\text{FeO}$  and  $\text{M}_3\text{O}_4\text{-MO}$  (M= Mn, Co, Mg). This solution have been examined to exploit the combination of good  $\text{H}_2$  yields in the  $\text{Fe}_3\text{O}_4/\text{FeO}$  system with the low reduction temperature in a  $\text{M}_3\text{O}_4\text{-MO}$  [57]. More specifically, Ehrensberger et al. [58] studied the  $\text{Mn}_3\text{O}_4\text{-Fe}_3\text{O}_4$  system, and found out that, at atmospheric pressure, steam with a partial pressure of about 4200 Pa was able to oxidize  $(\text{Fe}_{1-x}\text{Mn}_x)_{1-y}\text{O}$  to  $(\text{Fe}_{1-z}\text{Mn}_z)_3\text{O}_4$  with  $x>z$ , forming hydrogen in the temperature range of 773–1173 K. Moreover in the study it has been demonstrated that the partial substitution of iron for manganese, at 10 and 30 mol% respectively, in the wustite phase did not lower the total amount of hydrogen formed per mole of transformed oxide in the hydrolysis reaction, leading however to a significantly slower kinetics of the process. In addition to the need for a lower reduction temperature, another significant problem of this redox pair is rapid deactivation due to the significant high-temperature melting and sintering of the metal oxide, which directly affect the repeatability of the cycle. Kodama et al. [59] have addressed this problem, and they proposed a WS cycle with  $\text{Fe}_3\text{O}_4$  supported on fine particles of monoclinic  $\text{ZrO}_2$  (m- $\text{ZrO}_2$ ). The  $\text{ZrO}_2$  support alleviates sintering of the iron oxide during the high-temperature reactions, resulting in a good activity and repeatability through the cyclic reaction in the temperature range of 1000–1400°C.

### 2.3.3 Perovskites

Among well-known oxygen carriers of Zn, Ni, Fe, the perovskite materials for syngas production have only been studied recently, but with fast-growing interest. The reason is that the perovskite structure is characterized by attractive features such as energetic stability, reliability and durability at high processing temperatures. Unlike ceria, most of perovskites are characterized by not favorable thermodynamics, requiring either a large temperature swing between reduction and oxidation

steps or an excess of oxidant to complete re-oxidation and to increase the fuel production rate [61]. However, perovskite oxides are a very versatile material class able to structurally accommodate a large variety of elements of the periodic table, offering great potential for tuning their thermodynamic properties. Another advantage of most perovskite compositions is the shift to lower operation temperatures, leading to a simplification of the requirements for solar-to-fuel reactors design. Perovskite-structured materials are typically formulated as  $ABO_3$ , where A is a large alkaline earth or rare earth element and B is a smaller transition metal cation. The ideal cubic structure crystallize in the space group  $Pm\bar{3}m$  and is shown in figure 2.6. In this structure, the B cation is in 6-fold coordination and the A cation is in 12-fold cuboctahedral coordination.

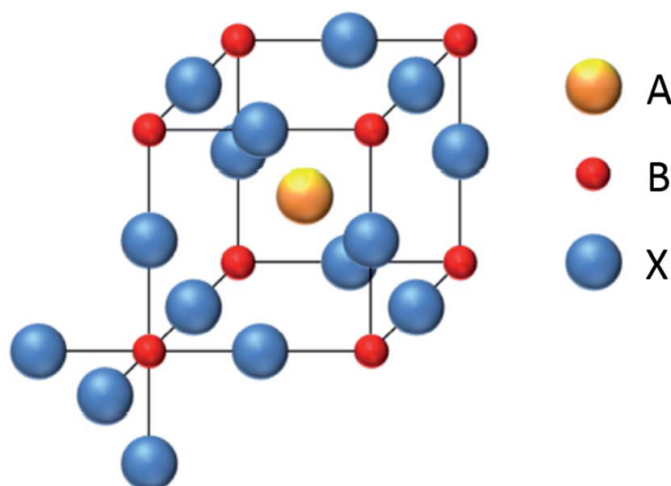


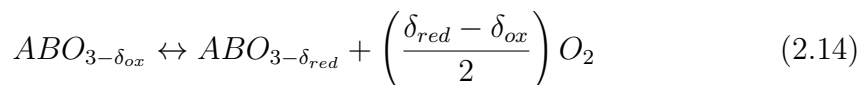
Figure 2.6: The ideal cubic structure of an  $ABX_3$  perovskite. For oxides, X is to the oxide ion  $O^{2-}$ , A is a large 12-fold coordinated cation, and B is a small 6-fold (octahedral) coordinated cation. [60].

As already mentioned, this kind of structure enable to modify the perovskite composition by means of incorporating a large number of chemical elements and different cations on the A-site or B-site in the crystal lattice. Doping the perovskite allows to obtain different structures that may enhance electronic, ionic or magnetic properties of the material. In this context, Goldschmidt introduced a tolerance factor  $t$ , based on the ionic radii of the A and B side cations [62]. The idea behind the Goldschmidt tolerance factor is to connect the structural flexibility to the ionic radii of the involved ions. The tolerance factor  $t$  is evaluated according to Equation

2.13, where  $r_A$ ,  $r_B$ ,  $r_O$  represents the ions for the general perovskite formula  $ABO_3$ .

$$t = \frac{r_A + r_O}{\sqrt{2}(r_B + r_O)} \quad (2.13)$$

The tolerance factor is  $t=1$  for an ideal cubic perovskite, while deviations of  $t$  from the unit value correspond to an increased tendency for structural distortion, leading to orthorhombic, rhombohedral, tetragonal, monoclinic or triclinic symmetries. The redox cycle for syngas production by using non-stoichiometric perovskite as oxygen carrier consists of a first high temperature reduction step (Reaction 2.14) and the following oxidation step (Reaction 2.15 and/or 2.16).



The high number of doping possibilities in perovskite materials is the most interesting property for thermochemical cycles; the large composition space of at least 27 suitable elements for the A-site, and 35 elements for the B-site [63] enables perovskites to tune their thermodynamic properties. Here follows a detailed overview of one the best performing perovskite formulations, with a special focus on their ability to produce solar fuel with high yield and stable performance by means of A-site and B-site substitutions.

### Lanthanum–Manganite Perovskites

Lanthanum-manganite perovskites have been extensively investigated for numerous applications such as electrodes in SOFC [64] and metal-air batteries [65]. Concerning the two step thermochemical cycles applications,  $LaMnO_3$  is characterized by a very low reduction extent, which prevents the fuel production [63]. For this reason, among the lanthanum-manganite perovskites series, the most studied are the A-site substituted materials with Sr but also with Ca. Indeed, Strontium-doped lanthanum-manganite perovskites, often referred to as LSM, show encouraging  $Mn^{4+}/Mn^{3+}$  redox activity during two-step thermochemical  $CO_2$  dissociation

for solar fuel production. Demont and Abanades examined the thermochemical cycles of  $La_{1-x}Sr_xMnO_3$  ( $x=0.35, 0.50, 0.65, 0.80$ ), collecting weight variations resulting from reduction or oxidation by TGA [66]. From the results of their study, LSM50 appeared to be the most suitable trade-off for thermochemical  $CO_2$  splitting. Dey and Rao [67] studied the  $La_{1-x}Sr_xMnO_3$  ( $x=0.3, 0.4, 0.5$ ) towards CDS at isothermal operating condition and obtained  $CO$  production  $n_{CO}=134 \mu\text{mol/g}$  per cycle by LSM50 at  $1400^\circ\text{C}$ . As per several studies, increasing the Sr-content enhance the reduction properties. Indeed, the controlled introduction of Sr in the A-site increases the oxidation state of Mn, due to the lower charge of  $Sr^{2+}$  with respect to  $La^{3+}$ , resulting in a enhancement of  $O_2$  production rate, as shown in Figure 2.7.

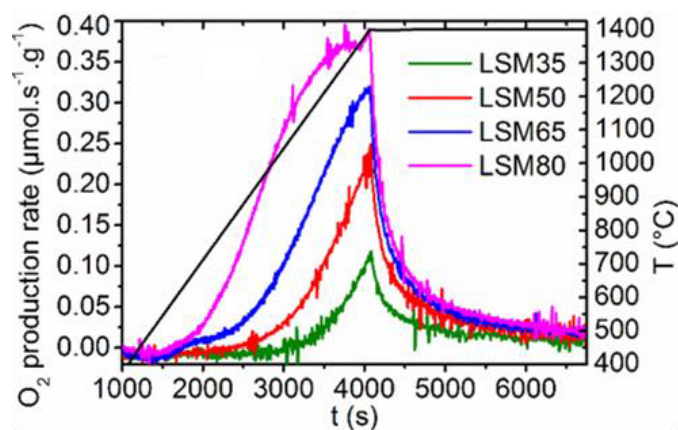


Figure 2.7:  $O_2$  production rates in LSM perovskites with different content of Sr. [66].

However, re-oxidation yield decreases steeply with the increase of Sr-content. Data reported in Figure 2.8 strongly suggest that thermodynamics for full re-oxidation are increasingly unfavorable as the Sr-content is raised. While LSM35 shows an almost complete re-oxidation yield, for the samples with higher Sr-doping only slight portions of the oxygen released by the crystal lattice during the reduction are recovered when performing the  $CO_2$  dissociation step.

A recent study by Takalkar et al. [68] concentrated on the exploration of the thermal reduction and re-oxidation behavior of the LSM perovskites in multiple CS cycles. Obtained results provide further confirmation that the rise in the Sr molar concentration is favorable to improve the thermal reduction yield of the LSM

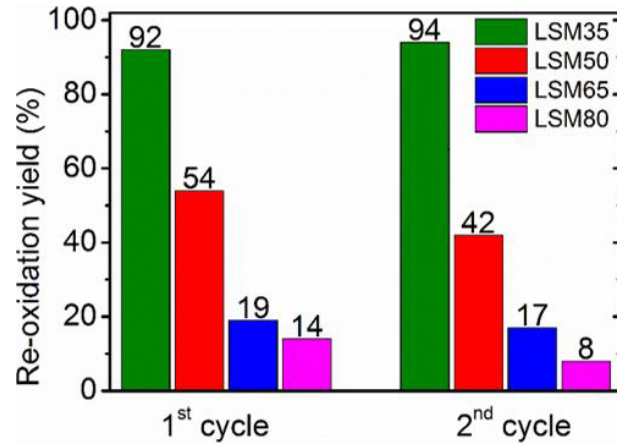


Figure 2.8: Re-oxidation yields of the perovskites under  $\text{CO}_2$  exposure. [66].

perovskites. The long term thermal cycling (from cycle 2 to cycle 10) shows that the LSM40 perovskite was the best choice in terms of evolved oxygen ( $n_{\text{O}_2}=214.8 \mu\text{mol/g}$  per cycle), whereas LSM70 showed the highest activity towards CS reaction ( $n_{\text{CO}}=342.1 \mu\text{mol/g}$  per cycle). The results both in terms of  $\text{O}_2$  and  $\text{CO}$  production are shown in Figure 2.9a and 2.9b respectively.

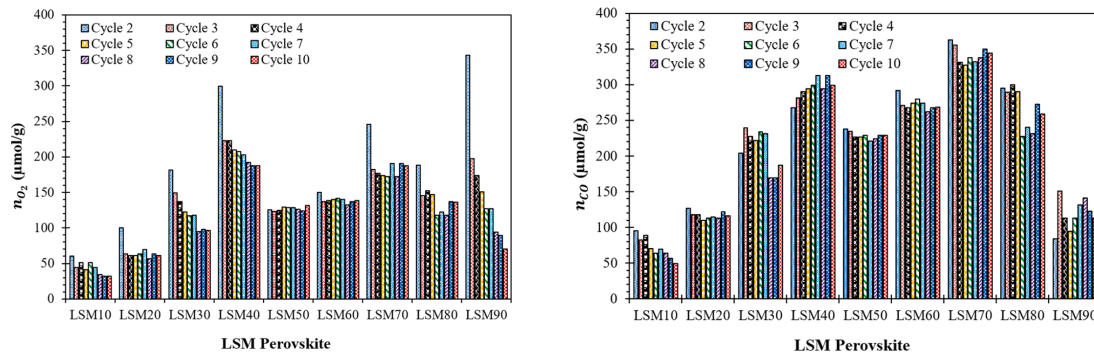


Figure 2.9:  $\mu\text{mol/g}$  of  $\text{O}_2$  evolved and  $\text{CO}$  produced by LSM perovskites from cycle 2 to cycle 10 ( $T_{\text{red}}=1400^\circ\text{C}$  for 60 min,  $T_{\text{oxy}}=1000^\circ\text{C}$  for 30 min, and heating/cooling rate =  $25^\circ\text{C}/\text{min}$ ). [68]

Another possibilities to enhance the fuel production in lanthanum-manganite perovskites is the A-site partial substitution with  $\text{Ca}^{2+}$  or with  $\text{Ba}^{2+}$  cations. In general LCM, which stands for  $\text{La}_{1-x}\text{Ca}_x\text{MnO}_3$ , displayed better reducibility with respect to the Sr dopant, but the amount of evolved  $\text{CO}$  was lower in comparison

with LSM [69, 70]. Concerning the presence of  $\text{Ba}^{2+}$ , it does not show any positive effect on the reduction extent or on the re-oxidation yield when compared with LSM and LCM [63]. In Table 2.1 a summary of the  $\text{O}_2$  and  $\text{CO}$  yields found in literature is provided.

LM Perovskite	Abbrev.	$T_{red}/T_{oxy}$ °C	$n_{\text{O}_2}$ μmol/g	$n_{\text{CO}}$ μmol/g	Ref
$\text{La}_{0.9}\text{Sr}_{0.1}\text{MnO}_3$	LSM10	1400/1000	47.6	95.6*	[68]
$\text{La}_{0.8}\text{Sr}_{0.2}\text{MnO}_3$	LSM20	1400/1000	66.6	116.7*	[68]
$\text{La}_{0.7}\text{Sr}_{0.3}\text{MnO}_3$	LSM30	1400/1000	123.7	209.4*	[68]
$\text{La}_{0.6}\text{Sr}_{0.4}\text{MnO}_3$	LSM40	1400/1000	214.8	294.6*	[68]
$\text{La}_{0.5}\text{Sr}_{0.5}\text{MnO}_3$	LSM50	1400/1000	126.9	228.7*	[68]
$\text{La}_{0.4}\text{Sr}_{0.6}\text{MnO}_3$	LSM60	1400/1000	139.4	272.9*	[68]
$\text{La}_{0.3}\text{Sr}_{0.7}\text{MnO}_3$	LSM70	1400/1000	187.9	342.1*	[68]
$\text{La}_{0.2}\text{Sr}_{0.8}\text{MnO}_3$	LSM80	1400/1000	140.5	267.4*	[68]
$\text{La}_{0.1}\text{Sr}_{0.9}\text{MnO}_3$	LSM90	1400/1000	37.9	75.9*	[68]
$\text{La}_{0.7}\text{Sr}_{0.3}\text{MnO}_3$	LSM30	1400/1400	37.9	75.9*	[67]
$\text{La}_{0.6}\text{Sr}_{0.4}\text{MnO}_3$	LSM40	1400/1400	48.9	98.2*	[67]
$\text{La}_{0.6}\text{Sr}_{0.4}\text{MnO}_3$	LSM40	1400/1000	205	397	[71]
$\text{La}_{0.5}\text{Sr}_{0.5}\text{MnO}_3$	LSM50	1400/1400	69.5	134.8*	[67]
$\text{La}_{0.5}\text{Sr}_{0.5}\text{MnO}_3$	LSM50	1400/1050	199.5	242*	[66]
$\text{La}_{0.5}\text{Sr}_{0.5}\text{MnO}_3$	LSM50	1400/1100	201	325	[71]
$\text{La}_{0.5}\text{Sr}_{0.5}\text{MnO}_3$	LSM50	1400/873	236	224	[71]
$\text{La}_{0.5}\text{Ca}_{0.5}\text{MnO}_3$	LCM50	1400/1050	221.5	189*	[69]
$\text{La}_{0.5}\text{Ba}_{0.5}\text{MnO}_3$	LBM50	1400/1050	159	167*	[69]

Table 2.1: LM A-substituted perovskites: μmol/g of  $\text{O}_2$  and  $\text{CO}$  evolved during thermochemical redox cycling. Comparison between the findings reported by Takalkar et al. [68], Dey and Rao [67], Farooqui [71] and Demond et al. [66, 69]. Yields indicated with \* were obtained by means of TGA.

Finally, the introduction of A-site dopants leads to an increase of  $\text{Mn}^{4+}$  to maintain charge balance. This increased  $\text{Mn}^{4+}$  can then lead to vacancy formation

through the redox couple  $\text{Mn}^{4+}/\text{Mn}^{3+}$ , enhancing the  $\text{O}_2$  production.

The effect is more complicated when in the case of B-site doping. Cimino et al. [72] investigated the structural, redox and catalytic oxidation properties of LMA, which stands for  $\text{LaAl}_{1-x}\text{Mn}_x\text{O}_3$ , with Al-doping content in the range  $x=0-1$ . The results of their study demonstrated that the presence of Al in the LMA solid solutions produces a strong promoting effect on the  $\text{Mn}^{4+}$  to  $\text{Mn}^{3+}$  reducibility, while inhibiting the further reduction to  $\text{Mn}^{2+}$ . McDaniel et al. performed 80 cycles and showed that LMS with B-site partial substitution with  $\text{Al}^{3+}$  could effectively split both  $\text{CO}_2$  and  $\text{H}_2\text{O}$  with high yields and fast kinetics [73]. More specifically the materials tested in their study were  $\text{Sr}_{0.4}\text{La}_{0.6}\text{Mn}_{0.6}\text{Al}_{0.4}\text{O}_3$ , labelled as SLMA1;  $\text{Sr}_{0.6}\text{La}_{0.4}\text{Mn}_{0.6}\text{Al}_{0.4}\text{O}_3$ , labelled as SLMA2;  $\text{Sr}_{0.4}\text{La}_{0.6}\text{Mn}_{0.4}\text{Al}_{0.6}\text{O}_3$ , labelled as SLMA3. The results of the tests performed in terms of CO production rate is shown in Figure 2.10. Results for ceria are shown in the same picture for comparison.

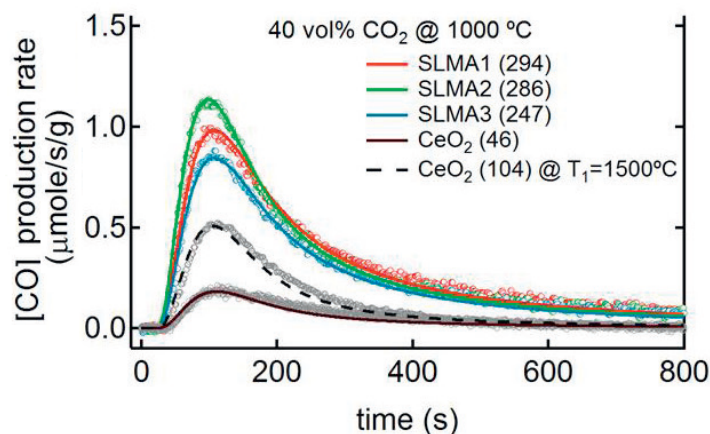


Figure 2.10: CO production rates as a function of time measured during oxidation in 40 vol%  $\text{CO}_2$  at  $1000^\circ\text{C}$ . SLMA1-3 thermally reduced at  $1350^\circ\text{C}$  in He.  $\text{CeO}_2$  thermally reduced both at  $1350^\circ\text{C}$  and  $1500^\circ\text{C}$  in He. The total amount of CO produced in  $\mu\text{mol/g}$  of material is shown in parentheses. [73].

As it is clearly visible from the graph, nearly 6 times more CO is produced by the Al-doped LSM compounds as compared to  $\text{CeO}_2$  when reduced at  $T_{red}=1350^\circ\text{C}$  and oxidized at  $T_{oxy}=1000^\circ\text{C}$ . The fuel production rates for  $\text{CeO}_2$  reduced at  $T_{red}=1500^\circ\text{C}$  are also reported in Figure 2.10 in the round brackets. Also in this case the SLMA compounds outperform ceria producing a total amount of CO equal

to  $n_{CO}=294 \mu\text{mol/g}$  in the case of the best performing material. Moreover also the stability of Al-doped LSM has been tested by means of a short-term durability study on SLMA2 undergoing  $\text{CO}_2$  splitting at  $T_{red}=1350^\circ\text{C}$  and  $T_{oxy}=1000^\circ\text{C}$ . The almost constant level of CO, as shown in figure 2.11, produced during the course of the experiment is encouraging and indicates there are no fast material degradation mechanisms at play.

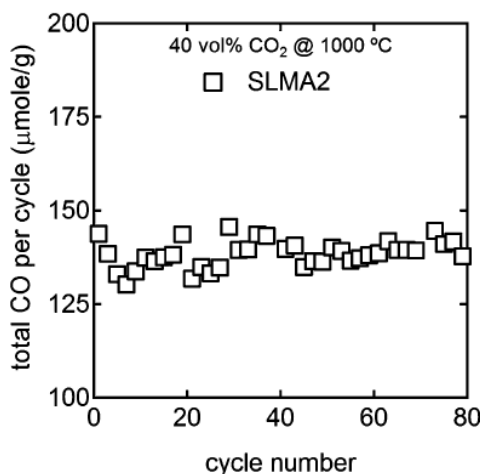


Figure 2.11: Total amount of CO produced per cycle for SLMA2. Material was reduced at  $T_{red}=1350^\circ\text{C}$  in He and oxidized in 40 vol%  $\text{CO}_2$  at  $T_{oxy}=1000^\circ\text{C}$ . Dwell times for thermal reduction and oxidation were 15 min each resulting in a 30 min redox cycle. [74].

Cooper et al. [75] provide further experimental evidence to support the study of McDaniel et al. They experimentally tested the  $\text{La}_{1-x}\text{Sr}_x\text{Mn}_{1-y}\text{Al}_y\text{O}_3$ , thereby confirming the excellent behavior of LSMA, which not only appears to be the most promising material in terms of degree of reduction, but also in terms of fuel production and cyclic performance. In order to improve the thermodynamic driving force for fuel production and simultaneously enhance the splitting kinetics, Carrillo et al. [76] explored the partial substitution of Mn by Cr in the LSM perovskite structure. Thermochemical cycling tests were performed to the  $\text{La}_{0.6}\text{Sr}_{0.4}\text{Cr}_x\text{Mn}_{1-x}\text{O}_3$  materials from  $x=0$  to  $x=0.85$ , in which  $\text{O}_2$  and CO production were monitored for eight consecutive cycles. The first three cycles were performed at isothermal conditions, evaluating the influence of the reduction and oxidation temperatures. The results obtained by Carrillo et al. show that the temperature increase leads to higher

and faster CO production for every LSM Cr-doped sample. It also demonstrated that performing reduction at higher temperatures leads to higher O<sub>2</sub> release, still not comparable to the values obtained when testing the LSM sample. This result illustrates the importance of finding a trade-off between materials with high yields, that require short exposure to CO<sub>2</sub>, and materials with high oxygen exchange capacity. The optimum CO yields was observed for x=0.3 at 1200°C with 4.6 mL/g. In figure 2.12 the total CO production (Figure 2.12a) and O<sub>2</sub> release (Figure 2.12b) is shown for the samples isothermally cycled at 1400°C.

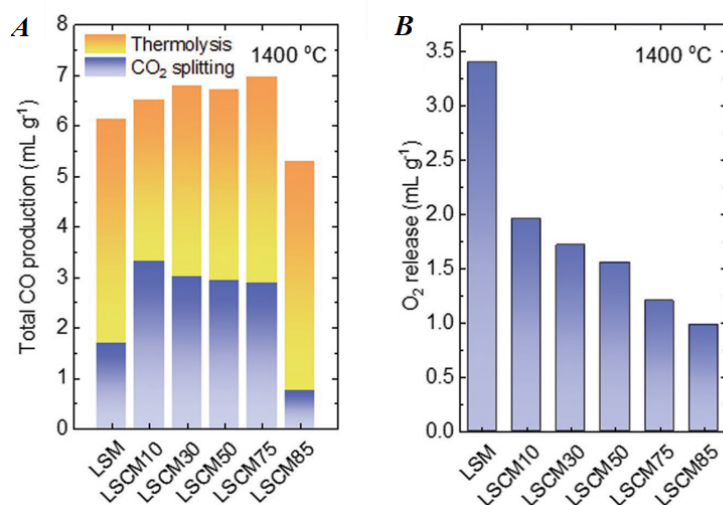


Figure 2.12: LSM Cr-doped perovskites: a) results of the isothermal cycles at 1400°C in terms of CO production, differentiating the contribution of the CO produced from the two-step CO<sub>2</sub>-splitting. b) results of the isothermal cycles at 1400°C in terms of O<sub>2</sub> evolved. [76].

It has to be pointed out that they observed the concomitant generation of O<sub>2</sub> in the isothermal CO<sub>2</sub> splitting, especially at 1300°C and 1400°C. This is due to the thermolysis of CO<sub>2</sub> (Reaction 2.17). This phenomenon has never been observed on perovskite before since previous studies rely on TGA, that cannot monitor catalytic processes unrelated to weight changes, while it has already been reported for isothermal cycles with ceria or heryncite [77, 78].



For this reason, Figure 2.12 a) depicts the total CO produced differentiating both sources, thermolysis and CO<sub>2</sub> splitting. The highest fuel production at 1400°C was observed for Cr x=0.1 with 3.3 mL/g of CO. In order to evaluate the influence of the Cr content to the kinetics the CO rate production curve for the samples with the lowest (x=0 and x=0.1) and the highest (x=0.75 and x=0.85) amount of Cr has been plotted. Figure 2.13 illustrates an increase in CO production rate while increasing Cr-content, confirming the positive influence of Cr-doping on improving the CO<sub>2</sub>-splitting kinetics; moreover the results indicate that by varying the Cr-content it would also be possible to optimize the CO<sub>2</sub>-splitting reaction time. Indeed, the fastest kinetic performance can be observed for Cr x=0.85, which reached the equilibrium CO production in 8 min. It also achieved a peak rate of 0.93 mL/min/g compared to 0.33 mL/min/g of LSM without the Cr B-site doping.

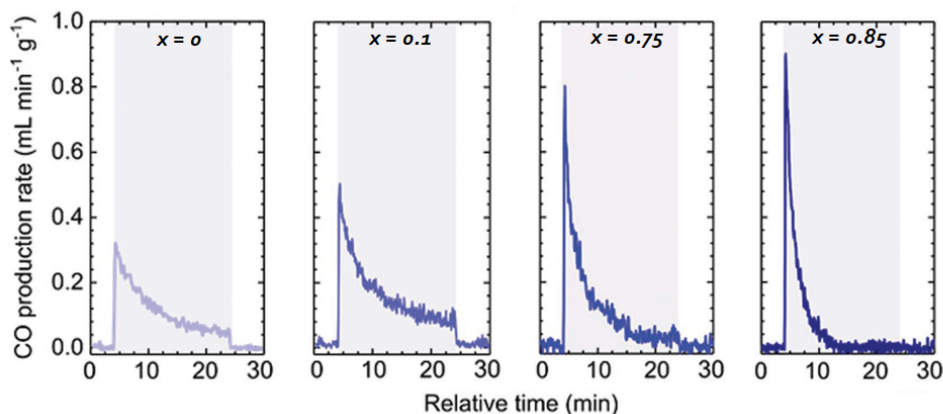


Figure 2.13: CO production rates of  $La_{0.6}Sr_{0.4}Cr_{1-x}Mn_xO_3$  materials obtained for the CO<sub>2</sub>-splitting half-cycle performed at 1200°C. [76].

The most favorable rate performance was observed for  $La_{0.6}Sr_{0.4}Cr_{0.85}Mn_{0.15}O_3$ , which showed fast splitting reaction and 0.8 mL/min/g when operated at isothermal conditions at 1400°C. This material also showed high thermochemical and structural stability and durability. In table 2.2 the CO yields of LSM Al and Cr-doped perovskites producing solar-to-fuel thermochemical cycles are summarized.

LM Perovskite	Experimental Conditions	$n_{CO}$ $\mu\text{mol/g/cycle}$	Ref
$\text{La}_{0.6}\text{Sr}_{0.4}\text{Mn}_{0.6}\text{Al}_{0.4}\text{O}_3$	Red in He at 1350°C/ Oxy in 40% $\text{CO}_2$ at 1000°C	294	[74]
$\text{La}_{0.4}\text{Sr}_{0.6}\text{Mn}_{0.6}\text{Al}_{0.4}\text{O}_3$	Red in He at 1350°C/ Oxy in 40% $\text{CO}_2$ at 1000°C	286	[74]
$\text{La}_{0.6}\text{Sr}_{0.4}\text{Mn}_{0.4}\text{Al}_{0.6}\text{O}_3$	Red in He at 1350°C/ Oxy in 40% $\text{CO}_2$ at 1000°C	247	[74]
$\text{La}_{0.5}\text{Sr}_{0.5}\text{Mn}_{0.75}\text{Al}_{0.25}\text{O}_3$	Red in Ar at 1400°C/ Oxy in 50% $\text{CO}_2$ at 1050°C	186*	[69]
$\text{La}_{0.6}\text{Sr}_{0.4}\text{Mn}_{0.6}\text{Al}_{0.4}\text{O}_3$	Red in Ar at 1400°C/ Oxy in 50% $\text{CO}_2$ at 1050°C	187*	[69]
$\text{La}_{0.6}\text{Sr}_{0.4}\text{Mn}_{0.4}\text{Al}_{0.6}\text{O}_3$	Red in Ar at 1400°C/ Oxy in 50% $\text{CO}_2$ at 1050°C	180*	[69]
$\text{La}_{0.5}\text{Sr}_{0.5}\text{Mn}_{0.6}\text{Al}_{0.4}\text{O}_3$	Isothermal redox cycling at 1400°C	212*	[79]
$\text{La}_{0.5}\text{Sr}_{0.5}\text{Mn}_{0.6}\text{Al}_{0.4}\text{O}_3$	Isothermal redox cycling at 1400°C	203*	[79]
$\text{La}_{0.5}\text{Sr}_{0.5}\text{Mn}_{0.6}\text{Al}_{0.4}\text{O}_3$	Red in Ar at 1400°C/ Oxi in 50% $\text{CO}_2$ at 1050°C	200*	[80]
$\text{La}_{0.5}\text{Sr}_{0.5}\text{Cr}_{0.4}\text{Mn}_{0.6}\text{O}_3$	Red in Ar at 1400°C/ Oxi in 50% $\text{CO}_2$ at 1050°C	138*	[80]
$\text{La}_{0.5}\text{Sr}_{0.5}\text{Cr}_{0.4}\text{Mn}_{0.6}\text{O}_3$	Isothermal redox cycling at 1400°C	139*	[79]
$\text{La}_{0.6}\text{Sr}_{0.4}\text{Cr}_{0.3}\text{Mn}_{0.7}\text{O}_3$	Red in Ar at 1400°C/ Oxi in $\text{CO}_2$ at 1200°C	205	[76]
$\text{La}_{0.6}\text{Sr}_{0.4}\text{Cr}_{0.1}\text{Mn}_{0.9}\text{O}_3$	Red in Ar at 1400°C/ Oxi in $\text{CO}_2$ at 1400°C	147	[76]
$\text{La}_{0.6}\text{Sr}_{0.4}\text{Cr}_{0.25}\text{Mn}_{0.75}\text{O}_3$	Red in Ar at 1400°C/ Oxi in $\text{CO}_2$ at 1400°C	129	[76]

Table 2.2: Summary of the fuel yields of LSM Al and Cr-doped perovskites in solar-to-fuel thermochemical cycles found in literature. Yields indicated with \* were obtained by means of TGA.

As previously said, the key issue of the thermochemical CO<sub>2</sub> splitting performance is the oxygen-carrier material, that must reflect the needs and restrictions imposed by the operating conditions of the system. The literature review presented in these previous paragraphs highlighted possible alternatives present to date. In particular, focusing on perovskites, these kind of oxygen carriers are getting increased attention. New compositions are synthesized and tested in this energy field to be compared with existing one in terms of fuel production, oxygen exchange capability, stability and durability. The material tested in this study is a non-stoichiometric double perovskite with composition  $Sr_2FeNi_{0.4}Mo_{0.6}O_{6-\delta}$ . In the next chapter a detailed description of the characterization of this material is provided. The focus then proceeds to results of tests performed on the material in a microreactor setup.

## Chapter 3

# Materials and Experimental Methods

### 3.1 Materials: SFNM-04

The choice of the material tested in this study was driven by the collaboration with the UNIUD and MIT [81]. The objective of the activity of research of UNIUD during the first year of the project was the individuation of perovskite oxides with suitable catalytic and electro-catalytic properties, in order to be used as anodic materials, or pre-anode catalytic layers. The first approach concerns the study of a double perovskite oxide of strontium, iron and molybdenum with a high content of nickel as dopant. The selected composition  $Sr_2FeNi_{0.4}Mo_{0.6}O_{6-\delta}$ , called also SFNM-04, is a double perovskite and it was chosen on the basis of previous studies which employed similar configuration as electrode in symmetrical and reversible SOFCs [82, 83]. Furthermore this material could evolve during reducing treatment in  $H_2$  at high temperature and form finely dispersed alloy nanoparticles on the perovskite surface via exsolution process. The latter mainly consists in a reversible transformation of the perovskite cubic structure in a layered Ruddlesden-Popper (RP) structure. These phases are named after S. N. Ruddlesden and P. Popper, who first synthesized and described the RP phase with general formula of  $A_{n+1}B_nO_{3n+1}$  in 1957 [84]. The crystal structure of RP perovskites is shown in Figure 3.1 and consists of  $nABO_3$  perovskite layers which are sandwiched between two AO rock-salt layers alternately distributed along the c-axis.

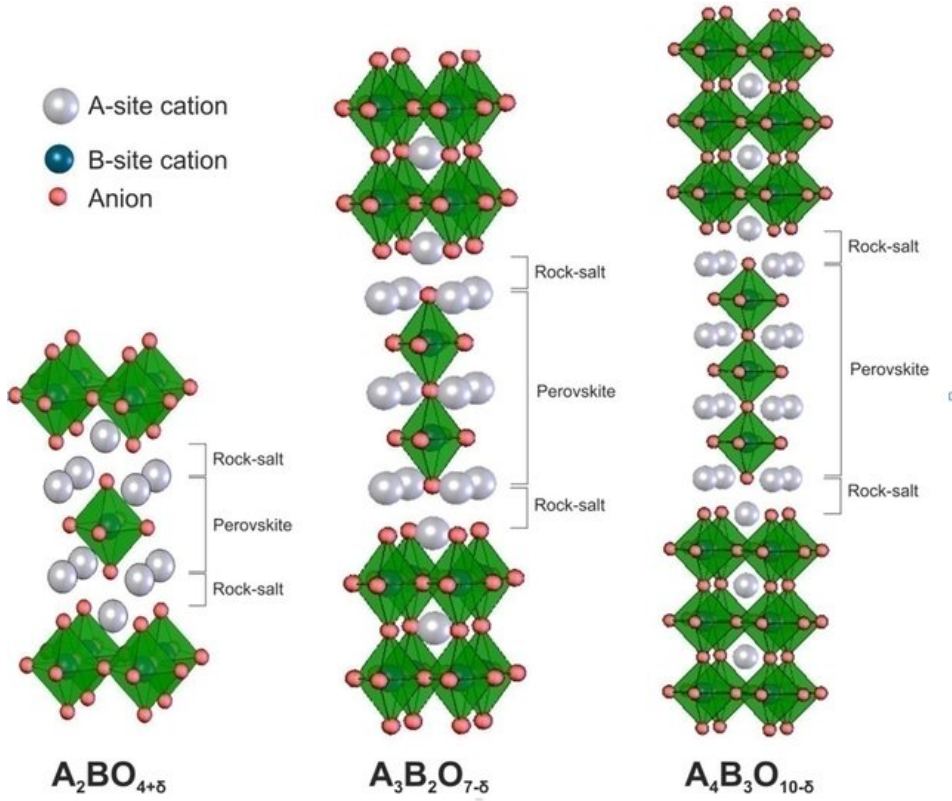


Figure 3.1: The structure of Ruddlesden-Popper phases ( $A_{n+1}B_nO_{3n+1}$  where  $n = 1, 2,$  and  $3$ ) [86].

Compared with other perovskites and oxygen ion conductors, the layered structural nature of RP perovskites allows several of them to accommodate a substantial amount of interstitial oxygen. This is mainly due to the presence of rock salt layers (AO) in the RP structure, which can accommodate excess oxygen [85]. The specific structure of SFNM-04 presents a double perovskite structure with the Fe and Mo cations that can arrange in alternative way inside the oxygen octahedra. In this context, Ni is expected to enter in the structure as  $Ni^{2+}$  and substitute some of the  $Fe^{2+}$  cations, increasing in this way the amount of  $Fe^{3+}$  with respect to  $Fe^{2+}$ . This leads to an increment in electronic conduction.

The characterization of the material was carried out in cooperation with the Department of Chemical Sciences of the University of Padua. Here follows a summary of the main analysis performed by the IMPACT research group.

### 3.1.1 Chemical-Physical Characterization

The perovskites phases were initially characterized with XRD, which is one of the most powerful non-destructive techniques when it comes to crystalline materials characterization. In figure 3.2 the obtained spectrum of both SFNM-04 and SFNM-05 (that has Ni concentration  $x=0.5$  instead of 0.4) composition is shown.

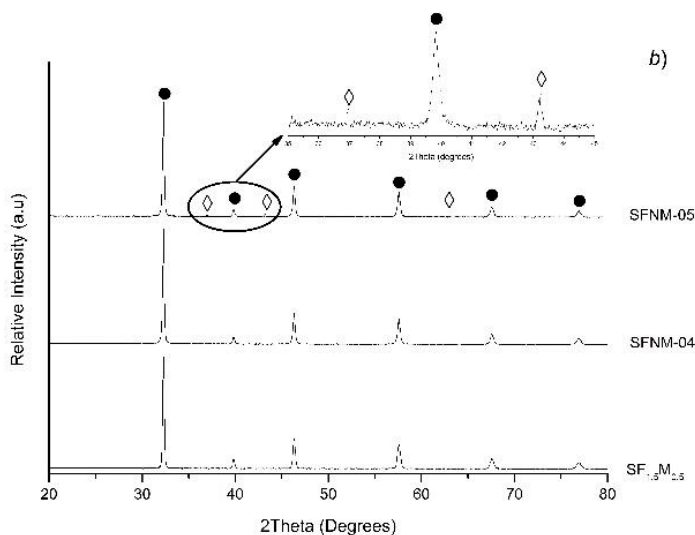


Figure 3.2: XRD spectra of SFNM-04 and SFNM-05 samples.

The XRD analysis demonstrated that the solubility limit of Ni inside the double perovskite lattice is between 0.4 and 0.5 molar compared to the other metallic cations. Indeed, the SFNM-05 sample presented a NiO segregation on the surface, which demonstrates that not all of the Ni was entered in the structure, while SFNM-04 shows no segregation and phase separation. Semi-quantitative XPS and EDX analysis of SFNM-04 and SFNM-05 provided further confirmation of the solubility limit; the results of these analysis showed a small surface segregation of Sr in SFNM-04 and a high amount of Ni on the surface of SFNM-05, due again to the exceeding of the solubility limit in the structure.

### 3.1.2 Functional Characterization

In order to investigate the material evolution and stability to repeated redox cycles, a further characterization on SFNM-04 has been done with the Temperature

Programmed Reduction (TPR). The analysis approach used is the following:

1. Pre-treatment in air raising 10 °C/min up to 500°C to remove impurities and/or to re-oxidize the sample after every reduction ramp;
2. 1 hour of dwelling at 500°C;
3. TPR raising 10 °C/min up to 900°C in a reducing ambient at  $H_2/N_2 = 4.5\%$ , with a flux of 35 ml/min;
4. Cooling ramp down to room temperature in  $N_2$ ;
5. Re-oxidation step, as described in the first point.

The raw signal of the  $H_2$  consumed in each reduction step during TPR analysis is shown in Figure 3.3.

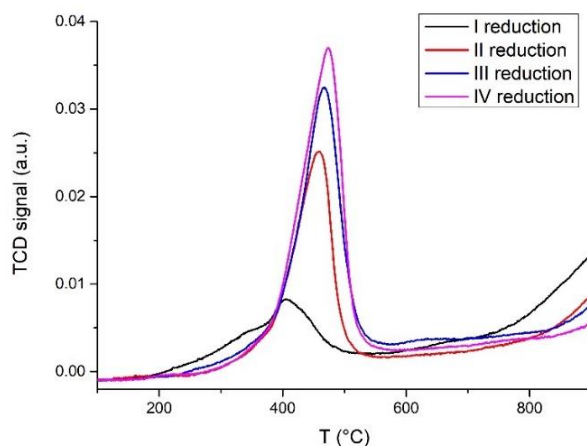


Figure 3.3: SFNM-04  $H_2$  consumption in TPR analysis of 4 subsequent reduction and re-oxidation cycles.

As it is clearly visible from the image, the trend of the curve drastically changed between the first reduction and the second one, while the profile seems to be more stable and constant after the second reduction. The explanation of this evolution is within a transition phase during the first reduction cycle, from the starting double perovskite structure to a different phase more stable to reduction. A second XRD analysis has been performed after TPR to confirm this hypothesis.

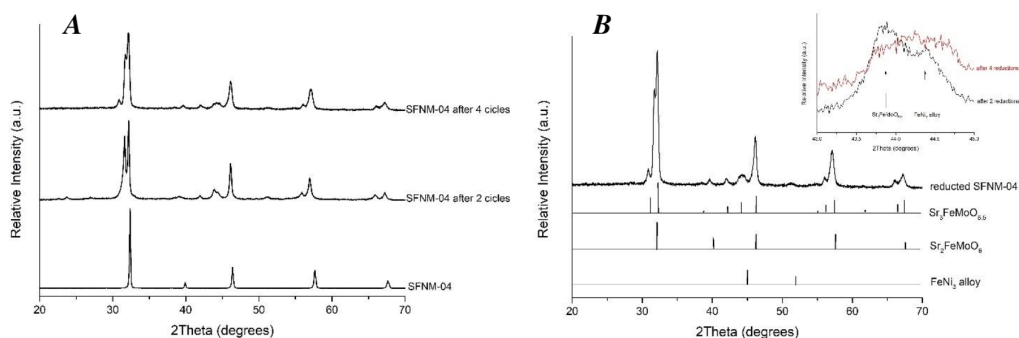


Figure 3.4: Functional Characterization of SFNM-04: a) XRD spectra after 2 and 4 reduction cycles; b) Magnification of the signal at  $44.5^\circ$ .

In Figure 3.4 the spectra of SFNM-04 after 2 and 4 reduction cycles is shown to understand the evolution of the phase in a reductive environment; after the second TPR cycle, both the structure transition, with the formation of a RP phase, and the formation of a surface alloy  $FeNi_3$  from the already mentioned exsolution process can be identified. The most intense signal attributed to the Fe-Ni alloy is in correspondence of  $44.5^\circ$  and it is better shown in the magnification in Figure 3.4 b); its area grows together with the number of cycles meaning that that the exsolution process proceeded during the cycles. This could explain the peak of  $H_2$  consumption at  $450^\circ C$  shown in figure 3.3, that should account to the contribution of alloy reduction and the successive reduction of  $Fe^{3+}$  and  $Mo^{6+}$  in the RP structure.

### 3.1.3 Stability of SFNM-04 to $CO_2$

After the TPR assessment, also the stability of the material to  $CO_2$  has been tested. Experimental results on the samples suggested that the presence of Ni inside the SFM lattice is responsible for the formation of carbonates and molybdates and destabilizes the SFM double perovskite phase, compromising the long-term performance of devices that will employ hydrocarbons as fuels. It must be noted that  $SrMoO_4$  compound has been found in SFNM-04 after one year from its first synthesizing due to the reaction with the atmospheric  $CO_2$  at room temperature. Moreover, as shown in 3.5, the formation of  $SrMoO_4$  and  $SrCO_3$  was observed with an XRD analysis on a powder sample of SFNM-04 treated in 30% of propane in

$N_2$  at  $800^\circ C$  for 2 hours, to simulate the operating conditions.

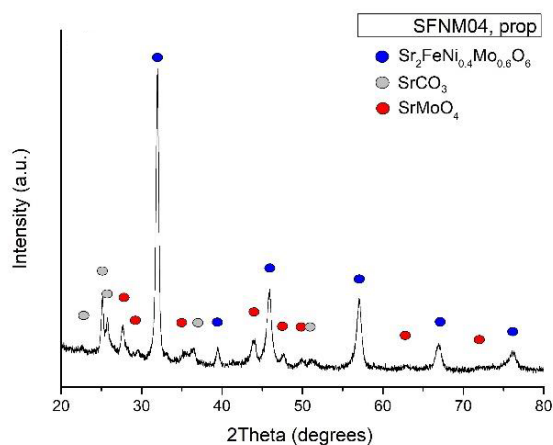


Figure 3.5: XRD analysis of SFNM-04 after the treatment in 30%  $C_3H_8$  at  $800^\circ C$  for two hours.

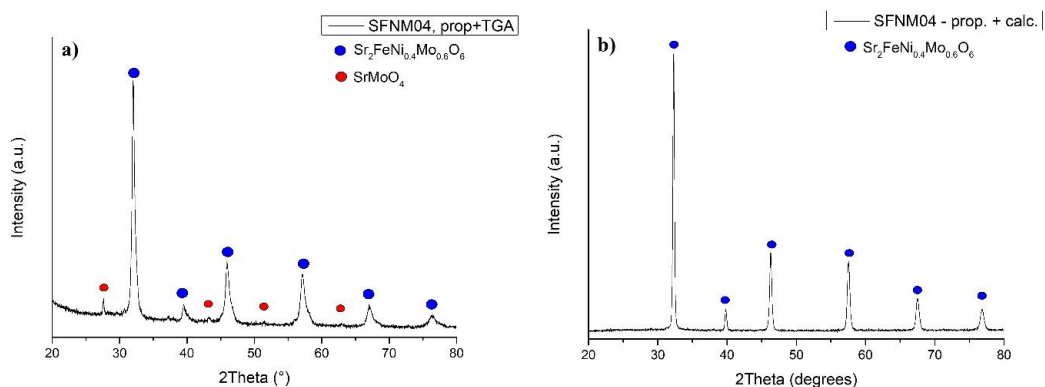


Figure 3.6: XRD analysis of SFNM-04 after a) thermal treatments; b) after the calcination in 30%  $C_3H_8$  at  $800^\circ C$  for two hours.

In order to restore the starting phase of the material, a thermal treatment at slightly higher temperature than the operating one would be enough. As shown in Figure 3.6 a), the XRD analysis after the TGA sample has revealed that  $SrCO_3$  disappeared with the thermal treatments; also, phase  $SrMoO_4$  appeared to be largely decreased in the double perovskite structure. A further calcination at  $900^\circ C$  in air restored the starting double perovskite phases, by eliminating all of

$SrMoO_4$  from the sample. The XRD analysis of the restored material after TGA and calcination treatments is shown in Figure 3.6 b).

### 3.1.4 Oxy-dry Reforming Catalytic Tests

SFNM-04 material has finally been tested as catalyst for both dry reforming and oxy-dry reforming reactions, but the best results were obtained in oxy-dry reforming conditions. The test was performed in 80 ml/min flux of  $CH_4:CO_2=3:2$ . The sample was pre-reduced at  $800^\circ C$  in  $H_2$  for one hour and then kept in a reducing environment for 12 hours at  $700^\circ C$ . Table 3.1 summarizes the  $H_2$  and CO production data.

T°C	561	610	659	708	758	808
CO	0	0,043	0,048	0,329	2,293	4,539
$H_2$	0	0	0,172	0,118	0,586	2,806

Table 3.1: CO e  $H_2$  production by SFNM04 powders.

The oxy-dry reforming reaction started at  $700^\circ C$ , with appreciable results at  $800^\circ C$ . Moreover, a clear inflection of  $CO_2$  conversion is shown between  $550^\circ C$  and  $600^\circ C$ , followed by an increment of  $CH_4$  conversion, meaning that a direct combustion between methane and oxygen is happening.

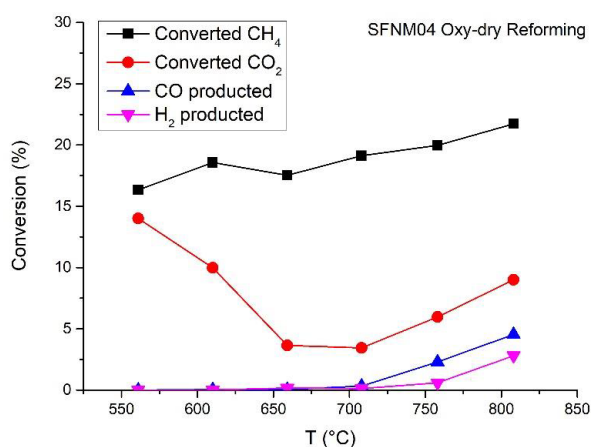


Figure 3.7: Catalytic results of Oxy-dry Reforming Test for SFNM-04.

### 3.1.5 Influence of H<sub>2</sub>, CO<sub>2</sub> and temperature

Recently the SFNM-04 has been used as oxygen carrier material in redox cycles performed in microreactor setup at Politecnico di Torino. More details about the setup are provided in 3.2. By varying the content of CO<sub>2</sub> in the oxidation and of H<sub>2</sub> in reduction, the influence of these parameters on the CO production has been suggested. The results of an isothermal test performed at T=850°C varying CO<sub>2</sub> content and H<sub>2</sub> content are shown in figure 3.8 and 3.9 respectively. The tests aim is to analyze the SFNM-04 response in terms of CO production by changing the H<sub>2</sub> content in a range of 5÷100 % and the CO<sub>2</sub> content in a range of 6÷100 %, without considering the temperature effect in first approximation.

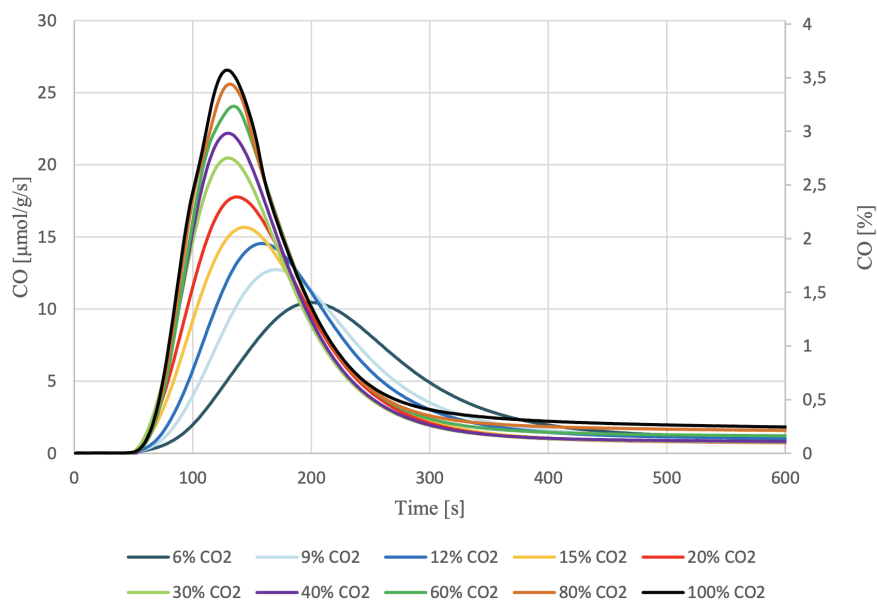


Figure 3.8: CO production expressed in [ $\mu\text{mol/g/s}$ ] and in [%] terms: 9 Isothermal Cycles at T=850°C by varying the CO<sub>2</sub> content in the range 6-100 % during reduction.

The outcomes of the tests show that by increasing the CO<sub>2</sub> concentration during the oxidation step in a N<sub>2</sub>-based gas mixture from 6% to 100%, the CO peak goes from 10.11 [ $\mu\text{mol/g/s}$ ] to about 26.08 [ $\mu\text{mol/g/s}$ ]. Moreover, as shown in Figure 3.8, the the amount of CO<sub>2</sub> in the gas mixture affects the kinetic of the reaction: it take about 120 s to reach the CO production rate peak with 100% of CO<sub>2</sub>, that is much less than the time required with 6% of CO<sub>2</sub>. Differently, by increasing the

H<sub>2</sub> content in the reduction flow rate starting from 5% up to 100%, the CO peak increase from 16.55 [ $\mu\text{mol/g/s}$ ] up to 36.01 [ $\mu\text{mol/g/s}$ ].

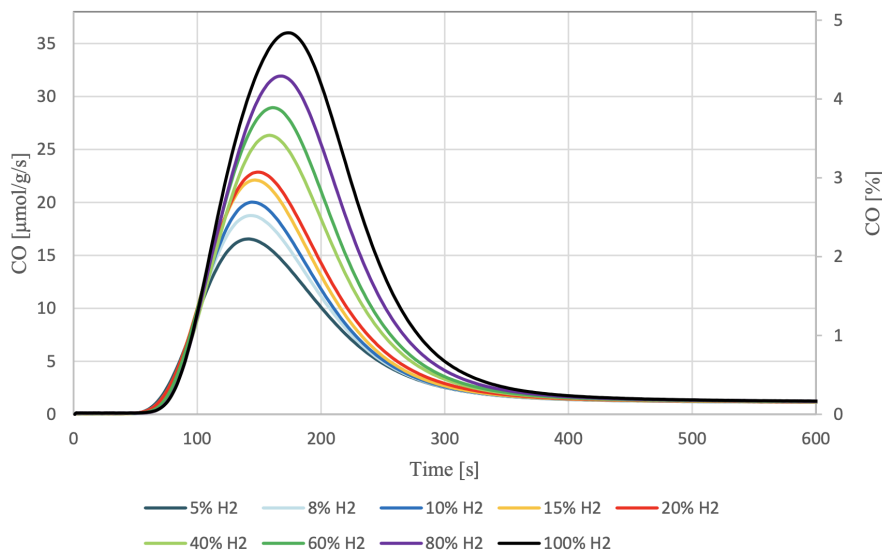


Figure 3.9: CO production expressed in [ $\mu\text{mol/g/s}$ ] and in [%] terms: 10 Isothermal Cycles at  $T=850^{\circ}\text{C}$  by varying the H<sub>2</sub> content in the range 5-100 % during reduction.

The influence of the H<sub>2</sub> content seems to be predominant with respect to the CO<sub>2</sub> ones, allowing to reach higher CO production rates. These results can be explained by the fact that the H<sub>2</sub> indirectly affect the re-oxidation of the sample. Indeed, higher H<sub>2</sub> concentrations promote a favorable reduction of the sample that means a higher amount of released oxygen, and thus a higher amount of oxygen vacancies generated within the structure. At the same time, also the exsolution process is slightly enhanced when the sample reacts in a stronger reducing environment. The main difference with respect to the outcomes obtained varying the CO<sub>2</sub> content seems to be the influence on the reduction kinetics, corresponding to a faster reaction with the increase of CO<sub>2</sub> content. On the contrary, increasing/decreasing the H<sub>2</sub> content seems not to affect the kinetic of the reaction. This difference is due to the fact that the CO<sub>2</sub> content directly affects the CO production rate in the oxidation step, while the H<sub>2</sub> has an indirect effect the CO production, creating a lattice structure with less oxygen vacancies and less suitable to produce fuels during a re-oxidation step.

The same tests have been performed by fixing the isothermal temperature at lower value equal to  $T=750^{\circ}\text{C}$ . With a lower operating temperature, a diminution of the reaction kinetics is expected together with a smaller CO production rate and global yield. Concerning the influence of  $\text{CO}_2$  [%] also in this test, as the content increases, a CO production rate increase is detected. In this case it is not noted the shrinkage of the curves highlighted for tests performed at higher temperature while increasing  $\text{CO}_2$  [%], revealing a slower reaction kinetics. Moreover, the maximum CO production values and the global yields obtained operating at  $T=750^{\circ}\text{C}$  with  $\text{CO}_2$  content equal to 100% are slightly lower when compared to the outcomes of the test at higher temperature with 20% of  $\text{CO}_2$ . With reference to  $\text{H}_2$  [%] influence, values obtained with higher operating temperature are increased with respect to those obtained at  $T=750^{\circ}\text{C}$ . As an example, when using a mixture of 5%  $\text{H}_2/\text{N}_2$  at  $T=850^{\circ}\text{C}$ , the maximum CO production rate reached is higher of that observed when performing an isothermal cycle at  $T=750^{\circ}\text{C}$  with a reducing gas composed only by hydrogen (100%  $\text{H}_2$ ). In fact, at  $T=750^{\circ}\text{C}$  with 100%  $\text{H}_2$  a maximum CO production rate of around 14 [ $\mu\text{mol/g/s}$ ] is reached, that is lower than the one obtained at  $T=850^{\circ}\text{C}$  with 5% of  $\text{H}_2$ , 16.549 [ $\mu\text{mol/g/s}$ ]. Also in terms of global yields [ $\mu\text{mol/g}$ ], the maximum value obtained while operating at lower temperature is in correspondence of  $\text{H}_2$  content equal to 100%. This value is again comparable with the value of CO production obtained performing an isothermal cycle at  $T=850^{\circ}\text{C}$  with only 10% of  $\text{H}_2/\text{N}_2$  as reducing gas and 20%  $\text{CO}_2/\text{N}_2$  for the oxidation step.

Temperature [ $^{\circ}\text{C}$ ]	$\text{CO}_2$ [%]	$\text{H}_2$ [%]	CO production rate [ $\mu\text{mol/g/s}$ ]	CO yield [ $\mu\text{mol/g}$ ]
750	20	100	14	2190.4
850	20	5	16.5	2068
750	100	10	17	2269.6
850	20	10	17.5	2183.3

Table 3.2: Results of the isothermal tests performed at  $T=750^{\circ}\text{C}$  and  $T=850^{\circ}\text{C}$  varying  $\text{CO}_2$  and  $\text{H}_2$  content.

These results highlight that the operating temperature is the main impacting parameter for this kind of process. The outcomes summarized in this paragraph

and reported in table 3.2 show, in fact, that even if a 100% CO<sub>2</sub> flow is used during oxidation step (or 100% H<sub>2</sub> in the reduction one), a comparable redox performance would be achievable by increasing the temperature up to T=850°C with only 20% of CO<sub>2</sub> content (or 10% H<sub>2</sub>).

### 3.1.6 Exsolution

From the tests described in the previous paragraph, it is evident that the variation of reduction parameters has a predominant effect in terms of CO production rate compared to the oxidation variation. This is probably due to the already mentioned exsolution phenomenon, here described more in details.

The exsolution phenomenon is for sure one of the most interesting features of the SFNM-04 which has already been studied by Du et al. [87] in a research paper regarding the electrochemical characteristics of Sr<sub>2</sub>FeMo<sub>1-x</sub>Ni<sub>x</sub>O<sub>6-δ</sub> perovskite (with x=0.25 and 0.35).

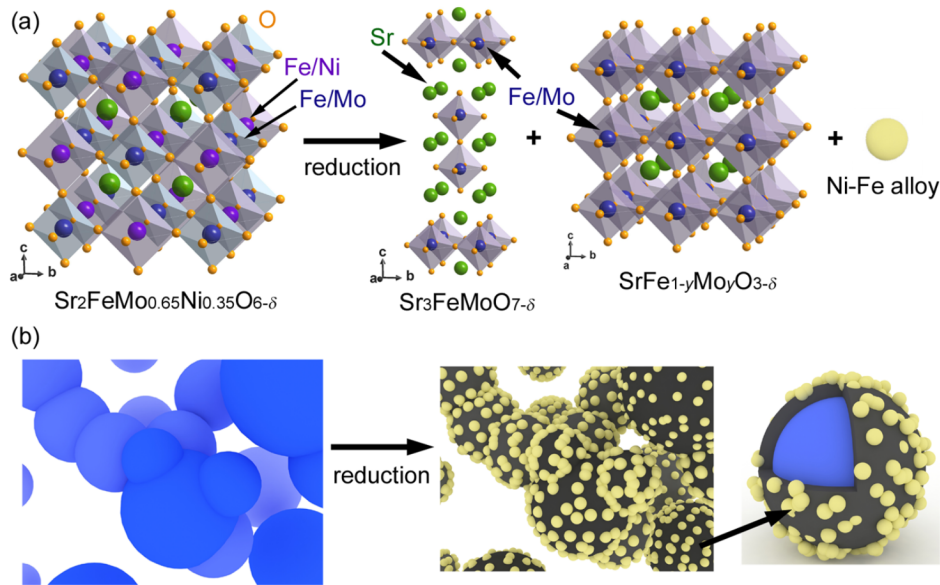


Figure 3.10: Illustration models for (a) structure transformation and (b) surface morphology evolution of Sr<sub>2</sub>FeMo<sub>0.65</sub>Ni<sub>0.35</sub>O<sub>6-δ</sub> under reducing atmosphere [87].

They observed the presence of exsolved FeNi<sub>3</sub> alloy nanoparticles on the surface of the perovskite structure. This phenomenon is due to the partial substitution of Mo with Ni in the structure. More in details, Fe and Ni tend to exsolve from the

lattice in reducing condition, corresponding to a self-assembly of FeNi<sub>3</sub> alloy on the surface in form of nanoparticles. The crystal structure transformation and the surface morphology evolution of the material under the reducing atmosphere is shown in Figure 3.10. Clearly, most of the nickel remains within the lattice with Ni<sup>2+</sup> valence and only a small fraction is reduced to metal from the substrate. As it can be seen from Figure 3.10 (b), the decomposed phases form a protection layer on the particles, which may impede further reduction allowing the inside of the particle to maintain the original perovskite structure. This phenomenon represents the driver of two different effects; firstly, the exsolution of Fe<sup>2+</sup> and Ni<sup>3+</sup> ions is responsible for the generation of a huge number of vacancies inside the perovskite lattice; secondly, the alloy generated on the surface acts as catalyst of the oxidation reaction, promoting the CO<sub>2</sub> dissociation. Therefore, this mechanism not only results in an enhancement of the global electro-catalytic performance of the material, but also in an increase of the stability of SFNM-04 due to the higher resistance of the alloy, with respect to metallic Ni, to sulfide and coke poisoning. As already mentioned in paragraph 3.1.3, the presence of Ni inside the SFM lattice is responsible for the formation of undesirable carbonates and molybdates, compromising the long-term performance of the materials. High concentrations of this carbonates could cause the carbon deposition phenomenon, limiting both the charge transfer and the diffusion of the oxygen towards the cathode surface. As a consequence, the re-oxidation of the SFNM-04 sample is negatively affected.

## 3.2 Test Bench Description

In this chapter a description of the experimental setup used to investigate the redox performance of SFNM-04 in CL application is provided. The analysis has been carried out in the CO<sub>2</sub> Circle Lab, located inside the Environmental Park of Turin, Italy. The test bench is used to test samples of different materials, in the form of powders or pellets. The experimental procedure is carried out in a controlled atmosphere by using a microreactor, which may be heated up to 1700°C. The use of the microreactor has several advantages: the very small thermal inertia, allowing for an almost immediate control of temperature; the inherent safety due to both the small reactant volume and the well controllable reaction conditions; the possibility to have very large surface to volume ratios. Moreover, by using a

microreactor, the actual production of the useful species can be measured. That's not possible if a thermal gravimetric analysis is employed for the characterization of the material. As a matter of fact, TGA measures the mass variations of the samples over time as the temperature changes. But the mass variations may be due not only to redox reactions. It may also be caused by any other reaction that occurs (e.g., formation of unwanted oxides, carbon deposition). It should be noted, however, that despite its advantages, the microreactor setup should not be considered as a replacement for TGA analysis. Both of these methods are necessary for the materials characterization. The test bench setup is shown in Figure 3.11.

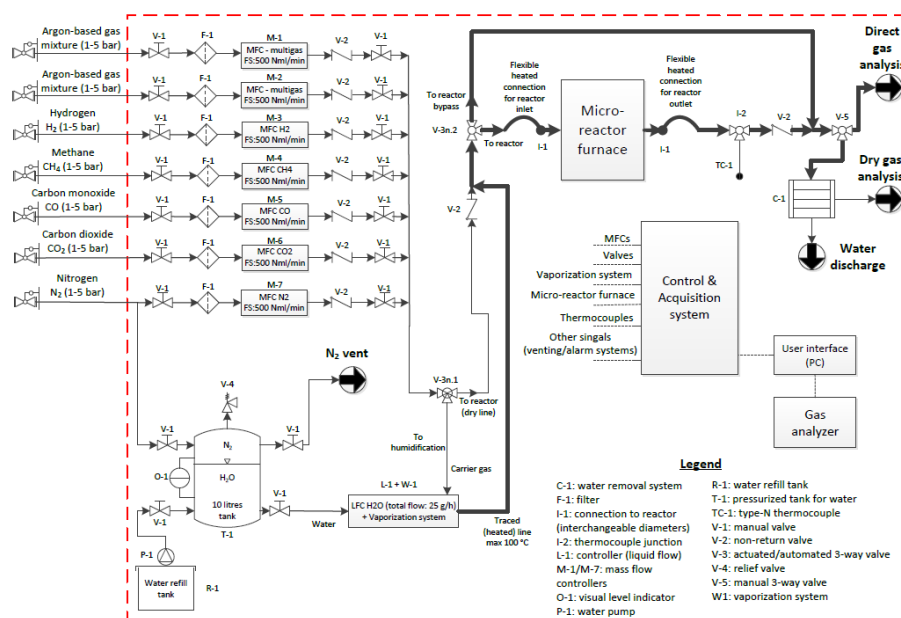


Figure 3.11: Test bench setup

More in details, the test bench is equipped with a gas supply system consisting of seven gas lines, five of which directly connected to the gas lines of the laboratory by means of pressure reducers installed on the wall. The remaining two are connected to cylinders placed under the hood, equipped with pressure reducers directly installed on them and activated only in operating conditions. The five gases directly connected to the gas lines are  $N_2$ ,  $CH_4$ ,  $CO$ ,  $CO_2$ ,  $H_2$ ; while the gases contained in the cylinders are mixtures such as:  $Ar-H_2$  (5% max),  $Ar-CH_4$

(5% max), Ar-CO<sub>2</sub> (5% max), Ar-CO (5% max), Ar-O<sub>2</sub> (5% max). All the streams start with a pressure of 2.5 bar, with the only exception of the N<sub>2</sub> stream, that start with higher pressure (in the range 3.5-5 bar), allowing the latter to pressurize also a demineralized water tank used to obtain, if necessary, a humidified stream. In the section downstream the pressure reducers, mass flow controllers are installed to regulate and measure the flow by means of a manual shut-off valve and a filter (in Figure 3.11 indicated as *V-1* and *F-1* respectively) installed upstream, and a non-return valve and a manual shut-off valve (in Figure 3.11 indicated as *V-2* and *V-1* respectively) installed downstream the MFC.

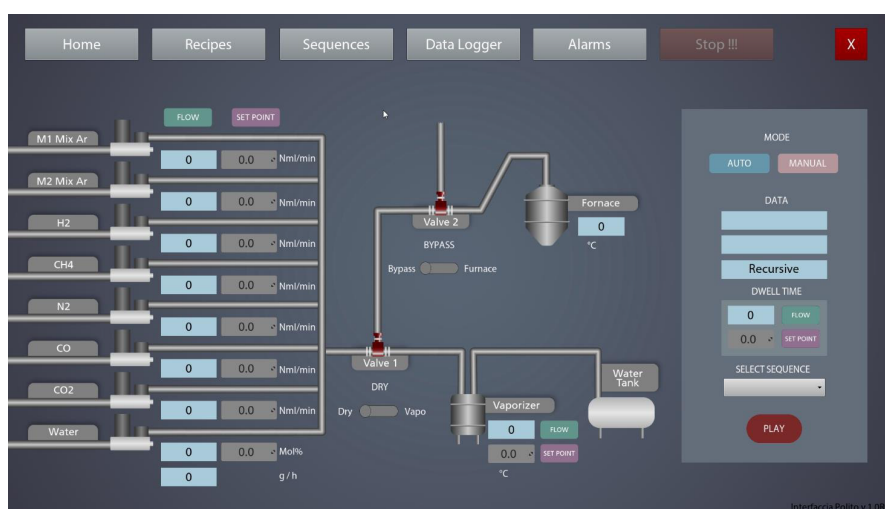


Figure 3.12: Software home screen

After MFCs, the seven lines converge into one dry mix line at atmospheric pressure towards two three-way valves (*V-3n.1*, *V-3n.2*). The first one is equipped with pneumatic actuator to select if the stream has to be dry or wet; the second one has been added to choose between directing the stream into the furnace or by-passing it to vent. Gas and water mass-flow controllers, vaporizer and pneumatic valves are controlled remotely via API-Miot software [88], which can be considered for all intents a SCADA (Supervisory Control And Data Acquisition); the software allows in fact to supervise, control and acquire data from the process. The home screen of API-Miot is shown in Figure 3.12. The furnace is controlled by an autonomous regulator that allows to configure set-points and ramps of temperatures and cycles. The software of the test bench and of the furnace enable to carry out

series of test cycles completely controllable from remote. The microreactor and the by-pass lines convey in a single line at the outlet of the microreactor. A manual selection valve allows to choose whether to direct the mixture to a condenser or to a gas analyser. The analyser output is then connected to a flexible exhaust line in the hood.

### 3.2.1 Microreactor and Furnace Section

The microreactor employed in the test bench is positioned inside the tubular electric furnace Carbolite Gero, as shown in Figure 3.13. A PCU is also used as energy supplier to provide electricity to the resistances placed in the core of the oven but also as controlling system for what concerns the temperature programs. The electric furnace is controlled by an Eurotherm PID which allow to remotely impose isothermal steps of temperature in a given time interval, or create ramp-up or ramp-down steps by selecting the proper set-point temperatures and the rate of progression in K/min.



Figure 3.13: Carbolite Gero furnace

More specifically, the Carbolite Gero microreactor is a continuous flow reactor composed by a 1-meter length horizontal tube of alumina ( $\text{Al}_2\text{O}_3$ ) with internal diameter of 32 mm [89]. Several insulation layers are placed between the inner tube and the outer layer to limit the heat and flow leakages and to provide a thermal barrier avoiding heat dispersion. Initially, the tests has been conducted with the *crucible configuration* in which a specific type of sample holder has been

chosen. The SFNM-04 powders have been placed in a bigger crucible with the shape like a half of cylinder, made of the same material as the tube (alumina). The perovskite powder mass has been measured by means of an analytical balance and then pushed to the center of the furnace.

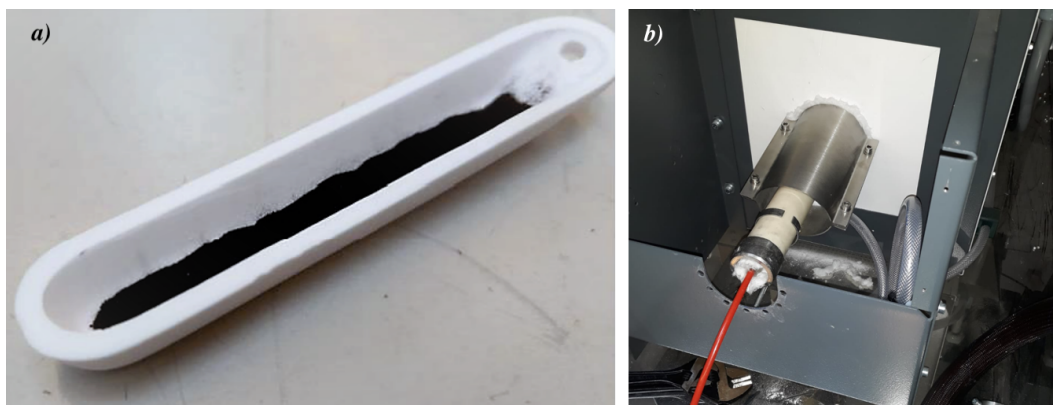


Figure 3.14: Microreactor setup: a) Alumina Crucible; b) tube-in tube.

In a second phase of the study an alternative setup, here referred as *tube-in-tube configuration*, has been selected. The reactor area has been reduced by inserting in the external tube a secondary alumina tube with a 8 mm of internal diameter. In the latter the sample has been placed in the center and, to ensure the position of the material, a quartz wool has been added before and after the sample mass. The crucible and the tube-in-tube configuration are shown in Figure 3.14.

### 3.2.2 Gas Analyser

The line containing the gas exiting from the reactor is analysed by the gas analyser. As it only works with dry mixture of gas, all the moisture content into the mixture has to be removed by the condenser placed after the furnace, allowing the instrument to work correctly without getting damaged. The basic operation of this component is to compare the physical properties of the entering stream with the properties of a reference gas, making it possible to evaluate the molar fraction of each molecule present in the analysed stream. The analyser used in this study is the Emerson Rosemount X-Stream XE. It is a continuous gas analyser that allows to measure up to five chemical species by means of two different detectors: Thermal Conductivity Detector (TCD) and Infrared Detector (IRD).

## Thermal Conductivity Detectors

The TCD is a universal, non-destructive, concentration-sensitive detector commonly used in gas chromatography. It basically senses changes in the thermal conductivity of the sample gas and compares it to a reference flow of carrier gas. Schematically a TCD can be represented as the image in 3.15.

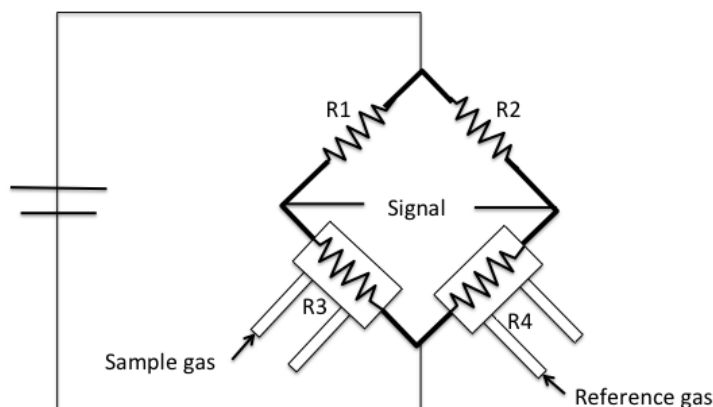


Figure 3.15: A simplified circuit diagram of a Thermal Conductivity Detector [90]

In a typical TCD, the sample components in the carrier gas and the reference gas flow into separate channels. A power supply provides current to the electrically heated resistance wires located in both channels. Due to the difference in thermal conductivity, when carrier gas containing sample vapors enters the measuring cavity, it will absorb a different amount of heat with respect to the reference gas, resulting in a change of the sensor temperature. This change in temperatures will lead to a change of the resistances from both the reference gas and the sample gas, which results in an out-of-balance signal proportional to the concentration of sample vapor in the sensor cavity. The carrier gas has therefore a dual function: it is both used to transfer the sample through the column, and as a reference gas. Due to these requirements it must be inert and may not be adsorbed by the column material but it also must be characterized by a different thermal conductivity with respect to most common sample gases in order to increase the detector sensitivity. Helium is often used as carrier gas since the large difference in thermal conductivity between He and other gases results in an enhancement of the sensitivity of TCD detection, generally producing a linear response [91]. The issue with helium as carrier gas arises only when in presence of helium-hydrogen mixtures.

As a result of their close thermal conductivity values, hydrogen gives a relatively low response on a TCD when using helium as carrier gas [92]. To address this issue Argon may be used in the place of helium. This solution results, however, in decreased sensitivity for the other compounds analyzed on the same channel, driving the need of a separate channel for the hydrogen analysis. For this case study, the Emerson X-Stream XE instrument is fitted with a TCD only for the H<sub>2</sub> flow stream.

### Infrared Detectors

An infrared detector is a detector that reacts to infrared radiation exploiting the selective absorption of chemical compounds in the infrared region of the spectrum. Since the atoms of each molecule are capable of vibrating only with definite frequencies, if a gaseous material is irradiated with infrared light of all wavelengths, those wavelengths which correspond to the vibrational frequencies of its molecules are absorbed while all the others are transmitted. As the gas molecules absorb this radiation, the molecules gain energy and vibrate more vigorously, resulting in a rise in the temperature. The temperature increases in proportion to gas concentration, and is detected by the detector. Moreover, the radiation absorbed by the gas molecules at the particular wavelength will correspond to a decrease in the original source strength. This radiation energy decrease can also be detected. The input measured is then converted into electrical signals. *Pyroelectric detector* is the most commonly used for gas measures; it exploits the pyroelectric materials features to exhibit spontaneous polarization, which is function of temperature. As infrared radiation strikes the detector surface, the change in temperature causes a current to flow, which is proportional to the intensity of the radiation. This detector exhibits good sensitivity and good response to a wide range of wavelength. The simplest way of converting light energy into an electrical signal is by means of a *thermoelectric detector*; this type of detector converts temperature into an electrical signal and is commonly known as a thermocouple. It is based on the junction of dissimilar metals, which generates a voltage potential directly proportional to the temperature.

IRDs can be divided in two subcategories, namely dispersive and non-dispersive. Dispersive types utilize an optical device such as a prism to reflect the infrared rays and the radiation is firstly focused on a slit and then converged by mirrors on

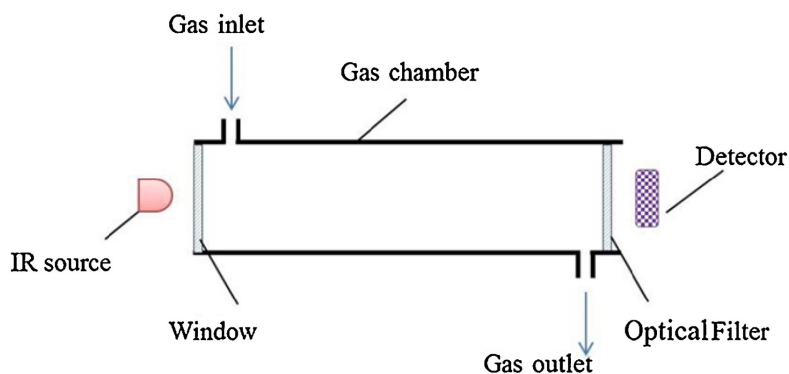


Figure 3.16: Typical structure of a NDIR [93]

a thermocouple. The dispersive type instrument is typically used only for special requirements. Almost all commercial IR instruments are of the non-dispersive type, in which two sources of IR are implemented. A sample cell allow the passage of the gas, and a second compensating cell is used to determine the background of radiation. The typical structure of a NDIR is shown in Figure 3.16. The major drawbacks of NDIR sensor are interference and detection limit; the use of a NDIR sensor for a certain gas is subject to interference from other gases that can absorb IR light [94]. Eliminating interference among target gases is very important and it has been corrected by applying multi-optical filters [95, 96]. Concerning the detection limit, Farren investigated the enhancement of IR source to increase NDIR analyzer output signals [97]. Park and Yi examined the implementation of concave mirror surfaces to focus a IR beam into the detector to increase the intensity of IR on the detector, with a corresponding enhancement of the detection limit [98].

### 3.3 Preliminary Experimental Procedures

Before starting the experimental tests, preparatory procedures are necessary to make the bench ready for operation. First and foremost, the reactor has to be at ambient temperature; so if other tests have been run, it is mandatory to wait for it to cool down. Moreover nitrogen is injected to clean the reactor. Subsequently the SFNM-04 sample is weighted and then inserted in the alumina tube, dispersed in the quartz wool or placed into the boat-shaped crucible depending on the selected configuration. In this step it is important that all gas lines are closed and similarly

the power conditioning unit must be switched off. Once the sample is loaded into the alumina tube, the flanges are closed and a leak test in Nitrogen is performed to verify the sealing of the reactor. The leakages are considered acceptable if lower than 10% of the mass flow injected. Then, the Emerson X-Stream analyser is connected to the outlet gas lines and the temperature program and the gas composition sequences are imposed through the software previously mentioned. Finally the last step consists in verifying if a calibration procedure of the gas analyser is needed. The zero and maximum range value are verified and eventually set by sending in the gas lines known gas flow concentrations. Once all these steps have been followed, both the reactor and the gas analyser are ready to be used.

# Chapter 4

## Results

The aim of the tests described in this section is to assess the influence of the SFNM-04 mass, gas flow rates and experimental configuration of the system on the fuel yields. To do so, a series of isothermal redox cycles at 850°C have been conducted in a microreactor setup varying the sample mass and the oxidation mass flow rates. The experimental tests are summarized in table 4.1, and extensively described in the following paragraphs.

Test ID	Configuration	Sample mass [mg]	Paragraph
Test (I)	Crucible	200	4.2
Test (II)	Crucible	50	4.3
Test (III)	Crucible	20.7	4.4
Test (IV)	Crucible	10	4.5
Test (V)	Crucible	5	4.6
Test (VI)	Tube-in-tube	4.6	4.7
Test (VII)	Tube-in-tube	1.3	4.8

Table 4.1: Brief summary of the set of experimental tests performed

As shown in Table 4.1, 7 tests have been performed. The first group of tests, (from Test (I) to Test (V)) has been carried out with the crucible configuration, progressively reducing the mass of the sample and varying consequently the oxidizing flow rates in the range 100-625 [Nml/min] in order to have similar mass to

flow ratios to be compared. The flow rate range has been chosen depending on instrumental and setup constraints; the lower bound is limited by the Emerson Gas Analyzer (EGA), whereas the maximum value of 625 Nml/min is imposed by the upper bound of the gas feeding lines. A second set of tests (Test (VI) and Test (VII)) has been performed varying the setup of the microreactor and, in particular, using the tube-in-tube configuration. The first test has been done with a mass of the sample similar to the lowest tested in the crucible in order to assess the influence of the setup on the outcomes of the tests. Although the mass of the sample, the mass flow rates and the setup vary, others parameters have been kept constant for all tests. These parameters are listed in 4.2.

<b>Reduction temperature</b>	850°C
<b>H<sub>2</sub> in reduction</b>	10%
<b>Reduction step duration</b>	30 [min]
<b>Reduction flow rate</b>	200 [Nml/min]
<b>Oxidation temperature</b>	850°C
<b>CO<sub>2</sub> in oxidation</b>	20%
<b>Oxidation step duration</b>	15 [min]%

Table 4.2: Parameters kept constant in all the tests performed.

More in details, each test is composed by 4 redox cycles for each oxidation flow rate values. As previously said, the cycles have been performed in isothermal condition at  $T=850^{\circ}\text{C}$ . The first 5 tests have been performed in a crucible configuration. When this setup has been used, before starting with the first redox cycle, a pre-treatment in air at  $T=500^{\circ}\text{C}$  for 60 min is carried out to ensure the absence of contaminants and to operate with a fully-oxidized sample. The temperature required for the pre-treatment has been reached maintaining a  $\text{N}_2$  flow rate  $m=200$  Nml/min. Subsequently, the temperature is increased by means of the temperature sequence controller from  $T=500^{\circ}\text{C}$  up to  $T=850^{\circ}\text{C}$  with a ramp rate of  $10^{\circ}\text{C}/\text{min}$ . Differently, in the last 2 tests, performed by using a tube-in-tube configuration, the isothermal redox temperature  $T=850^{\circ}\text{C}$  has been directly reached without the intermediate pre-treatment of the sample.

More in detail, a single redox cycle is organized in 5 subsequent steps:

- Reduction step with a gas mixture composed by 10% H<sub>2</sub>/N<sub>2</sub> for 30 min;
- Purge step in N<sub>2</sub> atmosphere for 10 min;
- Oxidation step in 20% CO<sub>2</sub>/N<sub>2</sub> atmosphere for 15 min;
- Oxidation step in air for 10 min;
- Purge step in N<sub>2</sub> atmosphere for 5 min to sweep the remained gases;

## 4.1 Data Processing

The experimental methods and practical procedure followed to extrapolate data are here described for the Test (I) used as reference, and then repeated for the successive ones. The data developed by the Emerson gas analyzer are provided in [ppm], as shown in Figure 4.1, making it necessary a conversion procedure in order to obtain the results of the tests in a more useful unit of measure.

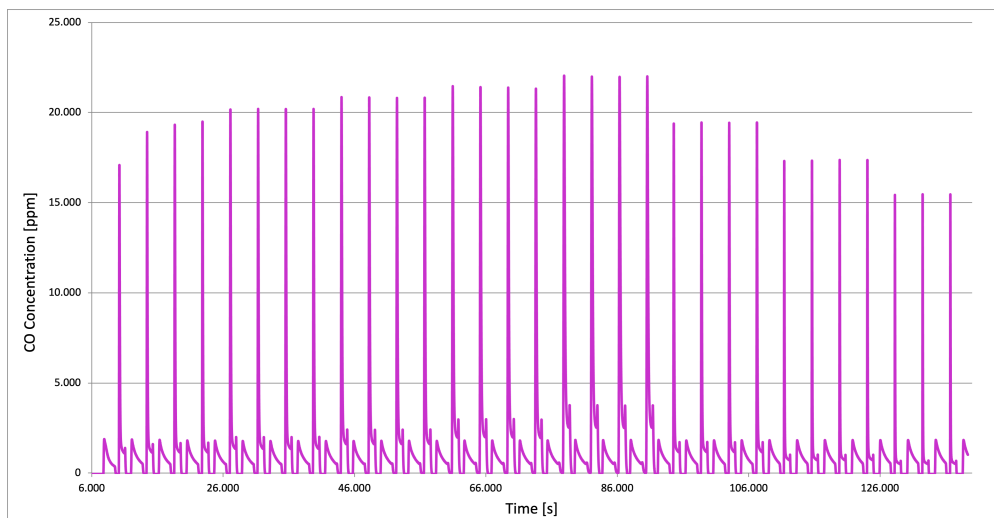


Figure 4.1: CO concentrations expressed [ppm] during Test (I).

Before starting with the processing of the data, the oxidations have been identified and separated into different curves. Then the data are converted in accordance to the following procedure:

- Firstly, according to the [ppm] definition, the measured data are divided by  $10^6$  to obtain a dimensionless quantity;

$$\frac{[ppm]}{10^6} = [-] \quad (4.1)$$

- The dimensionless quantities are then multiplied by the oxidation volumetric flow rate [Nml/min] and divided by 60 [s/min] to obtain [Nml/s], where N indicates the NTP (Normal Temperature and Pressure) operating conditions (T=293,15 K, p=1 atm);

$$\left[ \frac{Nml}{min} \right] \frac{1}{60} \left[ \frac{min}{s} \right] = \left[ \frac{Nml}{s} \right] \quad (4.2)$$

- Then, following the ideal gas law, [ml] are divided by 22,4 [l], which is the molar volume of an ideal gas, and multiplied by  $10^3$  to convert it into [ $\mu$ moles];

$$\left[ \frac{Nml}{s} \right] \frac{1}{22,4} \left[ \frac{moles}{l} \right] 10^3 = \left[ \frac{\mu moles}{s} \right] \quad (4.3)$$

- Finally, the obtained values in [ $\mu$ moles/s] are divided by the SFNM-04 mass to obtain a normalized value in [ $\mu$ moles/s/g];

$$\left[ \frac{\mu moles}{s} \right] \left[ \frac{1}{g} \right] = \left[ \frac{\mu moles}{s \cdot g} \right] \quad (4.4)$$

The results of the 4 cycles performed with the same volumetric flow rate are averaged to obtain a unique set of CO production rates value, as shown in Figure 4.2.

To obtain the CO production yield in [ $\mu$ moles/g], an integration method is required to evaluate the area below the oxidation curve. As illustrated in Figure 4.2, the tail of oxidation curve plotted in [ $\mu$ moles/s/g] does not seem to reach the zero values, but it stabilize at around 1 [ $\mu$ moles/s/g]. This phenomenon could lead to wrong and non-reliable CO yield if the integration method is applied without implementing a correction of the curve. The correction has been applied by considering the first derivative of the production rate and by setting a breaking point for the curve in correspondence to a value of the ratio between the relative change of the production rate and the production rate below a tolerance value equal to

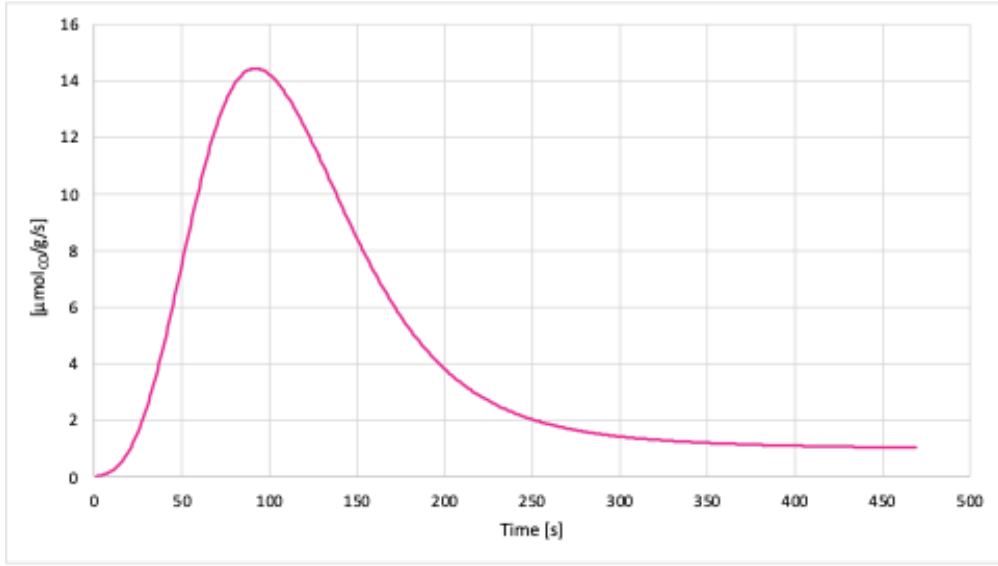


Figure 4.2: CO production rate in  $[\mu\text{moles/s/g}]$  during the oxidation step.

0,05%. The adopted procedure is quite conservative but it allows to obtain a good approximation of the fuel yields identifying the instant of time in which the tail of the curve can be considered stabilized at a constant value. Once the breaking point instant  $t_{BP}$  has been identified, a straight line that connects the origin with the breaking point has been drawn. The correction method and the corresponding corrected curve, evaluated as the difference between the original curve and the straight line, are shown in Figure 4.3 and 4.4 respectively.

Once the curve has been corrected, the CO yield expressed in  $[\mu\text{moles/g}]$  can be finally evaluated as the area below the curve, following Eq. 4.5.

$$CO\ Yield\ \left[\frac{\mu\text{moles}}{g}\right] = \int_0^{t_{BP}} y(t)\ dt \quad (4.5)$$

The gas analyzer provides concentration values each second, allowing to simplify Eq. 4.5 into 4.6.

$$CO\ Yield\ \left[\frac{\mu\text{moles}}{g}\right] = \sum_{n=0}^{t_{BP}} (y(t) \cdot \Delta t) \quad (4.6)$$

The same procedure described up to now has been applied to every oxidation of the cycles obtaining the production rates curves for every value of volumetric flow

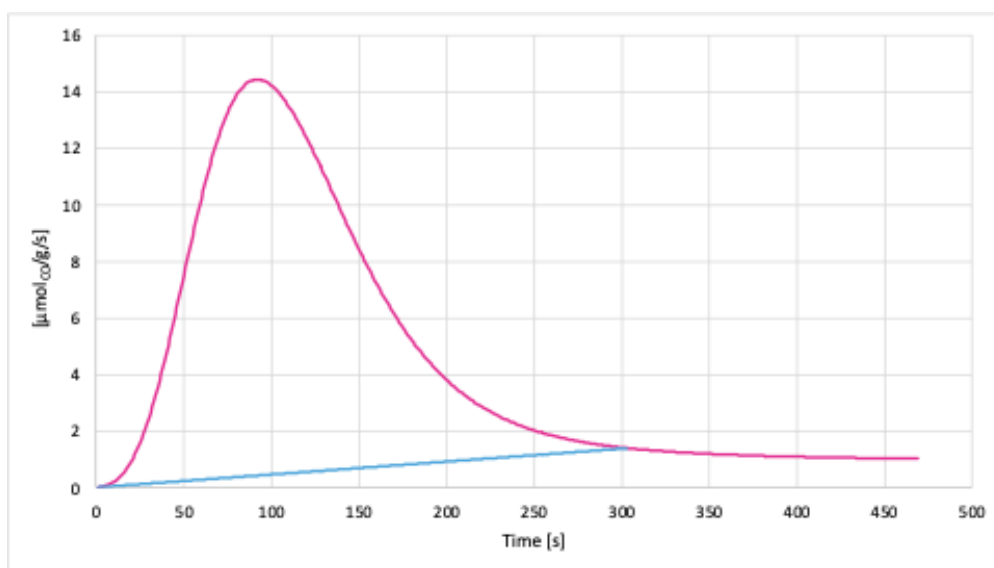


Figure 4.3: Correction method: break point identification in the original curve by means of the straight line.

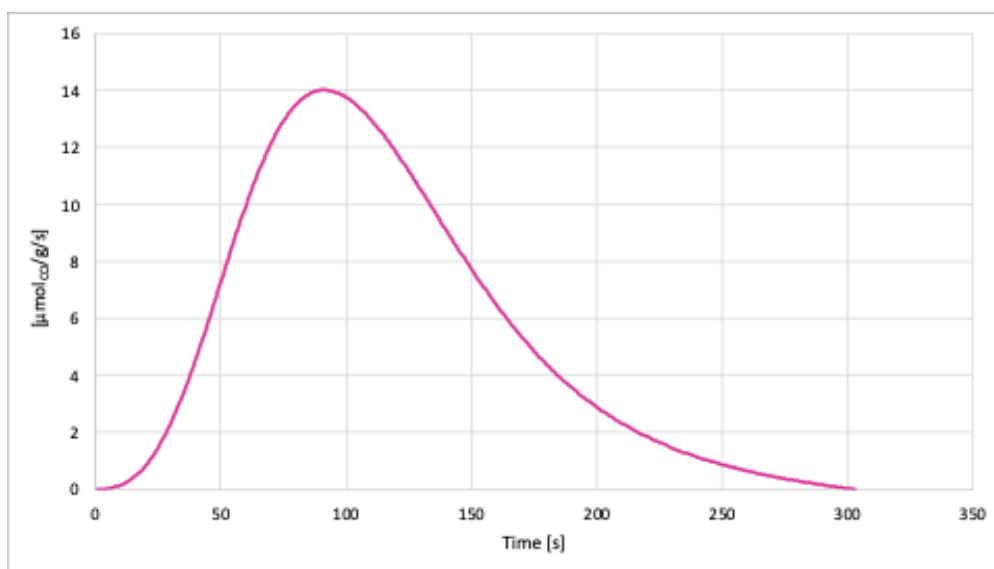


Figure 4.4: Correction method: corrected CO production curve.

rates and consequently, the total CO yields have been evaluated. The outcomes of Test (I) are illustrated in Figure 4.5.

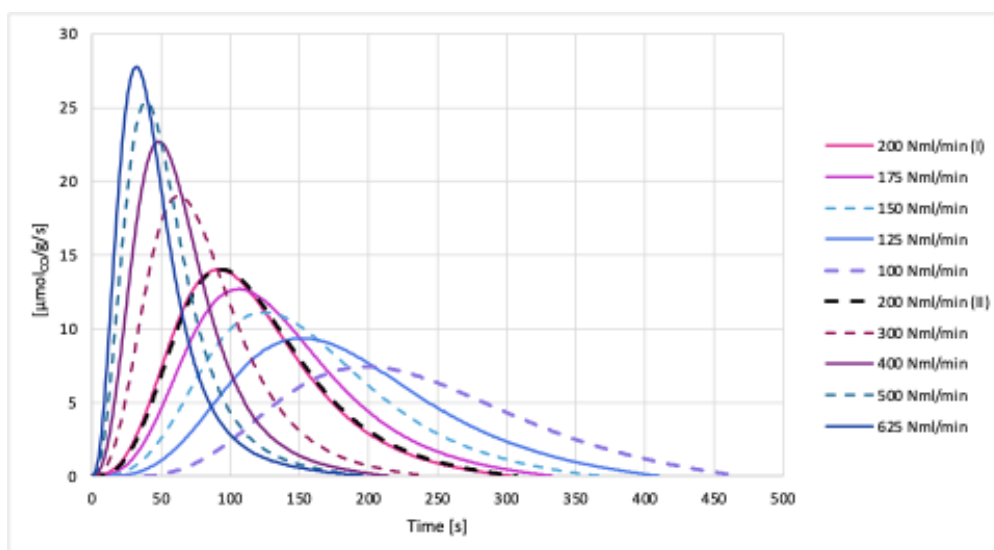


Figure 4.5: Test (I) results in terms of CO production rates [ $\mu\text{moles/s/g}$ ].

## 4.2 Test (I)

The first test has been conducted with a sample mass  $m=200$  mg, with oxidation mass flow rates varying in the range 100-625 Nml/min. More specifically, it is composed by 10 different sections, characterized by 10 values of oxidation flow rates: 200 (I), 175, 150, 125, 100, 200 (II), 300, 400, 500, 625 Nml/min.

Results of Test (I), already introduced in Figure 4.5, show an upward trend in the CO production peaks while increasing the oxidation volumetric flow rates. More in details, the highest peak of CO production rate is  $28.02 \mu\text{moles/s/g}$ , reached in correspondence of an oxidation flow rate equal to 625 Nml/min. On the other hand, while increasing the flow rates, the curves tend to tighten and stretch upwards with a correspondent decrease of the area underlying the graph and, limiting the CO yields in  $\mu\text{moles/g}$ . The highest CO yield is obtained with a volumetric flow rate during oxidation equal to 150 Nml/min, while the lowest value is obtained with the highest mass flow rate, resulting in a reduction of the total yield of about 14% when compared to the highest value. Table 4.3 shows the results of Test (I) both in terms of CO peak rates and total yield.

As it is visible both from the outcomes, two sections at 200 Nml/min have been performed to verify the repeatability of the fuel yields. The results obtained from the group of redox cycles performed at 200 Nml/min, better shown in the

Oxidation flow rate [Nml/min]	CO total yield [ $\mu$ moles/g]	CO peak rate [ $\mu$ moles/s/g]
100	1522.6	8.18
125	1618.7	9.95
150	1650.8	11.62
175	1648.5	13.15
200 (I)	1625.2	14.44
200 (II)	1636.6	14.46
300	1590.8	19.36
400	1536.7	22.99
500	1476.8	25.67
625	1413.9	28.02

Table 4.3: Test (I): results in terms of CO peak rates and total CO yield.

magnification in Figure 4.6, are encouraging and indicate the repeatability of the SFNM-04 sample.

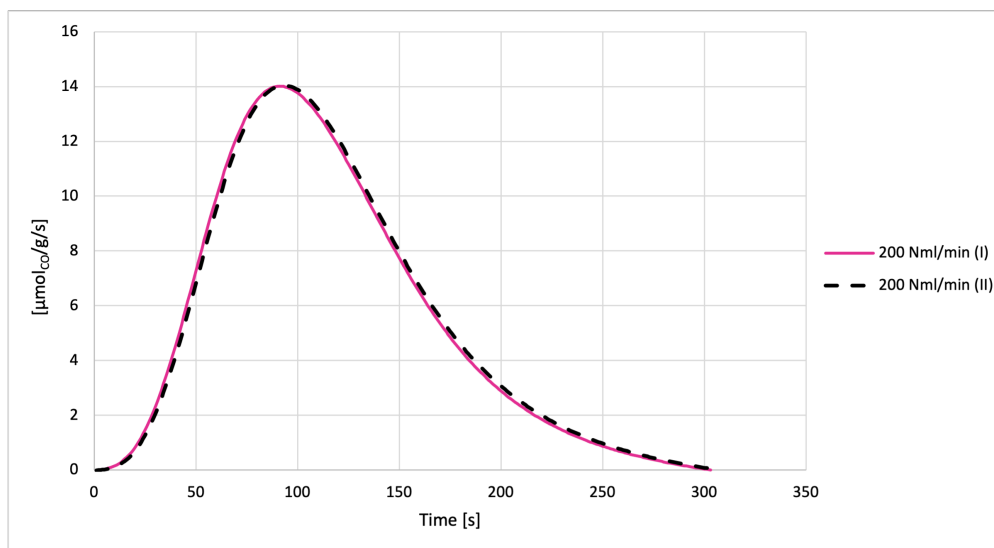


Figure 4.6: Repeatability test performed by testing the material two times with the same oxidation flow rate equal to 200 [Nml/min].

### 4.3 Test (II)

The second test has been performed reducing the sample mass down to  $m=50$  mg with the same range of oxidation volumetric flow rates, but different values. It is composed of 9 sections, with the following sequence of imposed oxidation flow rates: 125, 156.25, 175, 200, 300, 400, 500, and 625 Nml/min. The results of Test (II) are shown in Figure 4.7.

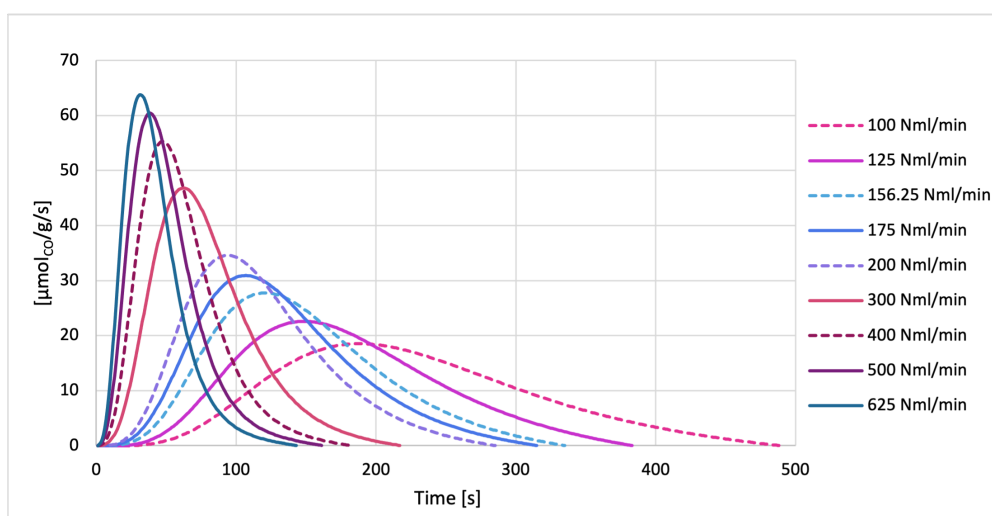


Figure 4.7: Test (II) results in terms of CO production rates [ $\mu\text{moles/s/g}$ ].

As for Test (I), also in this case the trend of the curves is to shrink and to elongate when increasing the volumetric flow rate. Consequently, the peak rate is reached faster and the reaction seems to be finished after a shorter interval of time. The CO production rates are in general higher with respect to Test (I); the maximum peak rate value is reached again for the higher value of the oxidation flow rate, but it is two times higher when compared to the rate reached with the same flow in Test (I). Also when considering the total CO yields, values obtained in this test with lower mass of the sample are higher. The outcomes of Test (II) are listed in Table 4.4.

Oxidation flow rate [Nml/min]	CO total yield [ $\mu$ moles/g]	CO peak rate [ $\mu$ moles/s/g]
100	4003,1	20,55
125	3810,5	24,80
156.25	3888,1	29,66
175	3930,2	32,59
200	3881,8	36,17
300	3674,1	48,10
400	3408,0	56,40
500	3149,9	61,42
625	2834,5	64,65

Table 4.4: Test (II): results in terms of CO peak rates and total CO yield.

#### 4.4 Test (III)

The sample mass is further reduced in Test (III) down to  $m=20.7$  mg. Test (III) has been performed again varying the oxidation flow rate in the range  $100\div 625$  Nml/min. The selected values are 100, 125, 165.6, 207, 258.75, 300, 400, 500, and 625 Nml/min. Figure 4.8 shows the results obtained with the experimental conditions described above.

While the shape of the curves is similar to the ones resulting from Test (I) and Test (II), the total CO production for equal values of the mass flow rates keeps increasing reaching a maximum value of  $8828.3 \mu\text{moles/g}$ . The peak values of the CO production rate and the total CO yields are listed in Table 4.5.

Differently from the other tests, the reduction of the mass appears to have influenced the peaks of CO production rates. In the previous analysis, with higher values of sample mass, the rate of fuel production showed a continuing upwards trend with the increase of oxidation flow rates. Moreover, the curves representative of the cycles performed with higher flow rates continued to stretch upwards corresponding to higher peaks reached in less time for increased flow rate values. In this case, the results of the cycles performed with 500 and 625 Nml/min showed similar trends, reaching comparable CO rate values ( $120.66$  and  $121.82 \mu\text{moles/s/g}$

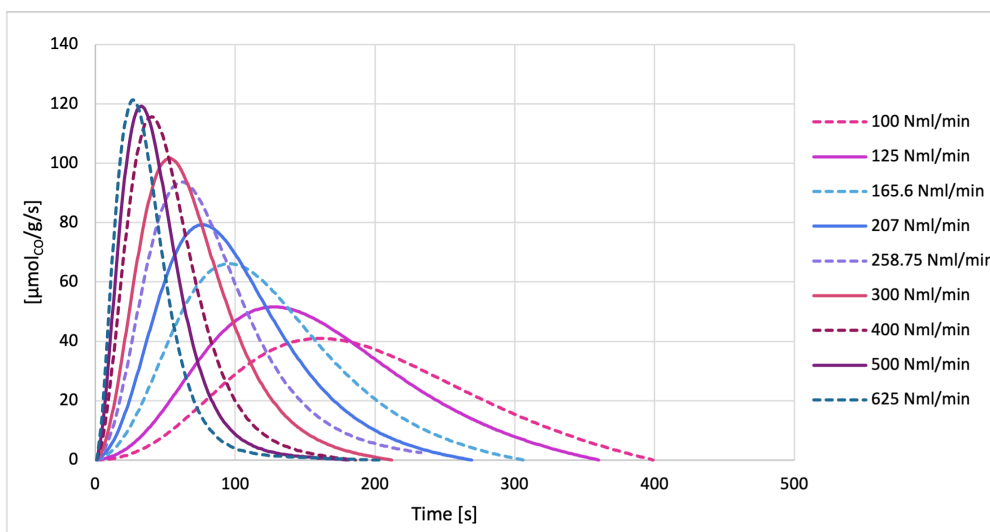


Figure 4.8: Test (III) results in terms of CO production rates [ $\mu\text{moles/s/g}$ ].

Oxidation flow rate [Nml/min]	CO total yield [ $\mu\text{moles/g}$ ]	CO peak rate [ $\mu\text{moles/s/g}$ ]
100	8204.0	47.35
125	8764.9	56.28
165.6	8828.3	69.73
207	8645.2	82.09
258.75	8555.8	95.31
300	7865.4	103.84
400	6973.0	117.43
500	6054.0	120.66
625	5276.5	121.82

Table 4.5: Test (III): results in terms of CO peak rates and total CO yield.

respectively).

## 4.5 Test (IV)

Test (IV) has been performed continuing to reduce the mass of the sample, equal in this case to  $m=10$  mg. The result of the nine section carried out with oxidation volumetric flow rates equal to 100, 125, 145, 193, 242, 300, 400, 500, 625 Nml/min are displayed in Figure 4.9.

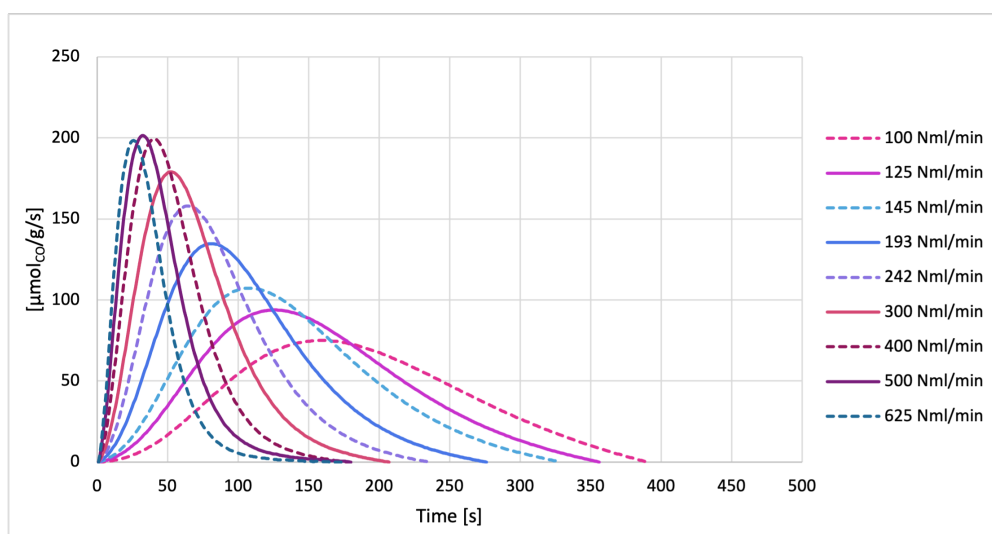


Figure 4.9: Test (IV) results in terms of CO production rates [ $\mu\text{moles/s/g}$ ].

In this test the resemblance between the curves at higher flow rates is even more pronounced. This similarity is reflected in the outcome values of the redox cycles performed with 400, 500, and 625 Nml/min which reach almost equal peaks in terms of CO rate production, as shown in Table 4.6.

Despite the CO rate peaks seemed to reach a plateau independent from the flow rates, the influence of the mass is still remarkable from the fact that the yields keep increasing while decreasing the SFNM-04 sample mass. Indeed, the specific yield achieved in this test with an oxidation flow rate equal to 500 Nml/min is equal to about 10000  $\mu\text{moles/g}$ , that is 66% increase with respect to the yield obtained in Test (III), performed with the same flow rate, but different mass of the sample.

Oxidation flow rate [Nml/min]	CO total yield [ $\mu$ moles/g]	CO peak rate [ $\mu$ moles/s/g]
100	14869.62	87.41
125	15863.95	102.47
145	16015.61	114.55
193	15535.33	140.34
242	14697.70	162.73
300	13728.48	183.20
400	12045.15	202.16
500	10303.49	204.06
625	8428.42	198.84

Table 4.6: Test (IV): results in terms of CO peak rates and total CO yield.

## 4.6 Test (V)

The SFNM-04 mass has been further reduced to  $m=5$  mg to better investigate the dependence of the fuel yields on the sample mass parameter. The test is again composed by nine different sections, each one performed with a different value of oxidation flow rates. More in details, the test has been done with flow rates equal to 100, 121, 150, 200, 250, 300, 400, 500 and 625 Nml/min. The outcomes are shown in Figure 4.10 and also listed in Table 4.7.

From the results, it is evident that also when considering a low value for the sample mass, the influence of this parameter on the CO total yields is still present. Even though the shape of the curves at high flow rates seem more and more similar with the decreasing of the mass sample, the yields of tests performed with different SFNM-04 mass keep increasing. Test (V) returned extremely high yields, approaching 30000  $\mu$ moles/g. This can be caused by the setup chosen for this first set of five tests; it is plausible that the sample mass powders in the crucible are not effectively traversed by the gas flow, but lapped only on the upper surface, not allowing the mass to completely react. If this is the case, high values of SFNM-04 should be more affected by this phenomenon. Indeed, tests performed with the higher values of mass of the sample are the ones characterized by lower specific

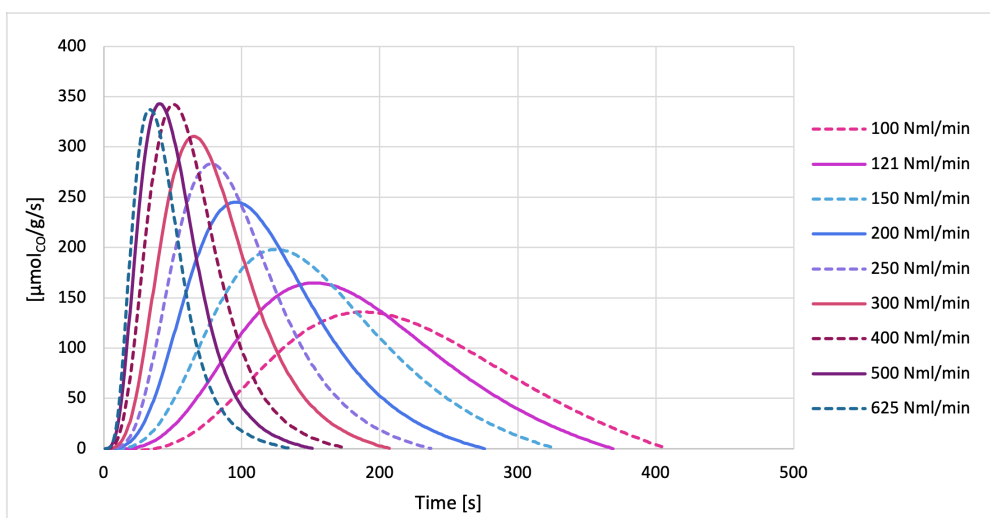


Figure 4.10: Test (V) results in terms of CO production rates [ $\mu\text{moles/s/g}$ ].

Oxidation flow rate [Nml/min]	CO total yield [ $\mu\text{moles/g}$ ]	CO peak rate [ $\mu\text{moles/s/g}$ ]
100	26623.97	166.71
121	28479.91	188.48
150	28891.50	217.39
200	27916.23	260.89
250	26202.14	296.88
300	24520.48	323.02
400	21502.50	352.56
500	18116.96	351.74
625	14864.81	343.08

Table 4.7: Test (V): results in terms of CO peak rates and total CO yield.

yields, thus confirming the hypothesis made. To address this issue, two tests with the tube-in-tube configuration have been performed.

## 4.7 Test (VI)

As already mentioned, the tube-in-tube configuration consists in a reduction of the reactor area by inserting in the external tube a secondary alumina tube with a 8 mm of internal diameter. In the latter the sample has been dispersed in the quartz wool, added before and after the sample mass to ensure the position of the SFNM-04 powders during testing conditions.

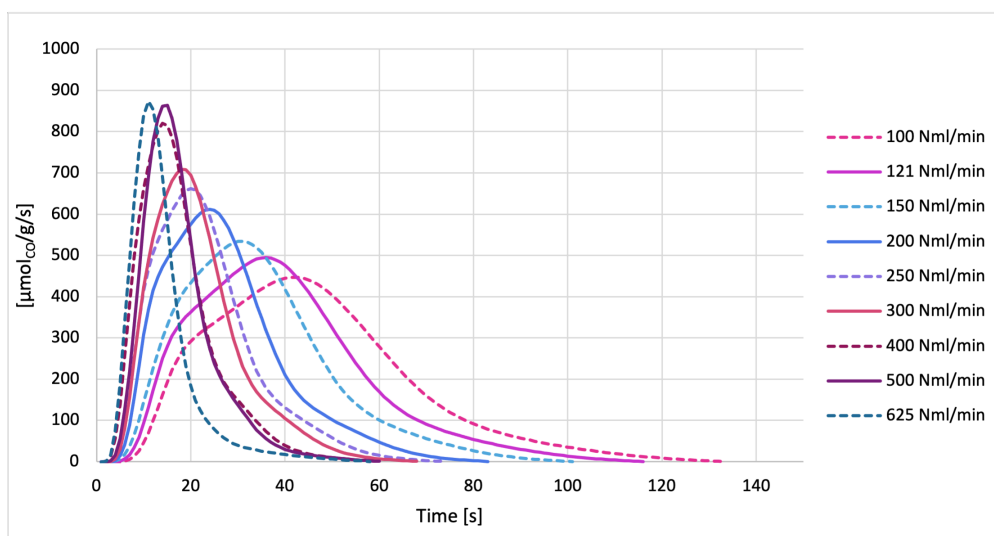


Figure 4.11: Test (VI) results in terms of CO production rates [ $\mu\text{moles/s/g}$ ].

The microreactor setup is shown in Figure 3.14. This configuration ensures that all the sample mass is directly exposed by the gas flow, differently from the previous configuration. However, this configuration can not be used with high values of SFNM-04 mass. Test (VI) has been performed with a sample mass equal to  $m=4.6$  mg firstly because the high mass values tested with the crucible configuration (e.g. 200 mg) can not be tested with the tube-in-tube configuration, and secondly because the chosen value is similar to the mass used in Test (V), allowing to direct compare the outcomes of the two tests which differs only for the microreactor setup. Test (VI) has been performed, in fact, considering the same oxidation flow rate values employed in Test (V). The outcomes of Test (VI) are shown in Figure 4.11. As expected, Test (VI) results in higher CO production rates. The curves are narrower and reach higher peaks. This is due to the higher surface to volume ratio in the tube-in-tube configuration with respect to the crucible.

Even though the peaks are more than two times higher than those obtained in Test (V), the normalized yields with respect to the sample mass are unexpectedly lower; this is due to the higher gas velocities in the inner tube. This aspect will be better discussed in Chapter 5. Results of Test (VI) are listed in Table 4.8.

<b>Oxidation flow rate</b>	<b>CO total yield</b>	<b>CO peak rate</b>
[Nml/min]	[ $\mu$ moles/g]	[ $\mu$ moles/s/g]
100	22221.63	462.61
121	20907.29	510.02
150	19267.04	549.94
200	17402.30	627.16
250	15733.79	675.07
300	14672.13	721.22
400	13493.21	830.07
500	12680.92	874.39
625	9849.52	880.15

Table 4.8: Test (VI): results in terms of CO peak rates and total CO yield.

More in general, the outcomes of this test again show a reduction of the yield when increasing the flow rate at constant sample mass. But in this case, the specific yields at higher flow rates seem to reach a plateau in a region apparently not dependent on the oxidation mass flow rate it self.

## 4.8 Test (VII)

The last test, herein referred to as Test (VII), has been performed with the lowest value of sample mass, equal to  $m=1.3$  mg. The experimental procedure has been carried out considering again the same oxidation volumetric flow rate values used both in Test (V) and in Test (VI). The curves resulting from the raw data processing are shown in Figure 4.12.

The results of this last test confirm the evidence found in Test (VII): while the CO rate peaks keep increasing, the total CO yields at high flow rate reach a value

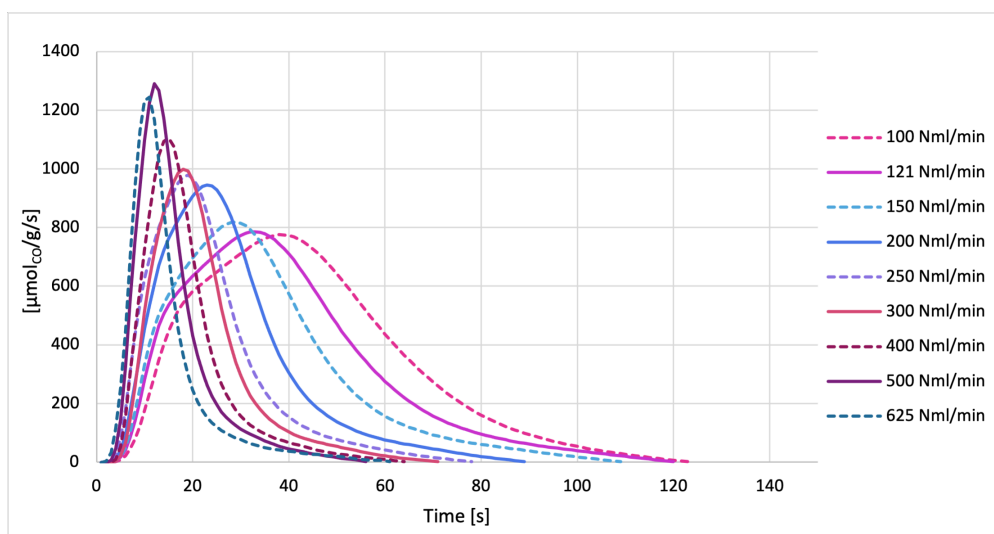


Figure 4.12: Test (VII) results in terms of CO production rates [ $\mu\text{moles/s/g}$ ].

independent from the flow rate. The peak values of the CO production rate and the total CO yields are listed in Table 4.9.

Oxidation flow rate [Nml/min]	CO total yield [ $\mu\text{moles/g}$ ]	CO peak rate [ $\mu\text{moles/s/g}$ ]
100	39321.48	822.25
121	35028.47	824.98
150	30481.40	854.16
200	26494.72	978.19
250	22174.94	1006.68
300	18783.92	1024.10
400	16704.42	1127.86
500	16140.11	1316.63
625	13855.83	1262.88

Table 4.9: Test (VII): results in terms of CO peak rates and total CO yield.

# Chapter 5

## Summary and Discussion

### 5.1 Influence of Sample Mass

As previously said, the tests has been performed by varying the SFNM-04 sample mass starting from  $m=200$  mg down to  $m=1.3$  mg.

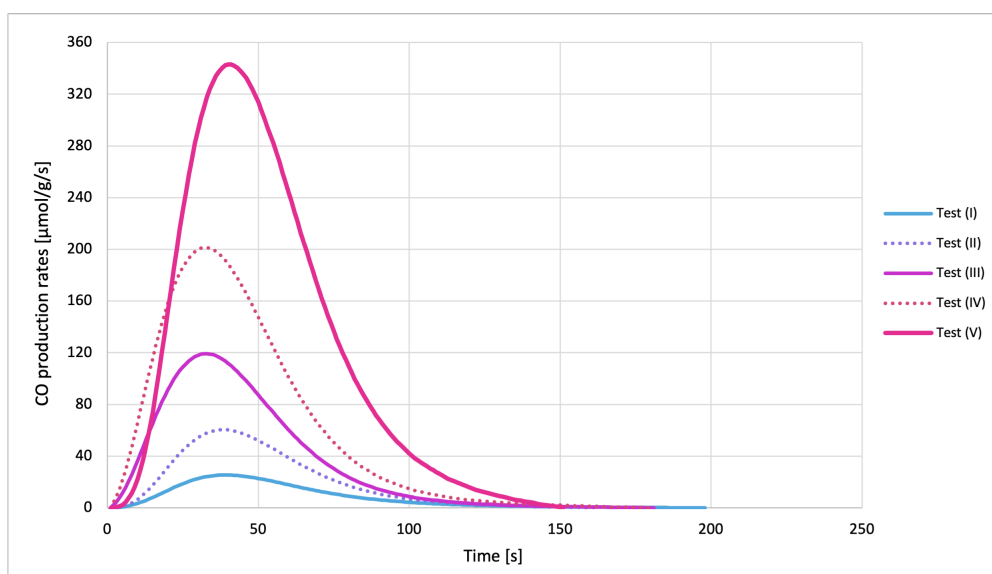


Figure 5.1: CO production rates curves: comparison at fixed setup configuration (crucible) and oxidation flow rate (500 Nml/min).

In order to evaluate the sample mass influence on the CO yields and CO production rates, all the other parameters must be kept constant. The first set of

tests, from Test (I) to Test (V) has been performed considering the same reactor setup and having in common some of the oxidation flow rate values, allowing for an analysis only with sample mass variations. In spite of this reasoning, Figure 5.1 shows the average curves resulted from tests (I) to (V), performed with the crucible configuration. The mass of the sample has been decreased from  $m=200$  mg in Test (I) down to  $m=5$  mg in Test (V). All the curves refers to sections of the tests performed with the same flow rate equal to 500 Nml/min. From Figure 5.1 it is evident a gradual increase upwards. The curves become, in fact, taller and wider with the sample mass decrease meaning that a lower sample mass value results in a higher specific yield, releasing more CO per unit of sample mass. Moreover, the curves tend to reach the peaks of CO production rates more or less at the same time instant, ranging between 35 and 40 [s]. Also the breaking points  $t_{BP}$ , identified as the instant of time in which the oxidation can be considered ended, are comparable. Indeed, a sample mass variation does not seem to translate the curves left or right on the x-axis, meaning that it does not appear to affect the timing of the oxidation, but it seems to alter the response in terms of CO production rates and specific yields. More specifically, a decrease of the sample mass corresponds to a taller and wider curve, resulting in an increase of the specific yields. The yields of tests performed with different SFNM-04 mass kept increasing, reaching in Test (V) values so high (in the order of 30000  $\mu\text{moles/g}$  for low values of flow rates) that they can not be considered reliable. To explain this trend, it has been supposed that the most precise yields are the ones obtained with lower sample mass values. As mentioned in paragraph 4.7, it is plausible that when high values of sample mass are considered, the specific yields are limited by the lower surface-to-volume ratio which does not allow the sample to react completely, resulting in a lower CO release per unit mass. Conversely, when smaller sample mass are used for the cycles, a relatively high percentage of the sample react, consistently with the higher specific yields observed. The upward trend of the specific yields is clearly visible from Figure 5.2.

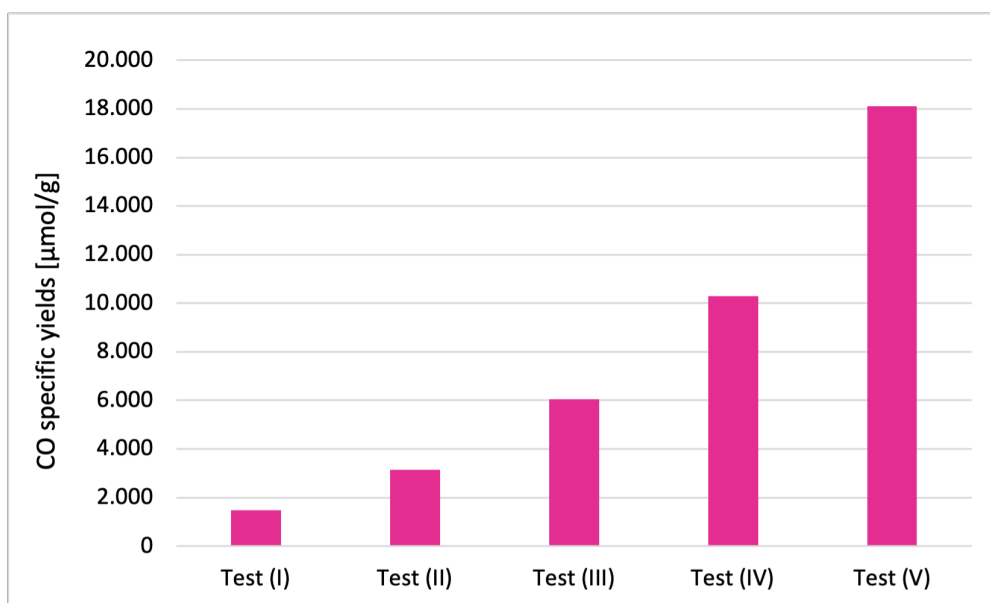


Figure 5.2: CO specific yields: upward trend resulting from a gradual decrease of SFNM-04 mass.

## 5.2 Influence of the Oxidation Flow Rates

The influence of the oxidation flow rate both on the yields and on the CO production rate has already been shown in the previous chapter. Indeed, all the tests have been performed varying only the flow rates among the sections, allowing to analyze the results as function of the oxidation flow rates variation.

As already outlined, the curves tend to stretch upwards with the increase of the oxidation flow rates, reaching higher CO production rate peaks. It must be noticed that the gap between one flow rate and the successive is smaller for lower flow rate values. To be more accurate, the first section of Test (II) has been performed with an oxidation flow rate equal to 100 Nml/min, while the second one with 125 Nml/min. The difference is 25 Nml/min. If the last two sections of the same test are considered, the difference between the selected flow rates is higher, corresponding to 125 Nml/min. Therefore, the gap between one curve and the successive one is not proportional to the flow rates variation meaning that curves at higher flow rates seem to become more and more similar. This effect is even more pronounced when a lower sample mass is considered. Figure 5.3b shows, in

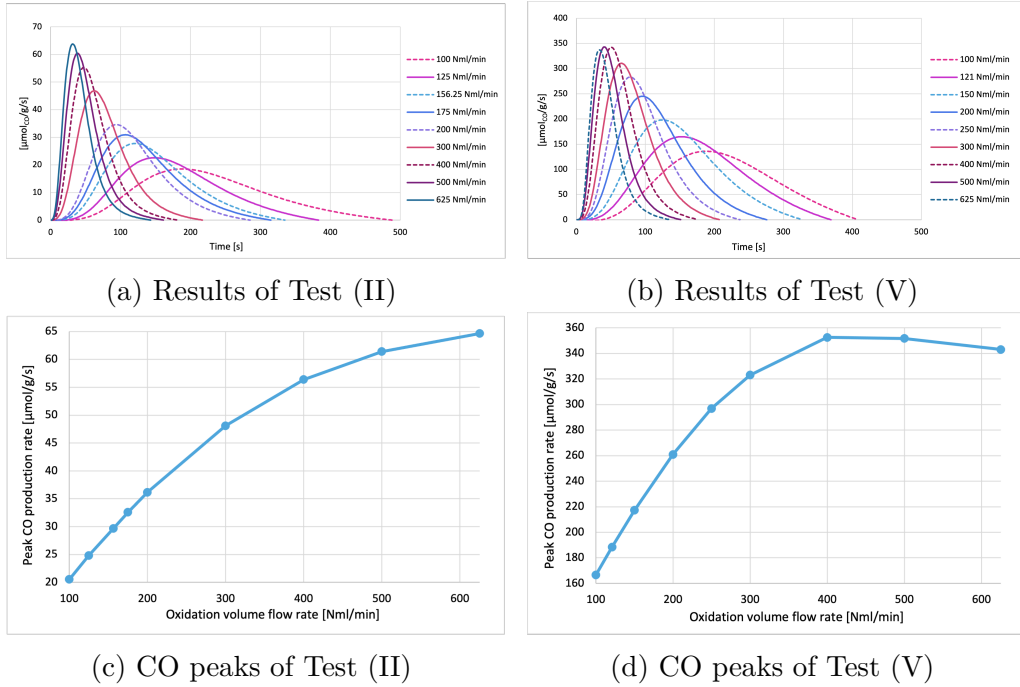


Figure 5.3: Influence of the oxidation mass flow rates on the results of two tests as reference. Results of Test (II) 5.3a and Test (V) 5.3b; Peaks of CO production rate as function of the oxidation volume flow rate again for Test (II) 5.3c and for Test (V) 5.3d.

fact, the results of Test (V) which has been performed with a SFNM-04 mass equal to  $m=5$  mg. The curves of the last three sections, performed with mass flow rates equal to 400, 500 and 625 Nml/min, seems to tend towards nearly identical shape. The similarity in terms of CO production is more evident in Figure 5.3d which illustrates the CO production rate peaks as function of the oxidation flow rates, again for Test (V). The figure clearly shows a plateau indicating that, at higher flow rates, the shape of the curves tends to a constant shape, apparently independent from the oxidation flow rates. Unfortunately, the same plateau has not been reached with the crucible configuration in terms of specific yields, which tend to decrease with increasing flow rate. However, when the tube-in-tube configuration has been considered, the CO specific yields reached a plateau again in correspondence of tests performed with high flow rates, meaning that in these experimental conditions, the CO yields can be considered not dependent on the oxidation flow rates. Figure 5.4a and 5.4b show the specific yields as function of the oxidation

volumetric flow rates for the set of tests performed with the crucible configuration and for the tube-in-tube configuration respectively.

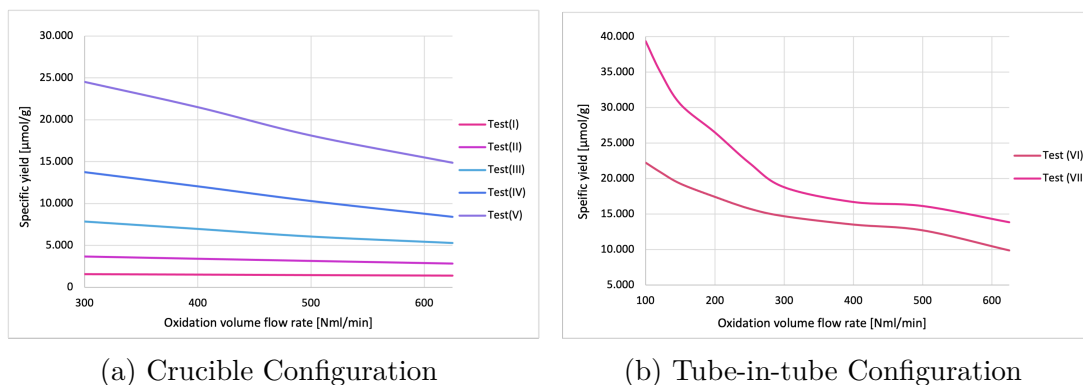


Figure 5.4: Specific CO yields as function of oxidation flow rates: 5.4a tests performed with the crucible configuration; 5.4b tests performed with the tube-in-tube configuration.

### 5.3 Influence of the Reactor Setup

Results of Test from (I) to (V), obtained with the alumina crucible, are here compared to the outcomes of Test (VI) and (VII), performed with the tube-in-tube configuration to assess the influence of the reactor setup. In order to properly compare the two different setups, all the other parameters must be kept constant. For this reason, Test (VI) has been performed with identical mass flow rate values to Test (V) and also comparable sample masses ( $m=4.6$  mg in Test (VI) and  $m=5$  mg in Test (V)), allowing for a direct comparison. Figure 5.5 illustrates the comparison between the curves obtained in Test (V) and Test (VI) with oxidation flow rate equal to 150  $\text{Nml/min}$  (Figure 5.5a) and 400  $\text{Nml/min}$  (Figure 5.5b). Figure 5.5 shows a higher and thinner curve for Test (VI), performed with the tube-in-tube setup, resulting in a faster reaction. Concerning the yields, Test (VI) is expected to provide higher values due to the higher surface to volume ratio, which allow more SFNM-04 mass to be exposed to the gas stream and, consequently, to react. However, as already mentioned in paragraph 4.7, results of Test (VI) show specific yields unexpectedly lower than Test (V) for the same oxidation flow rate values.

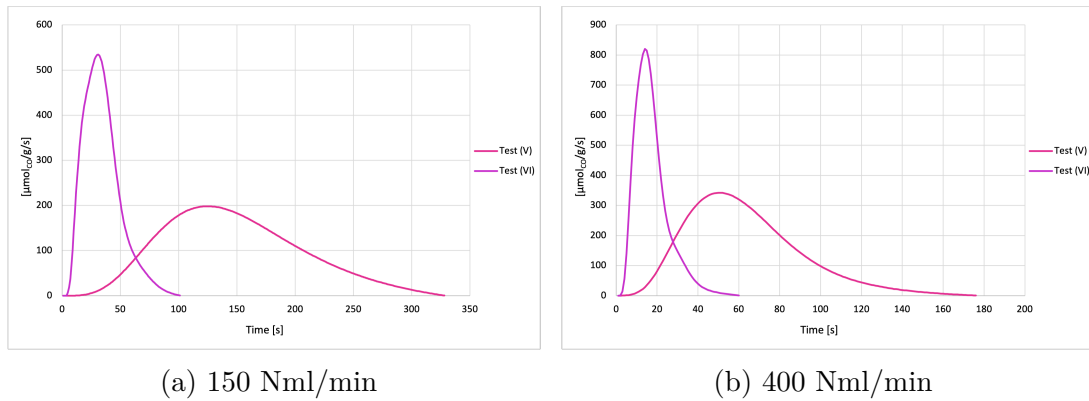


Figure 5.5: Reactor setup influence: CO production rate curves comparison of Test (V) and Test (VI).

The outcomes in terms of yields are shown in Figure 5.6 both for Test (V) and Test (VI).

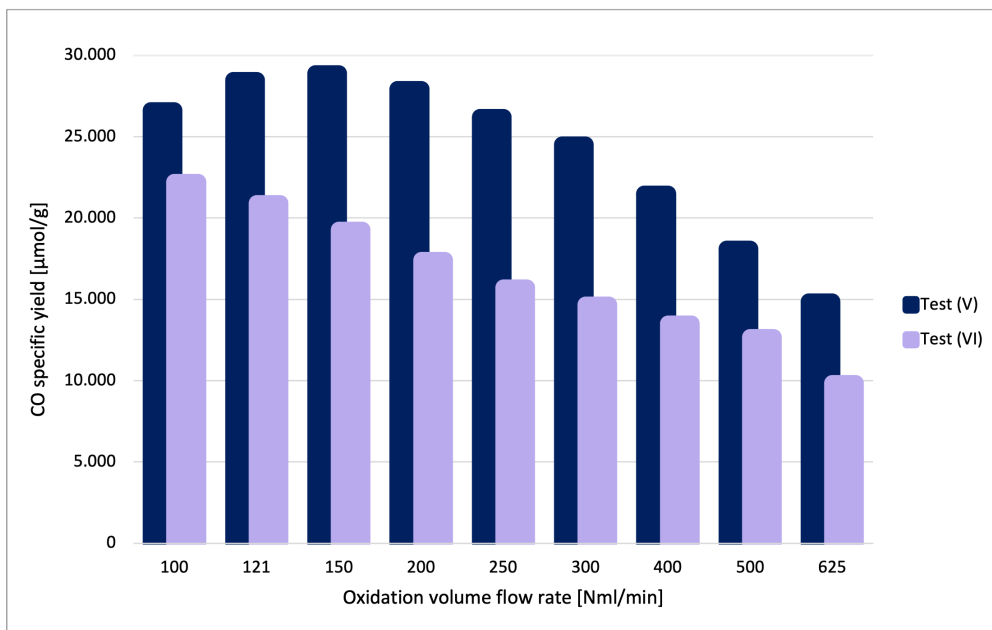


Figure 5.6: Reactor setup influence: CO specific yields comparison of Test (V) and Test (VI) at fixed flow rates.

Up to now, different tests have been compared as function of oxidation flow rates. But this is possible only if the same reactor setup is considered. The

comparison at fixed flow rates, in fact, loses sense when tests performed with different reactor geometries are cross-checked. This is due to the fact that, at the same flow rates, the sample masses in the two configurations are not exposed to the same gas velocity due to the different cross sections. For this reason, the gas velocity is the most appropriate parameter to compare yields obtained with different setups. In order to obtain the diagram with the gas velocity on the x-axis, the latter has to be evaluated as follows:

- Firstly, the cross sections for the crucible and tube-in-tube configuration are evaluated by considering the diameters of the outer and inner tubes (equal to  $d=32$  mm and  $d=8$  mm respectively);

$$A_{inner} = \pi \cdot \frac{D_{inner}^2}{4} = 0.503 \text{ cm}^2 \quad (5.1)$$

$$A_{outer} = \pi \cdot \frac{D_{outer}^2}{4} = 8.04 \text{ cm}^2 \quad (5.2)$$

- The flow rate in Nml/min is then multiplied by the actual operating temperature inside the reactor ( $T=850^\circ\text{C}$ ) and divided by the normal temperature ( $T=20^\circ\text{C}$ ) to obtain the real flow rate in ml/min, which is equal to  $\text{cm}^3/\text{min}$ . Both the temperatures in the ratio are expressed in K;

$$\left[ \frac{\text{Nml}}{\text{min}} \right] \left[ \frac{T_{operating}}{T_{normal}} \right] = \left[ \frac{\text{ml}}{\text{min}} \right] = \left[ \frac{\text{cm}^3}{\text{min}} \right] \quad (5.3)$$

- Finally, the gas velocities are evaluated by dividing the flow rates in  $\text{cm}^3/\text{min}$  by the cross sections. The obtained value is then converted into cm/s.

$$\left[ \frac{\text{cm}^3}{\text{min}} \right] \cdot A [\text{cm}^2] \cdot \frac{1}{60} \left[ \frac{\text{min}}{\text{s}} \right] = v_{gas} \left[ \frac{\text{cm}}{\text{s}} \right] \quad (5.4)$$

Once the gas velocities have been evaluated, it is possible to obtain a diagram which illustrates the specific CO yields as a function of the gas velocities, hence for the same geometric configuration. The graph is shown in Figure 5.7.

As it can be seen from the graph, the two different reactor setups are characterized by different gas velocities. In particular Test (V), performed in the crucible configuration, covers lower velocities ranging from less than 1 cm/s up to about 5 cm/s. Therefore, from Figure 5.7 it is not possible to compare yields obtained

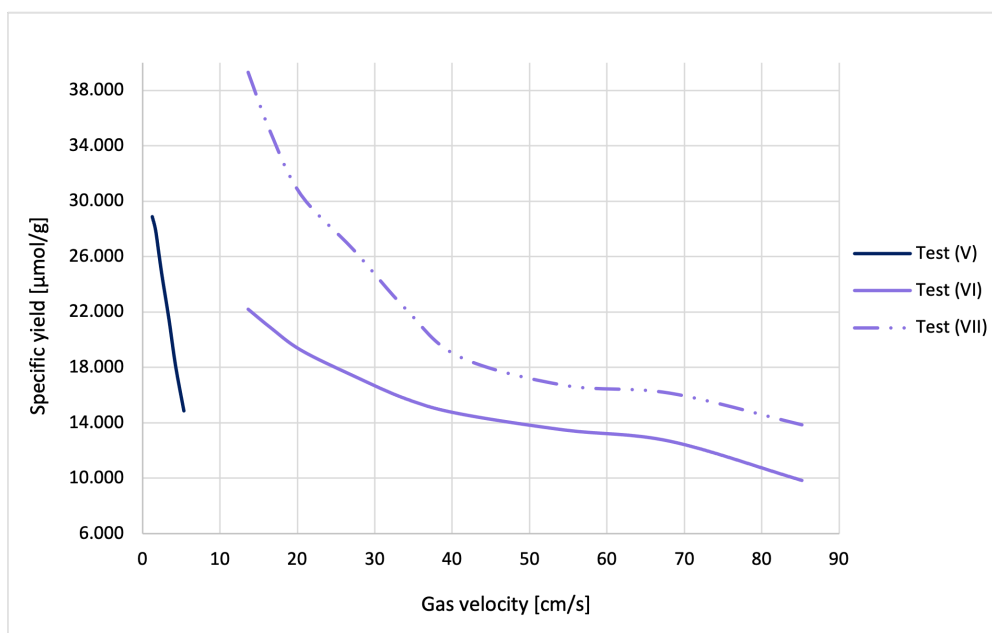


Figure 5.7: Reactor setup influence: CO specific yields comparison of Test (V), Test (VI) and Test (VII) at fixed gas velocities.

with the same velocity for the two different configuration. However the downward trend of the blue curve, representative of Test (V), clearly indicates that at higher velocities, the curve would be below the lilac curves, resulting in lower yields at fixed gas velocities.

## 5.4 Comparison of SFNM-04 with LSM-based perovskites

In this study, the SFNM-04 samples have been tested for the two-step  $\text{CO}_2$ -splitting. In this paragraph a comparison between the SFNM-04 double perovskite performance and the LSM-based perovskites analyzed in paragraph 2.3.3 is carried out. By comparing the fuel yield production listed both in Table 2.1 and 2.2, it is evident that the yields obtained in this study are at least one order of magnitude higher. For instance, the highest yield obtained while testing a sample mass of SFNM-04 equal to  $m=20.7$  mg in Test (III) is  $8828.3 \mu\text{moles/g}$ , while the highest yield among the ones reported is  $397 \mu\text{moles/g}$  for LSM40 [71].

From the comparison, it may seem that the SFNM-04 redox response in terms of CO yields is significantly enhanced with respect to other perovskites tested in literature. However, these results depend on several factors both from the raw data processing point of view but also different experimental conditions. Indeed, the integration method described in paragraph 4.1 used to evaluate the CO production per cycle must be the same used in the cited research to allow the comparison of the results. Unfortunately there are no information about the integration method used in the references associated to the values listed in Table 2.1 and 2.2. Hence, one likely explanation of the difference in CO yields may be represented by different integration methods. Moreover, not all the values reported in the tables were achieved with a microreactor simulation. Most of the yields were, in fact, obtained by means of Thermogravimetric Analysis (TGA) that is based on a different characterization method with respect to the microreactor, and could consequently lead to different results. Furthermore, TGA provides an instantaneous response to mass changes, thereby avoiding the gas analyzer influence on the results. This additional influence on the outcomes instead should be considered for the yields of this analysis. The results measured on the microreactor depend, in fact, on the gas analyser employed, which may not read the peaks correctly due to a slow response. Although the  $t_{90}$  of the EGA is much lower than the duration of the peaks, the analyzer could distort the results, making the peaks last longer. This delay in the response would strongly affect the final result of the integral, corresponding to an overestimation of the yields. Another important difference is represented by the operating conditions. Again most of the cycles performed in the references cited were carried out with different temperatures in reduction and oxidation, differently from the isothermal conditions considered for the tests of this study. In particular, all the yield values were obtained with reduction temperatures of about 1000°C or higher. This is probably due to the fact that those values are representative of thermal reductions performed with inert gases (He or Ar), therefore requiring higher reduction temperatures. Conversely, the reductions in this study are fuel-aided. Reduction steps have been performed, in fact, with a gas mixture composed by 10% H<sub>2</sub>/N<sub>2</sub> for 30 min, allowing for a lower reduction temperature  $T_{red}=850^{\circ}\text{C}$ . Despite this lower temperature, fuel-aided reductions are more effective in terms of fuel production with respect to thermal reductions.

# Chapter 6

## Conclusion

The analysis presented in this thesis has been carried out at the CO<sub>2</sub> Circle Lab, located in Turin, in collaboration with the University of Udine (UNIUD) and the Massachusetts Institute of Technology (MIT). The objective of the study is to propose a new double-perovskite structured material, here named as SFNM-04, with composition  $Sr_2FeNi_{0.4}Mo_{0.6}O_{6-\delta}$  for the thermochemical CO<sub>2</sub> splitting cycle to produce CO and also to define the influence on the oxygen carrier yields of the following parameters: sample mass, gas flow rate, and geometric configuration of the system. The redox cycles have been then conducted maintaining the same temperature conditions, i.e. isothermal cycles at  $T_{red}=T_{oxy}=850^{\circ}\text{C}$ , and gas atmospheres, i.e. 10% H<sub>2</sub>/Ar in reduction, 20% CO<sub>2</sub>/Ar in oxidation. A first set of five tests has been carried out in a microreactor with crucible configuration: the sample, in powder form, has been placed in an alumina crucible. The latter has been then positioned in the center of the reactor. The CO produced during oxidation has been monitored using EGA. The five tests involved masses progressively decreasing from one test to the next. Specifically, in order: 200, 50, 20.7, 10, and 5 mg. Each test was composed by different sections. Each sections involved oxidizing volumetric flow rates varying between 100 and 625 Nml/min (kept constant in the single section). Results have been analyzed in terms of CO yields, normalized to the mass of SFNM-04. The outcomes highlights that, at constant sample mass, the CO yield decreases as the flow rate increases. From the point of view of the influence of the sample mass it has been observed that, at fixed flow rates, the CO yield tends to increase as the sample mass decreases, reaching untrustworthy

values. It has been assumed that the most accurate yields are those obtained with the smallest masses because of the low exposure of the sample mass to the gas flow rates. The crucible configuration is characterized by a low surface to volume ratio, which allow only a small percentage of the sample to react. In order to eliminate this influence, another configuration has been tested. Test (VI) and Test (VII) has been performed with the tube-in-tube configuration. The reactor area has been reduced by inserting in the external tube a secondary alumina. In the latter the sample has been dispersed in the quartz wool, which also ensured the position of the material. This configuration is characterized by higher surface to volume ratios, allowing higher percentage of the sample to be exposed to the gas streams. Test (VI) has been performed with a sample mass  $m=4.6$  mg, similar to the value chosen for Test (V), allowing for the direct comparison of the two different setups. More in general, the tests performed with the tube-in-tube configuration provides further experimental evidence to confirm the trend already outlined in the first set of tests. Moreover, the outcomes of these last two tests shows faster CO rate peaks and again a decrease of the CO yields as the flow rate increases, but reaching in this case a plateau in a region apparently independent of the flow rate itself. Test (VI) and Test (VII) also results in higher specific CO yields, consistent with the higher surface to volume ratio.

Surely future perspectives could be to further test the material in TGA in order to better understand the percentage of material that takes part in the reaction but also to compare the results with the studies cited in this thesis. The majority of the literature, in fact, is established on TGA-based tests. Moreover, by means of TGA it would be possible to test lower SFNM-04 mass values to search for an independence of the CO yields on the sample mass itself. Regarding the future of CL, the ideal future solution is represented by thermal reduction coupled with CSP. In this context, SFNM-04 surely represents a promising alternative as oxygen carrier for the two-step CO<sub>2</sub> splitting thermochemical cycle. The main attractiveness is represented by the possibility to lower the operating temperatures enabling a more easily integration of the CL process with CSP. But this technology suffers from multiple disadvantages, one of which is represented by the strong discontinuity of irradiance but also the temperatures which can be reached with current technologies. The oxygen carrier represents the key issue; current materials do not fulfill the requirements in particular for the reduction reaction, requiring fuel as

reductant to eliminate most of these issues. The CL technology could be exploited also for the H<sub>2</sub> production resulting in a system that at the same time produces H<sub>2</sub>, possibly from solar sources, and remove CO<sub>2</sub> from the atmosphere having at the end of the process a useful product. The technology readiness level (TRL) for the CL using perovskite is currently at level 3-4. To go to the next level, the best possible material in terms of yields, stability and durability must be found. Then this material could be used in large-scale installations to produce syngas according to the needs of future users.

To conclude, in a path towards carbon neutral economies, methods to treat CO<sub>2</sub> will gain more and more importance. Technologies for CCUS are multiple. To understand the numerous possibilities, it is sufficient to think of the high number of possible perovskite formulations which can be used for CL. Works like the one carried out in this thesis are necessary to highlights which of the many will be the winning technology.

# Bibliography

- [1] Ritchie, H. and Max Roser, M., *CO<sub>2</sub> and Greenhouse Gas Emissions*. OurWorldInData.org., 2020
- [2] Lindsey, R., *Climate change: Atmospheric carbon dioxide*. NOAA Climate.gov, 2020
- [3] IEA, *Global Energy Review 2021*. IEA, Paris, 2021
- [4] Le Quéré, C., Jackson, R.B., Jones, M.W. et al., *Temporary reduction in daily global CO<sub>2</sub> emissions during the COVID-19 forced confinement*. Nat. Clim. Chang. 10 (647–653), 2020
- [5] Taylor, M., *Wind, Solar: continuing cost declines will help meet rising renewables targets*. EnergyPost.eu, 2021
- [6] IEA, *The role of CCUS in low-carbon power systems*. IEA, Paris, 2020
- [7] Nunez, C., *Fossil fuels, explained*. National Geographic, 2019
- [8] Ritchie, H. and Max Roser, M., *CO<sub>2</sub> and Greenhouse Gas Emissions - CO<sub>2</sub> emissions by fuel*. OurWorldInData.org., 2020
- [9] IEA, *CCUS in Clean Energy Transitions*. IEA, Paris, 2020
- [10] Gonzalez Diaz, A., *Sequential supplementary firing in natural gas combined cycle plants with carbon capture for enhanced oil recovery*. 2016
- [11] Leung, D., Caramanna G., *An overview of current status of carbon dioxide capture and storage technologies*. Renewable and Sustainable Energy Reviews, pp. 426–443, 2014
- [12] Herzog, H., Meldon, J., Hatton, A., *Advanced Post-Combustion CO<sub>2</sub> Capture*. Industrial and engineering chemistry research, pp. 6423-6434, 2009

- [13] House, K. Z., Baclig, A. C., Ranjan, M., Van Nierop, E. A., Wilcox, J., Herzog, H. J., *Economic and energetic analysis of capturing CO<sub>2</sub> from ambient air*. Proceedings of the National Academy of Sciences, 2011
- [14] De Visser, E., Hendricks, C., Barrio, M., Molnvik, M.J., DeKoeijer, G., Liljemark, S., et al., *Dynamics CO<sub>2</sub> quality recommendations*. Int J Green Gas Control, pp.478-84, 2008
- [15] Olajire, AA., *CO<sub>2</sub> capture and separation technologies for end of pipe application - a review*. 2010
- [16] Jansen, D., Gazzani, M., Manzolini, G., van Dijk, E., Carbo, M., *Pre-combustion CO<sub>2</sub> capture*. International Journal of Greenhouse Gas Control, pp. 167-187, 2015
- [17] Lanzini, A., *Carbon capture and sequestration (CCS) processes*. Polygeneration and Advanced Energy Systems Course, Politecnico di Torino, 2020
- [18] Global CCS Institute , *CO<sub>2</sub> capture technologies: pre-combustion with CO<sub>2</sub> capture*. 2012
- [19] Metz, B., Davidson O., de Coninck H. C., Loos M., Meyer L. A., *IPCC Special Report on Carbon Dioxide Capture and Storage*. IPCC, Cambridge University, 2005
- [20] Pfaff, I., Kather, A., *Comparative thermodynamic analysis and integration issues of CCS steam power plant sbased on oxy-combustion with cryogenic or membrane based air separation*. Energy Procedia, pp. 495–502, 2009
- [21] Burdyny, T., Struchtrup, H., *Hybrid membrane/cryogenic separation of oxygen from air for use in the oxy-fuel process*. Energy2010, pp. 1884-97, 2010
- [22] Global CCS Institute *CO<sub>2</sub> capture technologies: oxy combustion with CO<sub>2</sub> capture*. 2012
- [23] Edwards, R., Celia, M., *Infrastructure to enable deployment of carbon capture, utilization, and storage in the United States*. 2018
- [24] Jenkins, C. R., et al *Safe storage and effective monitoring of CO<sub>2</sub> in depleted gas fields*. Proceedings of the National Academy of Sciences 109, 2012
- [25] Kearns, J.et al.,*Developing a Consistent Database for Regional Geologic CO<sub>2</sub> Storage Capacity Worldwide*. 2017

- [26] Chen, P., Xie, Q., Min, M., Liu, Y., Wang, Y., Cheng, Y., Li, K., Ruan, R., *Utilization of Municipal Solid and Liquid Wastes for Bioenergy and Bio-products Production*. ChemInform, 2016
- [27] Hosseini, S. E., Wahid, M. A., *Hydrogen production from renewable and sustainable energy resources: Promising green energy carrier for clean development*. Renewable and Sustainable Energy Reviews, 2016
- [28] Ghoniem, A. F., *Needs, resources and climate change: Clean and efficient conversion technologies*. Progress in Energy and Combustion Science, 2011
- [29] Price, R.J., Morse, D.A., Hardy, S.L., Fletcher, T.H., *Modeling the direct solar conversion of CO<sub>2</sub> to CO and O<sub>2</sub>*. Industrial and Engineering Chemistry Research, pp. 2446–2453, 2004
- [30] Bilgen, E., Ducarroir, M., Foex, M., Sibieude, F., Trombe, F., *Use of solar energy for direct and two-step water decomposition cycles*. International Journal of Hydrogen Energy, pp. 251–257, 1977
- [31] Traynor, A.J., Jensen, R.J., *Direct Solar Reduction of CO<sub>2</sub> to Fuel: First Prototype Results*. 2002
- [32] Rydén, M., Lyngfelt, A., Mattisson, T., *Chemical-looping combustion and chemical-looping reforming in a circulating fluidized-bed reactor using Ni-based oxygen carriers*. Energy and Fuels, pp. 2585–2597, 2008
- [33] Ortiz, M., et al. *Optimization of a chemical-looping autothermal reforming system working with a Ni-based oxygen carrier*. Proc 10th Int Conf Greenhouse Gas Technology (GHGT-10), 2010
- [34] Bhosale, R., Takalkar, G., Sutar, P., Kumar, A., AlMomani, F., Khraisheh, M., *A decade of ceria based solar thermochemical H<sub>2</sub>O/CO<sub>2</sub> splitting cycle*. International Journal of Hydrogen Energy 44, pp. 34–60, 2019
- [35] Krenzke, P.T., Davidson, J.H. *Thermodynamic Analysis of Syngas Production via the Solar Thermochemical Cerium Oxide Redox Cycle with Methane-Driven Reduction*. Energy and Fuels, pp. 4088–4095, 2014
- [36] Ishida, M., Jin, H., Okamoto, T., *Kinetic Behavior of Solid Particle in Chemical-Looping Combustion: Suppressing Carbon Deposition in Reduction*. Energy and Fuels 12, pp. 223–229, 1998
- [37] Michalsky, R., Avram, A. M., Peterson, B. A., Pfromm, P. H., Peterson, A.

- A., *Chemical looping of metal nitride catalysts: low-pressure ammonia synthesis for energy storage*. *Chemical Science* 6, pp. 3965-3974, 2015
- [38] Laassiri, S., Zeinalipour-Yazdi, C. D., Catlow, C. R. A., Hargreaves, J. S.. *The potential of manganese nitride based materials as nitrogen transfer reagents for nitrogen chemical looping*. *Applied Catalysis B: Environmental*, 223, pp. 60-66, 2018
- [39] Yan, H., Gao, W., Wang, Q., Guan, Y., Feng, S., Wu, H., Chen, P., *Lithium Palladium Hydride Promotes Chemical Looping Ammonia Synthesis Mediated by Lithium Imide and Hydride*. *The Journal of Physical Chemistry C*, 125(12), pp. 6716-6722, 2021
- [40] De Diego, L. F., García-Labiano, F., Adánez, J., Gayán, P., Abad, A., Corbella, B. M., Palacios, J. M., *Development of Cu-based oxygen carriers for chemical-looping combustion*. *Fuel*. pp. 1749-57, 2004
- [41] Ishida, M., Jin, H., *A novel chemical-looping combustor without NO<sub>x</sub> formation*. *Eng Chem Res*, pp. 2469-72, 1996
- [42] Ishida, M., Jin, H., *A novel combustor based on chemical-looping reactions and its reaction kinetics*. *J Chem Eng Jpn*, pp. 296-301, 1994
- [43] Perret, R., *Solar Thermochemical Hydrogen Production Research (STCH)*. Sandia National Laboratories Report, pp.1-117, 2011
- [44] Yadav, D., Banerjee, R., *A review of solar thermochemical processes*. *Renewable and Sustainable Energy Reviews* 54, pp. 497-532, 2016
- [45] Weidenkaff, A., Steinfeld, A., Wokaun, A., Auer, P., Eichler, B., Reller, A., *Direct solar thermal dissociation of zinc oxide: condensation and crystallization of zinc in the presence of oxygen*. *Solar Energy* 65, 1999
- [46] Loutzenhiser, P.G., Meier, A., Steinfeld, A., *Review of the Two-Step H<sub>2</sub>O/CO<sub>2</sub>-Splitting Solar Thermochemical Cycle Based on Zn/ZnO Redox Reactions*. *Materials*, pp. 4922-4938, 2010
- [47] Steinfeld, A., *Solar hydrogen production via a two-step water-splitting thermochemical cycle based on Zn=ZnO redox reactions*. *International Journal of Hydrogen Energy* 27, pp. 611-619, 2002
- [48] Villasmil, W., Brkic, M., Wuillemin, D., Meier, A., Steinfeld, A., *Pilot scale*

*demonstration of a 100-kWh solar thermochemical plant for the thermal dissociation of ZnO.* The Journal of Solar Energy Engineering, 2014

- [49] Bhosale, R. R., *Solar hydrogen production via ZnO/Zn based thermochemical water splitting cycle: Effect of partial reduction of ZnO.* International Journal of Hydrogen Energy, pp. 4739-4748, 2021
- [50] Scheffe, J. R., Steinfeld, A., *Oxygen exchange materials for solar thermochemical splitting of H<sub>2</sub>O and CO<sub>2</sub>: a review.* Materials Today (7), 2014
- [51] Nakamura, T., *Hydrogen production from water utilizing solar heat at high temperatures.* Solar Energy 19, pp. 467-475, 1977
- [52] Kodama, T., *High-temperature solar chemistry for converting solar heat to chemical fuels.* Progress in Energy and Combustion Science 29, pp. 567-597, 2003
- [53] Steinfeld, A., Sandres, S., and Palumbo, R., *Design aspects for solar thermochemical engineering-A case study: Two-step water splitting cycle using the Fe<sub>3</sub>O<sub>4</sub>-FeO redox system.* Solar Energy 65(1), pp. 43-53, 1999
- [54] Sibieude, F., Ducarroir, M., Tofighi, A., and Ambriz, J., *High temperature experiments with a solar furnace. The decomposition of Fe<sub>3</sub>O<sub>4</sub>, Mn<sub>3</sub>O<sub>4</sub>, CdO.* International Journal of Hydrogen Energy 7(1), pp. 79-88, 1982
- [55] Darken, L. S., Gurry, R. W., *The system iron-oxygen. II. Equilibrium and Thermodynamics of Liquid Oxide and Other Phase.* Journal of the American Chemical Society 63, pp. 798-816, 1946
- [56] Kodama, T., Nakamuro, Y., Mizuno, T., *A Two-Step Thermochemical Water Splitting by Iron-Oxide on Stabilized Zirconia.* Journal of Solar Energy Engineering 128, 2006
- [57] Tamaura, T., Steinfeld, A., Kuhn, P., and Ehrensberger, K., *Production of solar hydrogen by a novel, 2-step, water-splitting thermochemical cycle.* Energy 20(4), pp. 325-330, 1995
- [58] Ehrensberger, K., Frei, A., Kuhn, P., Oswald, H., and Hug, P., *Comparative experimental investigations of the water-splitting reaction with iron oxide and iron manganese oxides.* Solid State Ionics 78, pp. 151-160, 1995

- [59] Kodama, T., Gokon, N., Yamamoto, R., *Thermochemical twostep water splitting by ZrO<sub>2</sub>-supported Ni<sub>x</sub>Fe<sub>3-x</sub>O<sub>4</sub> for solar hydrogen production*. Solar Energy 82(1), pp. 73–9, 2008
- [60] Kubicek, M., Borkac, A. H., Rupp, J. L. M., *Perovskite oxides – a review on a versatile material class for solar-to-fuel conversion processes*. Journal of Materials Chemistry A 5, 2017
- [61] Carrillo, R. J., Scheffe, J. R., *Advances and trends in redox materials for solar thermochemical fuel production*. Solar Energy 156, pp. 3-20, 2017
- [62] Goldschmidt, V. M., *Die Gesetze der Krystallochemie*. Naturwissenschaften 14, pp. 477–485, 1926
- [63] Haeussler, A., Abanades, S., Jouannaux, J., Julbe, A., *Non-Stoichiometric Redox Active Perovskite Materials for Solar Thermochemical Fuel Production: A Review*. Catalysts 8(12), 611, 2018
- [64] Jiang, S. P., *Development of lanthanum strontium manganite perovskite cathode materials of solid oxide fuel cells: a review*. Journal of Materials Science 43, pp. 6799–6833, 2008
- [65] Xue, Y., Miao, H., Sun, S., Wang, Q., Li, S., Liu, Z., *(LaSr)<sub>0.98</sub>MnO<sub>3</sub> perovskite with A-site deficiencies toward oxygen reduction reaction in aluminum-air batteries*. Journal of Power Sources 342, pp. 192–201, 2017
- [66] Demont, A., Abanades, S., *High redox activity of Sr-substituted lanthanum manganite perovskites for two-step thermochemical dissociation of CO<sub>2</sub>*. RSC Advances 97, 2014
- [67] Dey, S., Naidu, B. S., Rao, C. N. R., *Ln<sub>0.5</sub>A<sub>0.5</sub>MnO<sub>3</sub> (Ln = Lanthanide, A = Ca, Sr) Perovskites Exhibiting Remarkable Performance in the Thermochemical Generation of CO and H<sub>2</sub> from CO<sub>2</sub> and H<sub>2</sub>O*. Chemistry—A European Journal 21, pp. 7077–7081, 2015
- [68] Takalkar, G., Bhosale, R. R., AlMomani, F., Rashid, S., Qiblawey, H., Saleh Saad, M. A., Khraisheh, M., Kumar, G., Gupta, R. B., Shende, R., V., *Thermochemical splitting of CO<sub>2</sub> using solution combustion synthesized lanthanum–strontium–manganese perovskites*. Fuel 285, pp. 119-154, 2021
- [69] Demont, A., Abanades, S., *Solar thermochemical conversion of CO<sub>2</sub> into fuel via two-step redox cycling of non-stoichiometric Mn-containing perovskite oxides*. Journal of Materials Chemistry 3, pp. 3536–3546, 2015

- [70] Nair, M. M., Abanades, S., *Insights into the Redox Performance of Non-stoichiometric Lanthanum Manganite Perovskites for Solar Thermochemical CO<sub>2</sub> Splitting*. Chemistry Select 1, pp. 4449–4457, 2016
- [71] Farooqui, A. E., *Solar fuels via two-step thermochemical redox cycles for power and fuel production*. Doctoral Program of Erasmus Mundus in Environmental Pathways for Sustainable Energy Services (SELECT+), 2019
- [72] Cimino, S., Lisi, L., De Rossi, S., Faticanti, M., Porta, P., *Methane combustion and CO oxidation on LaAl<sub>1-x</sub>Mn<sub>x</sub>O<sub>3</sub> perovskite-type oxide solid solutions*. Applied Catalysis B: Environmental 43, pp. 397–406, 2003
- [73] McDaniel, A. H., Ambrosini, A., Coker, E. N., Miller, J. E., Chueh, W. C., O’Hayre, R., Tong, J., *Nonstoichiometric perovskite oxides for solar thermochemical H<sub>2</sub> and CO production*. Energy Procedia 49, pp. 2009–2018, 2014
- [74] McDaniel, A. H., Miller, E. C., Arifin, D., Ambrosini, A., Coker, E. N., O’Hayre, R., Chueh, W. C., Tong, J., *Sr- and Mn-doped LaAlO<sub>3-δ</sub> for solar thermochemical H<sub>2</sub> and CO production*. Energy and Environmental Science 6, 2013
- [75] Cooper, T., Scheffe, J. R., Galvez, M. E., Jacot, R., Patzke, G., Steinfeld, A., *Lanthanum Manganite Perovskites with Ca/Sr A-site and Al B-site Doping as Effective Oxygen Exchange Materials for Solar Thermochemical Fuel Production*. Energy Technology 3, pp. 1130-1142, 2015
- [76] Carrillo, A. J., Bork, A. H., Moser, T., Sediva, E., Hood, Z. D., Rupp, J. L. M., *Modifying La<sub>0.6</sub>Sr<sub>0.4</sub>MnO<sub>3</sub> Perovskites with Cr Incorporation for Fast Isothermal CO<sub>2</sub>-Splitting Kinetics in Solar-Driven Thermochemical Cycles*. Advanced Energy Materials 9, 2019
- [77] Furler, P., Scheffe, J., Marxer, D., Gorbar, M., Bonk, A., Vogt, U., Steinfeld, A., *Thermochemical CO<sub>2</sub> splitting via redox cycling of ceria reticulated foam structures with dual-scale porosities*. Physical Chemistry Chemical Physics 16, pp. 10503-10511, 2014
- [78] Muhich, C. L., Weston, K. C., Arifin, D., Mcdaniel, A. H., Musgrave, C. B., Weimer, A. w., *Extracting kinetic information from complex gas-solid reaction data*. Industrial and Engineering Chemistry Research 54(16), pp. 4113-4122, 2015
- [79] Jouannaux, J., Haeussler, A., Drobek, M., Ayral, A., Abanades, S., Julbe, A.,

*Lanthanum manganite perovskite ceramic powders for CO<sub>2</sub> splitting: Influence of Pechini synthesis parameters on sinterability and reactivity.* Ceramics International 45, pp. 15636–15648, 2019

- [80] Haeussler, A., Julbe, A., Abanades, S., *Investigation of reactive perovskite materials for solar fuel production via two-step redox cycles: Thermochemical activity, thermodynamic properties and reduction kinetics.* Materials Chemistry and Physics 276, pp. 125- 358, 2022
- [81] Boaro, M., Felli, A., *PRIN17 Project “Direct Biopower”.* 2020
- [82] Liu, Q., Yang, C., Dong, X., Chen, F., *Perovskite Sr<sub>2</sub>Fe<sub>1.5</sub>Mo<sub>0.5</sub>O<sub>6-δ</sub> as electrode materials for symmetrical solid oxide electrolysis cells .* International Journal of Hydrogen Energy 35, pp. 10039–10044, 2010
- [83] Ruiz-Morales, J. C., Marrero-López, D., Canales-Vázquez, J. Irvine, J. T. S., *Symmetric and reversible solid oxide fuel cells.* RSC Advances 1, pp. 1403–1414. 2011
- [84] Ruddlesden, S.N., Popper, P., *New compounds of the K<sub>2</sub>NiF<sub>4</sub> type* Acta Crystallography 10, pp. 538–539, 1957
- [85] Yattoo, M. A., Skinner, S. J., *Ruddlesden-Popper phase materials for solid oxide fuel cell cathodes: A short review.* Materials Today: Proceedings, 2022
- [86] Nikonov, A. V., Kuterbekov, K. A., *A brief review of conductivity and thermal expansion of perovskite-related oxides for SOFC cathode.* Eurasian Journal of Physics and Functional Materials 2(3), pp. 274-292, 2018
- [87] Du, Z., Zhao, H., Yi, S., Xia, Q., Gong, Y., Zhang, Y., Cheng, X., Li, Y., Gu, L., Swierczek, K., *High-Performance Anode Material Sr<sub>2</sub>FeMo<sub>0.65</sub>Ni<sub>0.35</sub>O<sub>6-δ</sub> with In Situ Exsolved Nanoparticle Catalyst.* American Chemical Society 10, pp. 8660-8669, 2016
- [88] API SRL *Manuale API-MIoT PoliTo.* Doc. nr. UG002007 Rev. A, 2020
- [89] Carbolite Gero Ltd. *Carbolite Gero 3000°C, furnace brochure catalogue*
- [90] Raja, P. M. V., Barron, A. R., *Catalyst Characterization Using Thermal Conductivity Detector.* Rice University. <https://chem.libretexts.org/@go/page/55930>, 2021
- [91] Snaveley, K., Subramaniam, B., *Thermal Conductivity Detector Analysis of*

*Hydrogen Using Helium Carrier Gas and HayeSep D Columns.* Journal of Chromatographic Science, Vol. 36, 1998

- [92] Toonen, A., van Loon, R., *Hydrogen Detection with a TCD using Mixed Carrier Gas on the Agilent Micro GC.* Agilent Technologies, 2013
- [93] Wong, J., Y., Anderson, R., L., *Non-Dispersive Infrared Gas Measurement.* International Frequency Sensor Association Publishing, 2012
- [94] Sun, Y., W., Liu, C., Chan, K., L., Xie, P., H., Liu, W., Q., Zeng, Y. et al. *Stack emission monitoring using non-dispersive infrared spectroscopy with an optimized nonlinear absorption cross interference correction algorithm.* Atmospheric Measurement Techniques 6, pp. 1993-2005, 2013
- [95] Burough, I., G., Creek, W., *Gas analyzer and gas analyzing method.* U.S. patent (Ed.), Andros Incorporated, 1980
- [96] Passaro, R., E., Williams, K., *Non-dispersive infrared gas analyzer.* U.S. Patent, Andros Analyzers Incorporated, 1982
- [97] Farren, C., A., *Non-dispersive infrared analyzer having improved infrared source and detecting assemblies.* Beckman Industrial Corporation, 1986
- [98] Park, J., Yi, S., *Temperature compensated NDIR CH<sub>4</sub> gas sensor with focused beam structure.* Procedia Engineering 5, pp. 1248-1251, 2010